UNIVERSITAT ROVIRA I VIRGILI

DEEEA
Departament d'Enginyeria Electrònica, Elèctrica i Automàtica

GRADUATED STUDENT MEETING

on

ELECTRONIC ENGINEERING

Tarragona, July 5-6, 2007

DIPUTACIÓ DE TARRAGONA

Abstracts Book

Graduated Student Meeting

on

Electronic Engineering

Tarragona, July 5-6, 2007

Organising Comitee

Xavier Vilanova

Lluis F. Marsal

Josep Ferré-Borrull

Margarita Rebenaque

Montse Rollizo

Mireia Alberich

Programme

Thursday, 5th July

10:00 Opening Session
10:15 Plenary Seesion 1
Tatiana Perova
11:30 Coffee break
11:45 Plenary session 2
Massimiliano Decarli
13:00 Lunch
15:00 Poster Session
16:30 Plenary session 3
Claude Lucat

Friday, 6th July

10:15 Plenary session 4
Mikael Östling
11:30 Coffee break
11:45 Plenary session 5
Claudia Zwingmann
13:00 Lunch
15:00 Poster session
16:30 Plenary session 6
Magali Estrada
17:45 Closing session and Best Poster Award

Invited Speakers

Plenary sesion 1

Design, fabrication and characterisation of ordinary and tunable photonic structures based on silicon for optical interconnects

Tatiana Perova
Department of Electronic & Electrical Engineering,
University of Dublin, Trinity College, Ireland

Plenary sesion 2

A technological Approach to BioMEMS: Overview and Prospects

Massimiliano Decarli
Microsystems Division, BioMEMS Group Center for Scientific and Technological Research (ITC-irst)
Fondazione Bruno Kessler Povo (Trento), Italy

Plenary sesion 3

Screen-Printing Technology for Mems Applications

Claude Lucat
Laboratoire IXL
CNRS, Bordeaux, France

Plenary sesion 4

Critical technology issues for deca-nanometer MOS

Mikael Östling
School of Information and Communication Technology
KTH, Royal Institute of Technology, Kista, Sweden

Plenary sesion 5

Potential and Design of New High-Resolution Multinuclear NMR Approaches in Metabonomics for Clinical Research and Diagnosis

Claudia Zwingmann
Département de médicine, Hôpital Saint-Luc Montréal,
Université de Montréal, Québec, Canada

Plenary sesion 6

Organic Semiconductor Devices

Magali Estrada del Cueto
Departamento de Ingeniería Eléctrica, Sección de Electrónica del Estado Sólido
Centro de Investigación y de Estudios Avanzados del IPN, México D.F.

Index

Invited Speakers

Posters

Plenary Sessions

Design, fabrication and characterisation of ordinary and tunable photonic structures based on silicon for optical interconnects

Tatiana Perova

Department of Electronic and Electrical Engineering
University of Dublin, Trinity College, Dublin 2, Ireland
e-mail: perovat@tcd.ie; Tel.: +3531 8961432; FAX: +3531 6772442

Over the last three decades, there has been rapid improvement of computer chip performance and downscaling of individual components. However, as computational power continues to increase, it is becoming increasingly difficult to provide the necessary communication between computer boards, chips and even individual chip components. This creates an interconnect bottleneck, which is predicted to become a "grand challenge" for the semiconductor industry by the year 2018 [1]. One of the solution to this problem is the investigation of unconventional interconnect technologies, such as optical interconnects, for example.

Silicon is nearly transparent and generally does not interact with the infrared light, making it an exceptional medium for guiding optical data streams between acting components. This is in particular important for developing devices and providing functionality in the optical domain for infrared wavelength common to silica fibre-optics telecommunication systems (1.3 to 1.5 μm). Optics on a silicon chip provides a new platform for monolithic integration of optics and microelectronics and can open the door to a new technology that is free from conventional microelectronic [2-4].
However, the difficulty in controlling light and diverting its path on silicon need to be addressed before this technology can successfully be used to resolve current microelectronics bottleneck.
Silicon-based photonic bandgap (PBG) structures have emerged in the research community as an established technology for fabricating high-performance ultracompact optical elements [5-10]. PBG structures have the advantage of providing strong light confinement in a compact geometry compared to other optical interconnects alternatives, such as Mach-Zehnder interferometers [10]. Furthermore, by having the capability for active control and multiplexing of the propagating light, tunable silicon-based PBG structures offer an exciting opportunity to investigate a potentially viable solution to the interconnect bottleneck.

This presentation is mainly focused on the design, fabrication and characterization of the ordinary and tunable photonic devices based on grooved silicon serving as one-dimensional (1D) photonic crystal. One-dimensional periodic structures with deep vertical grooves were design and fabricated by wet anisotropic etching on (110) oriented silicon and by deep reactive ion etching on (100) silicon wafers. Depending on the lattice parameter, the structures possess not only a main photonic band gap in the region of 10-30 μm, but also a number of secondary band gaps extended to the near infrared range of spectra. The possibility of PBG extension by introducing a silicon wall thickness disorder into the photonic structure have been shown theoretically and

experimentally.

The advantages of these photonic structures are as follows: the large refractive index contrast, in-plane moulding of the light flow, the possibility to fabricate a composite photonic structures by filling the grooves with a different compounds and compatibility with current semiconductor processing techniques. The optical properties of grooved Si structures were simulated using a transfer matrix method and band diagram method and have been verified experimentally using FTIR spectrometer in conjunction with IR microscope. The air spaces in the basic silicon-air matrices were then infiltrated with nematic liquid crystal E7. It is shown that the optical properties of the obtained composite 1D photonic crystals can be tuned by means of electro- and thermo-optical effects. Such a structures suit well for the various elements of the integrated optics and can serve as a building blocks for optical interconnects.

References

1. http://public.itrs.net
2. V.R. Almeida, C.A. Barrios, R.R. Panepucci, and M. Lipson, *Nature*, 2921, 117492 (2004).
3. M. Lipson, *Optical Materials*, 27, 731 (2005).
4. L.C. Kimerling, Applied Surface Science, 159-160, 8 (2000).
5. M. Salib, L. Liao, R. Jones et al., *Intel Technology Journal: Silicon Photonics*, 8, N2, 149 (2004).
6. A. Birner, R.B. Wehrsporn, U.M. Gösele, K. Busch, *Adv. Mater*., 13, 377 (2001).
7. L. Pavesi, *J. Phys.: Condens. Matter,* **15,** R1169 (2003).
8. S.M. Weiss, M. Haurylau, P.M. Fauchet, *Optical Materials*, 27, 740 (2005).
9. V.A. Tolmachev, T.S. Perova, S.A. Grudinkin, V.A. Melnikov, E.V. Astrova, Yu.A. Zharova, *Appl.Phys.Lett.,* **90**, 011908-10 (2007); *Physica Stat.Sol.*(c), 4, N6, 1961-1965 (2007).
10. Y. Matsuhisa, R. Ozakia, K. Yoshino, and M. Ozaki, *Appl.Phys.Lett*., **89**, 101109 (2006).

A. Liu, R. Jones, L. Liao, D. Samara-Rubio, D. Rubin, O. Cohen, R. Nicolaescu, M. Paniccia, *Nature,* 427, 615 (2004).

A technological Approach to BioMEMS: Overview and Prospects

Massimiliano Decarli

Microsystems Division,
BioMEMS Group Center for Scientific and Technological Research (ITC-irst)
Fondazione Bruno Kessler Povo (Trento), Italy

In the last twenty years, microfabrication technology for microsystems (MST) have been recognized as one of the most promising for theirs potential of innovation in the research and development of miniaturized systems in the field of micromechanics (MEMS, Micro-Electro-Mechanical-Systems), in biomedical applications (BioMEMS) and in optoelectronics (MOEMS, Micro-Opto-Electro-Mechanical-Systems). The possibility of integration of silicon-based technologies, typical of microelectronics, with the most recent microfabrication techniques has allowed developing a large area of different microsystems with a big fall-out effect on the industrial sector.

The seminar will give a general introduction on BioMEMS, with respect to commercial applications and R&D as well as to fabrication techniques. Finally some case-studies will be proposed and discussed, in a BioMEMS perspective..

Screen-Printing Technology for Mems Applications

Claude Lucat

Laboratoire IXL
CNRS, Bordeaux, France

Screen-printing, a cheap collective way of fabrication of microcomponents, has been widely used in microelectronics to fabricate interconnexions, passive components (varistors, heating elements, etc.) and sensors. In addition, when compacity of the films is concerned for some applications, one has to use specific densification process. In other respects, manufacturing of thick-film actuators suffered from the lack of technological solutions for releasing the free-standing layers (also referred as structural layers), which are required to be actuated separately from the substrate.

The aim of my lecture is first to describe the standard thick-film technology with the different problems arising at the level of each element of the micro-assembly, namely the substrate, the electrodes, the active material, etc. A new densification process, developed in our laboratory to improve the physicochemical properties of thick-films, is also presented. Examples drawn from our own experience in this area, deal with super-thick copper pads, varistors, PZT-based pyroelectric sensors, semiconductor oxide gas sensors, zirconia oxygen sensors, etc.

Then, I will introduce the extension of this standard technology to the fabrication of “MEMS”. As with silicon micromachining, it has been first necessary to develop a new thick-film process based on the sacrificial layer principle. Prior to the deposition of the structural layer, a sacrificial layer is screen-printed on the substrate and cured at low temperature. The sacrificial layer acts as a stable mechanical support during the firing of the structural layer and is totally removed after the final thermal treatment of the sample in a weak acidic solution. Subsequently, thick film structural layer of cantilever, bridge or channel type may be obtained. Potentialities of this new process in MEMS area are shown through studies of electrothermal actuators, heating resistors, microchannels, PZT piezoelectric device, etc.

Critical technology issues for deca-nanometer MOS

Mikael Östling

School of Information and Communication Technology
KTH, Royal Institute of Technology, Sweden

An overview of critical integration issues for future generation MOSFETs towards 10 nm gate length is presented. Novel materials and innovative structures are discussed and include the need for high-κ gate dielectrics and a metal gate electrode. Different techniques for strain-enhanced mobility are shown and recent experimental results will be presented as well as the necessity for drastically lowered S/D access resistances.

Potential and Design of New High-Resolution Multinuclear NMR Approaches in Metabonomics for Clinical Research and Diagnosis

Claudia Zwingmann
Département de médicine, Hôpital Saint-Luc Montréal,
Université de Montréal, Québec, Canada

Novel approaches are required for the study of human disease states aimed at improvement of diagnostic procedures, evaluation of disease progression, and identification of molecular targets for therapeutic intervention. A growing shift toward translational studies in today's biomedical research scene is metabonomics. It uses small molecules to detect changes in cell behaviour and organ function, and to monitor drug reactions. Physicians and scientists around the world are now beginning to realize that metabolic profiling will have a significant impact on the non-invasive evaluation of human diseases, and could provide clinical uses sooner than either genomics or proteomics. It is now the time to apply state-of-the-art analytical metholodogies and to develop new approaches in this emerging branch of the present basic and clinical research. In contrast to radiolabelling chromatographic assays, NMR spectroscopy is a unique technique to quantifiy multiple metabolites of biological significance simultaneously without altering or destroying the sample and without pre-selection of compounds. This method has emerged quickly as a powerful tool for studying complex biomedial problems. In conjunction with bioinformatics, the NMR information can be reduced to a metabolic profile characteristic of a specific disease/pathology.

Preliminary data using this approach have been performed to investigate metabolic alterations in urine- and blood samples in patients with non-alcoholic fatty liver diseases (NAFLD). Furthermore, to study other metabolites not detectable by conventional ^{1}H NMR analysis, preparatory work was done to explore the feasibility of natural abundance ^{13}C NMR measurements. To identify unknown metabolites in body fluids, two-dimensional $\{^{1}H\text{-}^{1}H\}$ and $\{^{1}H\text{-}^{13}C\}$ experiments were used to resolve overlapping resonances in ^{1}H NMR spectra. However, all these metabonomics approaches have the

major drawback in being hardly able to evaluate mechanistic clues underlying human diseases. An innovative approach would to create infrastructure and assist in the creation of novel research projects combining metabolic profiling in human samples with ex vivo and in vitro ^{13}C isotopomer analysis in animal models to elucidatethe mechanisms underlying different diseases. Our major previous NMR work has focussed on the study of intermediary metabolism by ^{13}C-NMR spectroscopy and stable isotopes. ^{13}C-NMR is the unique technique to investigate non-invasively fluxes through many metabolic pathways simultaneously. Examples for ^{13}C-NMR studies in animal models are given for: 1) Hepatic Encephalopathy, a neurological disorder caused by liver dysfunction. These studies have challenged the recent hypothesis for the development of brain edema. 2) The protective effects of N-acetylcysteine (NAC) in liver injury. These studies revealed new mechanisms of hepatoprotection at the level of intermediary metabolism, which are uncoupled from glutathione replenishment, previously suggested to be responsible for hepatoprotection by NAC. 3) Metabolic alterations in the early stage of hepatocellular apoptosis. These studies revealed that specific changes in glucose metabolism are prerequisite for the initiation and progression of the apoptotic process. The proposed multidisciplinary approach at the interface between clinical and

basic research will ultimatively bring the basic research work into a clinical forum and visa versa.

The proposed new approach of combining traditional 1H-NMR-based metabonomics with other non-invasive NMR applications on body fluids and with mechanistic studies using stable isotopes in animal models of human diseases will make an important contribution to improve diagnosis, treatment and understanding of human diseases.

Organic Semiconductor Devices

M. Estrada, J. C. Sánchez, I. Mejía. J. Nolasco, A. Cerdeira, Y. Matsumoto, A. Escobosa, B. Iñiguez*, L. Marsal*, J. Pallares*

Sección de Electrónica del Estado Sólido
Departamento de Ingeniería Eléctrica
CINVESTAV-IPN

*Departament dÉnginyeria Electronica Eléctrica i Automatica,
Universitat Rovira i Virgili,

After an introduction containing general aspects of organic devices, we present some of the results obtained by our group.
Results include the fabrication and characterization of two types of top gate polymeric devices using Polymethyl Metacrylathe (PMMA) as dielectric and Poly (3, hexylthiophene) (P3HT) as semiconductor using photolithographic technique. This technique has been, up to now not compatible with polymeric devices fabrication.
A study of the interface properties, where a density of surface states $Nss<1.5x10^{11}$ cm^{-2} is observed are discussed, as well as the electric characteristics of the devices.
We also show how to control and return the electrical characteristics to their initial behavior, after degradation with time.
Finally we show aspects regarding modeling of these devices, which seem to differs from other organic devices, as for example Pentacene.
We will also show first results on OLEDs fabricated with a new emitting polymer, the copolymer (BEHP PPV) co (MEH PPV), which presents some advantages with respect to (MEH PPV).
Finally we show preliminary characteristics of the heterojunction formed between P3HT and Si for solar cell applications..

Posters

Two or three-way data analysis in MS-Sensor devices. Which is the optimal approach?

M. Vinaixa*, J. Brezmes, E. Llobet, X. Vilanova, X. Correig
MINOS, DEEEA, Universitat Rovira i Virgili (URV)
Avda. Països Catalans, 26, 43007 Tarragona, *maria.vinaixa@urv.cat

Abstract

The goal of this paper is to compare the performance of two-way versus three way classifier models for their application in pattern recognition of MS-Sensor devices. Three classifier models, namely bilinear PLS-DA, trilinear N-PLS-DA and PARAFAC-MLR-DA (multilinear regression discrimination using loads for first mode as X-block predictors) are applied and compared in the framework of a classical MS-Sensor application such as olive oil discrimination.

Introduction

In recent yeats it has been shown that the rapid analysis of the global volatile fraction of foods by mass spectrometry without chromatographic separation produces signals (signatures) that contain significant and useful information. The so called MS-Sensor approach has been applied to compare the volatile fingerprint profile of samples and classify these samples according to their respective signatures. The main advantages rely on the fact that sample treatment is eliminated or reduced to a minimum and the fact that since chromatographic separation is avoided, near-real time results can be obtained.

In Spain, olive oil constitutes an important economic activity and much attention has been devoted to the study of such a product in recent years. Classical techniques used to assess its quality are usually time consuming and present a low throughput. MS-Sensor devices represent a novel oportunity to assess the quality of olive oils in a rapid, solvent free and easy way. Common pattern recognition algorithms applied on MS-Sensor data make use of the averaged mass spectra along the detected peak. Nevertheless, considering this averaged mass spectrum may lead to losing useful temporal information. Even when chromatographic resolution is avoided, a sort of diffusion is observed on the isothermal peak. This fact allows us to consider the possibility of computing this extra-information by considering the three way nature of the data using of trilinear algorithms such N-PLS or PARAFAC. Multi-way methods are particularly useful for treating data with more than two sources of variability like the data generated by MS-Sensor devices, where the response in ion counts arriving at the detector is measured as a function of time and mass/charge ratio. In fact, data provided from a MS-Sensor should be arranged as multi-way array where the first mode represents samples, the second one corresponds to mass spectra and the third to the elution profiles. Exploiting differences in the time response of the analytes can enhance the subtle variations in the spectra and therefore classification performance may be improved. The main goal of this paper is to see whether classifier algorithms may benefitiate from the use of second-order methods, even in the case of crude or poor chromatographic separation such direct MS-Sensor devices. To date, the application of second-order methods to classifier models in MS-Sensor devices has not been reported in the literature.

Experimental

Five different virgin olive oils were received directly from producers in 100 ml transparent glass bottles airtight sealed. They were kept frozen before any analysis was performed. The day before the analysis, all the samples were kept out of the freezer and were exposed at room temperature in darkness. Equal amount of samples (5 g) were placed in 20-ml glass vials that were immediately sealed with silicon septum. Six different aliquots were pipetted from each of the five oils giving a total of 30 vials to be analysed. SPME extraction of volatiles was performed by introducing a 50/30 µm DVB/Carboxen/PDMS (Supelco, Bellafonte, PA.) fibre into the vial and exposing them to the headspace of oil for 20 minutes. Afterwards, thermal desorption of the volatiles trapped on the fibre was conducted for 3 minutes in the chromatograph injection port at 270ºC. Volatiles trapped on the fibre were delivered to a 5- m deactivated fused silica column. The column was kept isothermal at 250ºC and the helium flow was set to 1.4 ml/min. The split valve was closed during desorption. The quadrupole mass spectrometer acquired in scan mode, and the mass range used was m/z 35 to m/z 200 at 0.5 scan/sec. The fibre was left 5 additional minutes in the injector port to ensure its complete cleaning. MS-Sensor data was imported into ASCII format and finally loaded into MATLAB version 6.5 (Mathworks, Inc., Natick, MA) for further data processing. The MATLAB routines used for PLS-DA, NPLS-DA and PARAFAC-mlr-DA were adapted from the PLS_Toolbox, version 3.5 (Eigenvector Technologies, Inc.,Manson, WA).

Results and Discussion

Raw data provided by the MS-Sensor was arranged as a three-way array data set $\underline{\mathbf{R}}$ (30×166×205). A modification of the previous reported RAFFT aligment algorithm was applied to $\underline{\mathbf{R}}_1$ (30×166×205) before any modelling in order to overcome retention time shifts from run to run. This modification consisted in the application of this algorithm to each m/z channel instead of doing so to the reconstructed TIC signal. Finally a two-way response matrix $\mathbf{R}_2$ (30×166) was obtained by averaging m/z values along the 205 scans considered. Exploratory data analysis was conduced using PARAFAC and PCA in order to observe the main trend on the data sets. Figure 1 shows PARAFAC's loads plot for samples modelled

using six components. The same trend is observed in both PARAFAC and PCA models. The five types of oils cluster well appart. Separation according origins is achieved in both cases and it seems that a gradation of scores indicating oil quality can also be deduced. Component 2 allows to ditinguish between geographical origins.

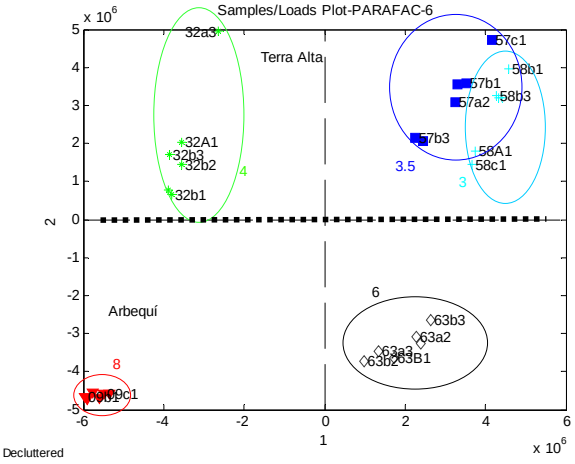

Figure 1. 6 component PARAFAC loads plot

Finally $\underline{\mathbf{R_1}}$ (30×166×205) and response matrices $\mathbf{R_2}$ (30×166) were split up into two parts: a training set and a test set. In the training phase a 5-category classification was envisaged according to each type of olive oil using either two-way PLS-DA or three way related methods as PARAFAC-mlr-DA or N-PLS-DA and four of the six measures in each category were used. The remaining two vials unseen by the model were used as a test set for further validation. Prior to any calculation, data were centered across the first mode for the three-way array and meancentered in the case of two-way matrix. The training phase of the models was evaluated using a cross-validation method, and RMSECV was used to assess the optimal number of factors for model fitting. Once the model had been trained, predicted category for test set samples was attempted. The predicted y-value from the calibrated models results in a continuous variable that can be interpreted as a class similarity index. Each calculated class prediction value can be compared with a Bayesian distribution curve to determine for a given predicted y-value the probability that this value belongs to that original class. Furthermore a threshold of "predicted y" is determined above which a sample is considered to be a member of the class. These thresholds are also calculated for the three models and class assignment is done comparing against this value. Figure 2 shows class predicted values for the test set samples using N-PLS-DA model. The dashed red horizontal lines represents the calculated thresholds. Regression between actual and predicted Y-values were performed for the three models to better assess their accuracy. The correlation coefficient, slope and intercept were calculated. Table 1 summarizes the characteristics of the N-PLS-DA, PLS-DA and PARAFAC-MLR-DA models calibrated for the classification of the olive oil samples.

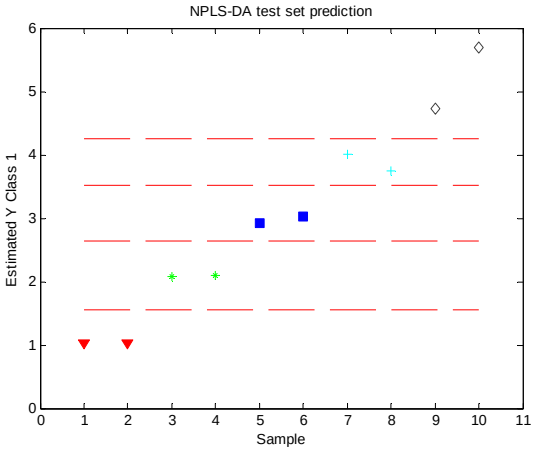

Figure 2. N-PLS-DA class predicted

	PLS-DA	N-PLS-DA	PARAFAC-MLR-DA
#LV's	11	11	6
%Succees rate test-set	100	100	100
RMSECV	0,14	0,17	0,23
RMSEP	0,19	0,25	0,23
X val	99,98	99,53	100
Y val	98,24	99,42	99,19
b (test)	-0,05	-0,01	0,14
m (test)	1,03	1,01	0,97
R2 (test)	0,99	0,97	0,97

Table 1. models' characteristics

Several conclusions can be drawn from this table. Regardless of which classifier method employed, all of them achieved a 100% success rate in classification of test samples. Concerning the number of components needed to fit each model, PARAFAC-MLR-DA is pointed to be the simplest model and consequently the most parsimonious one. Nevertheless, taking a look to RMSECV and RMSEP, we can conclude that despite the fact that all the models are able to classify new samples in a correct way, PLS-DA seems to outperform three-way methods. Therefore, for this particular application, the introduction of the third dimension does not allow to improve the performance of the MS-sensor device. Anyway, the parsimonity observed in the PARAFAC model and the fact that the performance remains quite acceptable leads us to consider that this model is more robust and may outperform classical approaches in a broader set of applications.

References

[1] J. W. H. Wong, C. Durante and H. M. Cartwright, *Analytical Chemistry* **2005**, *77*, 5655-5661.

[2] W. P. Gardner, R. E. Shaffer, J. E. Girard and J. H. Callahan, *Analytical Chemistry* **2001**, *73*, 596-605.

Correlation between electronic nose signals and bacteriological responses on shelf-life determination for red meat analysis

N. El Barbri[1*], B. Bouchikhi[1], E. Llobet[2], N. El Bari[3] and X. Correig[2]

1) Sensor Electronic & Instrumentation Group, Faculty of Sciences, Physics Department, University Moulay Ismaïl, B.P. 11201, Zitoune, Meknes, Morocco
2) MINOS, Microsystems and Nanotechnologies for Chemical Analysis, Universitat Rovira i Virgili, Avda. Països Catalans, 26, 43007 Tarragona, Spain
3) Biotechnology Agroalimentary and Biomedical Analysis Group, Faculty of Sciences, Biology Department, University Moulay Ismaïl, B.P. 11201, Zitoune, Meknes, Morocco
* Corresponding author; E-mail: noureddine.elbarbri@caramail.com

Abstract

Objective and rapid method for quality control of red meats has been developed. A metal oxide sensor-based electronic nose system consisting of six sensors was designed and used to analyze the headspace emanating from beef and sheep stored at 4 °C. A bacteriological method was selected as the reference method to consistently train the electronic nose system. The support vector machine (SVM) classification models classified meat samples based on the total microbial population into "unspoiled" (microbial counts < 6 log10 cfu/g) and "spoiled" (microbial counts ≥ 6 log10 cfu/g). The preliminary results obtained by the bacteria total viable counts (TVC) show that the shelf-life of beef and sheep meat stored at 4°C are 7 and 5 days, respectively. The electronic nose system coupled to SVM could to discriminate between unspoiled/spoiled beef or sheep meats with a success rate of 98.81 or 96.43%, respectively. To investigate whether the results of the electronic nose correlated well with the results of the bacteriological analysis, partial least squares (PLS) calibration models were built and validated. Good correlation coefficients between the electronic nose signals and bacteriological data were obtained.

Keywords – E-nose; Bacterial measurement; Red meat; Shelf-life; SVMs; PLS models.

1. Introduction

The control quality of the red meats is not only a major preoccupation of the consumers but also of the producers and distributors. The development of an objective and rapid method to spoilage classification of beef and sheep requires the building of reliable and simple tools, which facilitate routine control assessments.

In this paper, an electronic nose is used to assess the quality of beef and sheep meats stored at 4°C. Although, bacterial growth on the meat has been extensively studied, methods based on the total count of bacteria that correlate well with shelf-life determination are still under investigation. The purpose of this study is to evaluate the electronic nose performance as an additional instrument for the quality control of beef and sheep meats.

2. Experimental

2.1 Sample preparation and sampling

Two different types of meat species representative of Moroccan production and purchased from a local market were analysed. The samples from different animal species (beef and sheep) were cut into pieces of the same weight (10 g ± 1 g) immediately after receiving, placed in plastic bags (bags for freezing food) and introduced in a refrigerator kept at a constant temperature of 4°C ± 1°C. For each measurement, a meat sample was taken from the refrigerator and put inside a 500 ml glass bottle. The sampling bottles were sealed with septum and held at room temperature (22°C ± 2°C) for 50 min in order to reach a stable composition of the headspace. Measurements were performed each day for up to 2 weeks. Every day two replicate samples were extracted from the refrigerator to undergo microbiological analysis and six replicate samples were employed for electronic nose analysis.

2.2 Microbiological population enumeration

A 25 g sample of each product was randomly taken and placed in a sterile stomacher bag containing 225 ml of 0.1% (wt/vol) peptone water (PW, Oxoid Ltd., Hampshire. England). The sample and the PW were stomached for 2 min. Decimal dilutions were prepared using the same diluents. These dilutions were subsequently plated on the surface of a Plate Count Agar (PCA, Oxoid Ltd.). The plates were incubated at 30°C for 2 or 3 days. The total viable counts (TVC) were obtained by enumerating the colonies present, and calculated as log10 colony forming units (cfu)/g of the sample.

2.3 Electronic nose system

An electronic nose system was developed to obtain the

smell patterns from the headspace of meat samples, the details of which are described elsewhere [1]. This electronic nose system contains an array of six tin oxide based Taguchi gas sensors obtained from Figaro Engineering TGS 8XX (with XX= 23, 25, 26, 31, 32 and 82).

In a typical measurement, the headspace from a meat sample is fluxed into the electronic nose sensor chamber. Pure nitrogen is used at a constant flow of 500 sccm to allow the volatile species from the headspace to reach the sensor chamber. The electronic nose response is sampled (1 sample/s) for a time interval of 50 min. After the 50 min measurement, nitrogen is flushed again to clean the system until the steady state baseline resistance of the sensors is reached.

3. Results and discussion

3.1 Bacterial analysis

Fig. 1 shows the evolution in the counts of bacteria (log10 cfu/g) with the number of storage days for the two meats studied. A similar behavior can be observed for the two types of meat analyzed. A slight variation in the first five days followed with a very fast increase between days five and ten, and finally in the last days of conservation the curves show a tendency to stabilize. In addition, we notice that the cfu increases at a slightly higher rate in sheep meat then that in beef meat. Fig. 2 reveals also that the threshold of consumption acceptability (i.e., microbial counts < 6 log10 cfu/g) [2] should be set at day seven for beef meat and at day five for sheep meat.

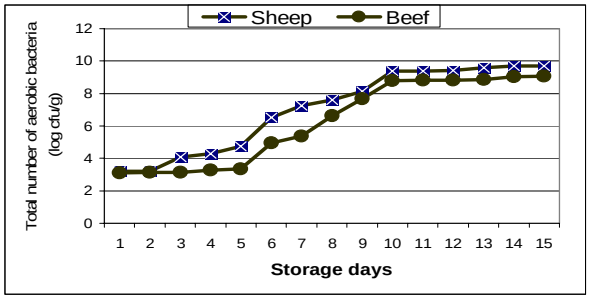

Fig. 1: Changes in the count of aerobic bacteria

3.2 Electronic nose analysis

3.2.1 SVM analysis

In the second step SVM was employed for analyzing the meat datasets. Considering the results of the bacteriological analysis we divided the dataset in two categories defined as spoiled and unspoiled samples. SVM with the approach multi classes one vs. one has been used to develop a rule of decision to classify the observations of the dataset in spoiled/unspoiled samples. A leave one out technique was used to validate the classification models. A very good success rate in classification was obtained in the spoilage classification of beef and sheep meats, (98.81 % and 96.43 %) respectively.

3.2.1Correlation between e-nose and bacterial analysis

The training phase and the prediction ability of the different PLS models built were evaluated. For each meat product, the response matrix, R (84 × 24), was split into different matrices: training matrix and validation matrix. In fact, three different training and their corresponding validation matrices were used (i.e. three-fold training and validation process).

A summary of the results of this study (for training and validation) for all the PLS models used to predict TVC in beef and sheep meats is shown in Table 1. Leave-one-out cross-validation technique is used in the training step. The predictions for validation measurements (i.e., not used for training) lie in the range of the predictions for training measurements. A very good correlation between the electronic nose results and bacterial analysis is obtained. In fact, correlation coefficients of 0.96 and 0.84 in training and validation are obtained for beef meat, respectively. Similarly, in the case of sheep meat, correlation coefficients of 0.92 and 0.83 in training and validation were obtained, respectively. This good agreement can be explained by the electronic nose system analyzes the development of component volatiles that result from the bacterial degradation of meat. Therefore, the electronic nose could be used as a rapid and alternative way for TVC prediction in red meats.

Table 1: Training (Tr) and validation (Va) regression coefficients of the PLS models.

	Beef			Sheep		
	Tr	Va	LVs	Tr	Va	LVs
Fold 1	0.95	0.88	7	0.93	0.80	11
Fold 2	0.99	0.72	21	0.93	0.84	11
Fold 3	0.94	0.93	7	0.9	0.86	9
Average	0.96	0.84	11	0.92	0.83	10

4. Conclusions

The correlation between the e-nose system and the bacteriological analysis was investigated. A very good correlation existed between the e-nose and bacteriological analysis results (the correlation coefficients for beef meat in training and validation were (0.96 and 0.84) and for sheep meat were (0.92 and 0.83). Therefore, the electronic nose could be used as a rapid and reliable method for the quality control of red meat on opposite of bacterial analysis that is required 2-3 days for colony formation. The electronic nose system can become an alternative tool for shelf-life determination and spoilage classification of red meats.

References

[1] N. El Barbri et al., "Electronic nose based on metal oxide semiconductor sensors as an alternative technique for the spoilage classification for red meat", IEEE International Workshop on Intelligent Data Acquisition and Advanced Computing Systems: Technology and Applications, 6-8 September 2007, Dortmund, Germany.

[2] S. Panigrahi et al., "Design and development of a metal oxide based electronic nose for spoilage classification of beef", Sensors and Actuators B 119, pp. 2–14, 2006.

Porous alumina for gas sensor applications

R.Calavia[a], A. Mozalev[b], V. Khatko[a], X. Correig[a], E. Llobet[a]

[a]Dep. Electrònica, Rovira i Virgili University, Tarragona, Spain
[b] *Department of Micro- and Nanoelectronics, Belarusian State University of Informatics and Radioelectronics, Brovka Str. 6, Minsk 220013, Belarus*

Abstract

Micromachined gas sensors have several very interesting characteristics, as for example the low power consumption. This characteristic is based on the low area to be heated, but it is interesting to increase the active area in order to improve their sensitivity. One possibility in order to improve the behavior of the sensors is based on the deposition of a porous alumina layer filled by the sensing material or use porous alumina in order to obtain nanorods of the active material. Both possibilities lead to an increase in the area exposed to the gas.

1. Introduction

The sensitivity of gas sensors depends on the size of the area in contact to the gas. As micromachined sensors have a very low electrode area in order to decrease the power consumption, it would be very interesting to increase the area of the active material in contact to the gas without increasing the area for heating.

One option to increase the sensing area without increasing the area for heating is based on the deposition of a porous alumina layer on the silicon oxide, between the heater and sensing material layer. So, it is possible to cover the surface of the porous alumina using the sensitive material and the surface of the pores, which leads to a very significant increase of the area in contact to the gas [1]. Figure 1 shows a first attempt to make a gas sensor out of such a process.

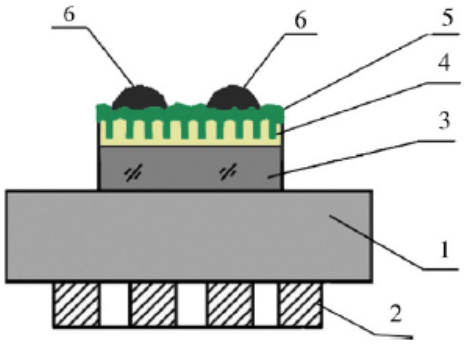

Fig 1. Schematic view of a gas sensor covered by a porous alumina layer: 1, ceramic substrate; 2, Pt heater; 3,piece of oxidized Si wafer; 4, porous alumina; 5, WO3 active layer; 6,
electric contacts.

2. To obtain porous alumina

The first step in order to obtain the porous alumina on the silicon wafer is the deposition of the aluminum layer on the surface of the silicon wafer. In this case this layer is deposited by magnetron sputtering and between the silicon oxide and the aluminum layer there is a titanium layer in order to evenly distribute the electrical current during the electrochemical process of anodization.

In order to obtain the porous alumina layer it is necessary an electrochemical process called anodization process. This electrochemical process oxidises the surface of the aluminium layer in contact to an acid electrolyte and in the minimum locals in the imperfections on the surface of the aluminium layer starts the growth of the pores.[2]

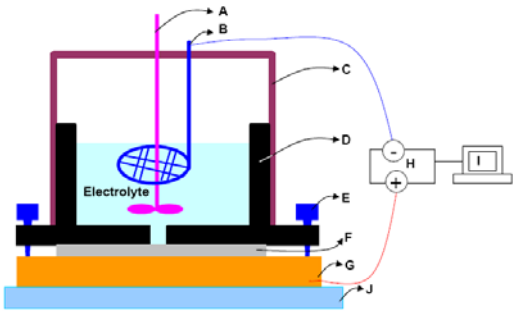

Fig. 2. Schematic diagram of the apparatus used for the anodization. A: Motor-controlled rotator for agitating the electrolyte, B: Pt mesh working as counter electrode, C: isolator consisting of an outer styrofoam layer and inner brass layer, D: electrolyte container made of teflon, E: screw for fixing the electrolyte container to the brass plate, F: aluminum sheet, G: brass plate working as electric conductor connected with a positive electric source, H : potentiostat/galvanostat (Keithley), and I: computer to operate the potentiostat/galvanostat and the cooling, J: Peltier cooling element.

The porous alumina obtained by this process is unorganized and in order to obtain self organized porous alumina it is necessary to use a process in two steps of anodising process, where the second anodising uses the end of the pores obtained in the first step as starting point for the pores in the second anodising process[3].

Cover the porous alumina using the active layer is one of the possibilities for increasing the size of the active area exposed to the gas (Fig 4). Another possibility is based in continuing the anodizing process when the pores arrive to the end of the aluminum layer, so the pores do not stop their growth. For example, when a Tungsten/ aluminum bilayer is deposited, after the removal of the porous alumina layer we obtain tungsten oxide nanorods that could be used as gas sensitive layer. These nanorods would lead to an increase in the area of the active layer exposed to the gas (Fig 3). [4].

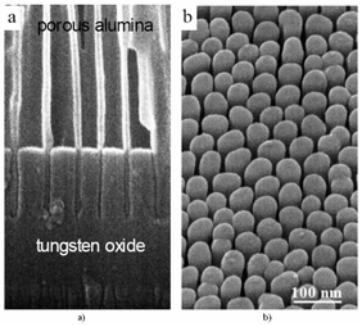

Fig. 3. WO_3 Nanorods growth steps. Pores growth in WO_3 layer (a) Nanorods obtained after extraction of the porous alumina layer (b)

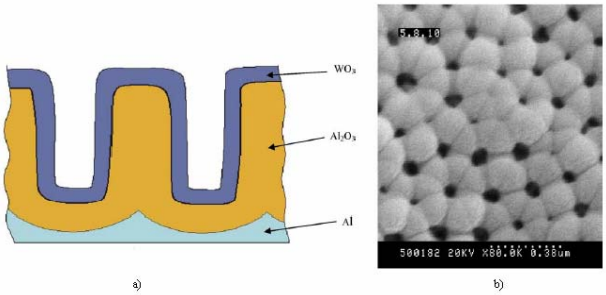

Fig 4. Porous alumina coated by WO_3, schematic sketch of the pores obtained by tartaric acid (a) and SEM image of the surface (b)

3. Conclusions

We are developing a procedure to make compatible the technology of microsystems with the anodization of aluminum. Either as a support or a template, anodized alumina could help obtaining films with very high surface area with many applications in the fields of gas sensors, microreactors, pre-concentrators or fuel cells.

References

[1] G. Gorokh a, A. Mozalev a, ,1, D. Solovei a, V. Khatko b, E. Llobet b, X. Correig b, “Anodic formation of low-aspect-ratio porous alumina films for metal-oxide sensor application”, electrochimica acta, available online 19 may 2006

[2] Jinsub Choi Doctoral tesis, “Fabrication of Monodomain Porous Alumina using Nanoimprint Lithography and its Applications”, ULB Sachsen-Anhalt, 2004

[3] H. Masuda and K. Fukuda, “Ordered metal nanohole arrays made by a two-step replication of honeycomb structures of anodic alumina,” Science, vol. 268, pp. 1466–1468, 1995.

[4] D. Solovei, G. Gorokh, A. Mozalev, “The growth of porous alumina films of the ordered morphologies by multi-step anodising process”, in: Book of Abstracts of the 55th Annual Meeting of the International Society of Electrochemistry (ISE), vol. II. Electrochemistry: From Nanostructured to Power Plants, Thessaloniki, Greece, September 19-24, 2004, p. 1023

Improvement of MS based e-nose performances by incorporation of Chromatographic retention time as a new data dimension

Cosmin Burian, Maria Vinaixa, Jesus Brezmes and Xavier Correig

Department of Electronic Engineering, Universitat Rovira i Virgili, Avenida Paisos Catalans 26, 43007 Tarragona, Spain

Abstract

This paper presents the work done in order to improve the performance of mass spectrometry-based electronic noses using the time retention of a chromatographic separation as an additional dimension. Solutions of nine isomers of dimethylphenols and ethylphenols were used in this experiment. The gas chromatograph mass spectrometer response was analyzed with pattern recognition algorithms like principal component analysis (PCA) and fuzzy ARTMAP.

1. Introduction

The goal of this work is to improve the sensitivity and/ or selectivity of the MS electronic nose by using the combination of gas chromatography and mass spectrometry adding the third dimension representing the time parameter of the chromatographic separation. Also to optimize the analysis, different chromatographic retention times were investigated.

Even though in recent experiments the MS electronic nose has proven better than gas sensors based electronic noses, some complex mixtures have proved difficult to classify. In most of the cases the methods used for the classifications were two-way methods. By coupling a gas chromatograph to a mass spectrometer we have the possibility to extract more data adding the time dimension to the m/z fractions and their intensity.

2. Materials and methods

Methods. For the experiment design we looked at 2 aspects: the PCA of the 9 isomers mass spectra and their chromatographic retention time. To obtain the chromatographic retention time (Fig.1.), 9 solutions of 1% isomer in methanol containing only one isomer were prepared and analyzed. In order to see which of the 9 isomers has most alike mass spectra we performed a PCA of the theoretical mass spectra of each isomer (Fig.2.).

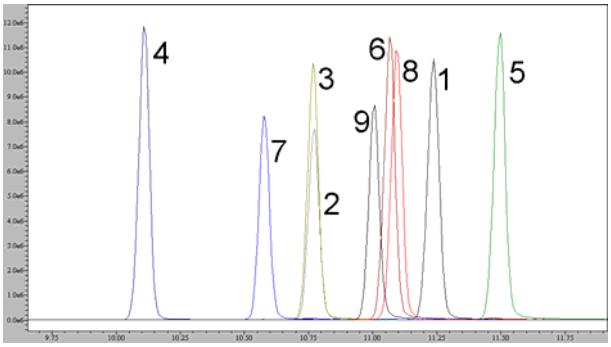

Fig.1. Chromatographic retention times for the 9 isomers as follows: **1)** 2,3-Dimethylphenol; **2)** 2,4-Dimethylphenol; **3)** 2,5-Dimethylphenol; **4)** 2,6-Dimethylphenol; **5)** 3,4-Dimethylphenol; **6)** 3,5-Dimethylphenol; **7)** 2-Ethylphenol; **8)** 3-Ethylphenol and **9)** 4-Ethylphenol;

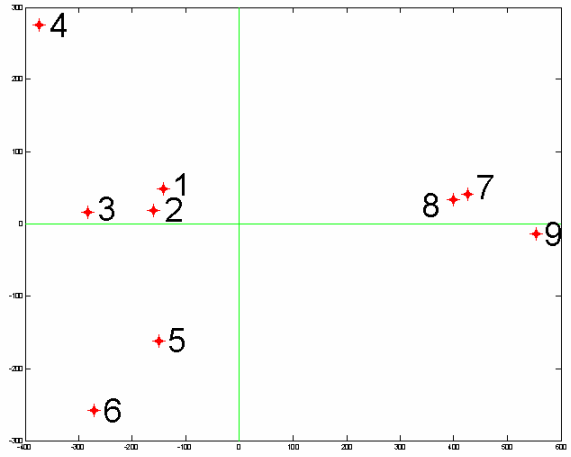

Fig.2. Principal Component Analysis of the isomers mass spectra

Based on this information we designed the experiment as shown in **Table 1.** Benzene acts as an internal standard, and having the highest concentration it is used in the normalization pretreatment of the data. We tried to make the experiment as complicated as possible in order to challenge the mass spectra-based electronic nose.

component	Sol1	Sol2	Sol3	Sol4	Sol5	Sol6	Sol7	Sol8	Sol9	Sol10	Sol11	Sol12	Sol13	Sol14	Sol15	Sol16	Sol17	Sol18	Sol19	Sol20
2,3-Dimethylphenol	-	0.5	0.5	0.5	0.5	0.5	0.5	0.5	0.5	0.25	0.5	0.5	0.5	0.5	0.5	0.5	0.25	0.5	0.25	0.5
2,4-Dimethylphenol	0.5	-	0.5	0.5	0.5	0.5	0.5	0.5	0.5	0.5	0.25	0.5	0.5	0.5	0.5	0.5	0.5	0.25	0.5	0.25
2,5-Dimethylphenol	0.5	0.5	-	0.5	0.5	0.5	0.5	0.5	0.5	0.5	0.5	0.25	0.5	0.5	0.5	0.5	0.5	0.5	0.5	0.5
2,6-Dimethylphenol	0.5	0.5	0.5	-	0.5	0.5	0.5	0.5	0.5	0.5	0.5	0.5	0.5	0.5	0.5	0.5	0.5	0.5	0.5	0.5
3,4-Dimethylphenol	0.5	0.5	0.5	0.5	-	0.5	0.5	0.5	0.5	0.5	0.5	0.5	0.5	0.5	0.5	0.5	0.5	0.5	0.5	0.5
3,5-Dimethylphenol	0.5	0.5	0.5	0.5	0.5	-	0.5	0.5	0.5	0.5	0.5	0.5	0.25	0.5	0.5	0.5	0.5	0.5	0.5	0.5
2-Ethylphenol	0.5	0.5	0.5	0.5	0.5	0.5	-	0.5	0.5	0.5	0.5	0.5	0.5	0.25	0.5	0.5	0.25	0.25	0.5	0.5
3-Ethylphenol	0.5	0.5	0.5	0.5	0.5	0.5	0.5	-	0.5	0.5	0.5	0.5	0.5	0.5	0.25	0.5	0.5	0.5	0.25	0.25
4-Ethylphenol	0.5	0.5	0.5	0.5	0.5	0.5	0.5	0.5	-	0.5	0.5	0.5	0.5	0.5	0.5	0.25	0.5	0.5	0.5	0.5
B/Et-OH/acetone	2%	2%	2%	2%	2%	2%	2%	2%	2%	2%	2%	2%	2%	2%	2%	2%	2%	2%	2%	2%

Table1. Experiment design (the numbers represent percentage of substance into methanol)

Three chromatographic methods were used. In method one we tried to separate as much as possible the isomers. To achieve this, a temperature programmed separation was used, starting at 50°C, where the temperature was kept constant for one minute, until 180°C, where almost all the isomers were separated. Method two and three were designed to give more coeluted peaks, and therefore isothermal separations. The temperatures used were used 175°C and 190°C respectively.

The measurements were conducted through syringe injection of 1 μl per measurement, and ten repetitions for each method and solution were made. Two blanks were also measured, one consisting of just methanol and the other with methanol and 2% of benzene.

3. Results and Discussion

The data collected from the GC-MS was arranged into a 3-D format that will display the separation time on the x axis, the m/z ratio on the y axis and the objects on the z axis. The data was separated, by adding one of the axis, into two groups of data. Group one is made by adding the time axis, giving the average mass spectra for each solution, and second group is made by adding the m/z axis, giving the total ion chromatogram.

These data was pretreated by normalization, and fed into a fuzzyARTMAP algorithm which tried to classify each solution.

The results are as follows:

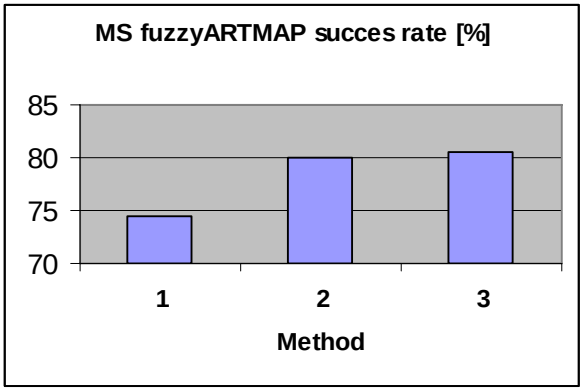

Fig.3. Mass Spectra fuzzyARTMAP success rate

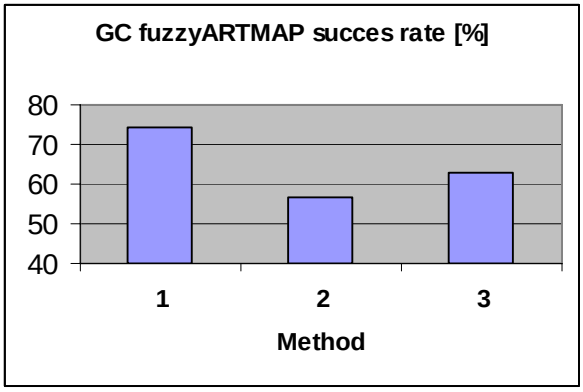

Fig.4. Chromatography fuzzyARTMAP success rate

The fuzzyARTMAP success rate shows that the algorithm is unable to completely classify the chosen solutions, giving room for future improvements.

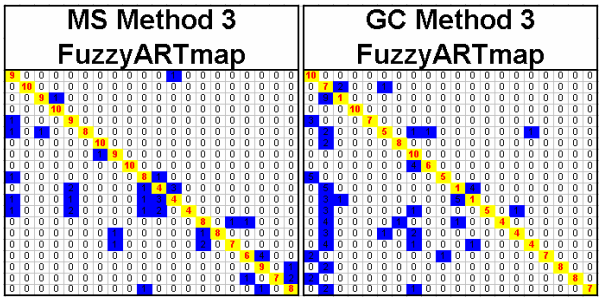

Fig.5. FuzzyARTMAP results for the Method 3 MS and GC (real (y) vs. predicted (x) solution)

Comparing the fuzzyARTMAP results (Fig.5.) we can see that the errors on the confusion matrix are quite different in the MS dimension and in the GC dimension. Therefore it is pretty clear that combining both dimensions can results in additional information which can be used to improve the mass spectra-based electronic nose performance.

4. Future Work

In order to improve the performances of the MS based electronic nose the data should be analyzed in a manner that involves analyzing both spectroscopic and chromatographic data at the same time. Therefore, the next step in this work is to use three-way models to combine both dimensions aiming towards the improvement of the electronic nose performance.

Analytical Modeling Framework for Short-Channel DG and GAA MOSFETs

H. Børli, S. Kolberg, and T. A. Fjeldly

[*]UniK – University Graduate Center, Norwegian University of Science and Technology, N-2021 Kjeller, Norway, {hborli, kolberg, torfj}@unik.no

Abstract

A modeling framework for nanoscale, short-channel double gate (DG) and gate-all-around (GAA) MOSFETs that covers a wide range of operating conditions is presented.

1. Introduction

To achieve sufficient accuracy in the analytical modeling of short-channel, nanoscale DG and GAA MOSFETs, the multi-dimensionality of the body potential and the electronic charge distribution has to be accurately accounted for. In sub-threshold, the device electrostatics is dominated by capacitive coupling between the electrodes. For the DG MOSFET, the 2D Laplace's equation can be conveniently solved by conformal mapping techniques, yielding analytical results [1-7]. We have shown that the DG results can be successfully applied to the GAA MOSFET as well, by performing an appropriate device scaling to compensate for the difference in gate control between the two devices [1-2]. This mapping is described in terms of the characteristic longitudinal field penetration lengths of the DG and GAA geometries [8-9].

Near and above threshold, the influence of the electronic charge on the electrostatics is taken into account in a precise, self-consistent manner by combining suitable model expressions with Poisson's equation. For finite drain voltages, the self-consistency also extends to a calculation of the quasi-Fermi potential and the drain current. In strong inversion, where the electronic charge dominates the device electrostatics, the behavior approaches that of long-channel devices [10-11].

The DG and GAA devices considered have gate length L=25 nm, silicon substrate thickness/diameter t_{si}=12 nm, and insulator thickness t_{ox}=1.6 nm.

2. 2D Capacitive Coupling

In devices with nanoscale gate length, the device electrostatics in the sub-threshold regime is dominated by capacitive coupling between the gate, source and drain electrodes. Previously, we have shown that in the DG MOSFET structure, the 2D potential distribution within the device body can be analytically determined by conformal mapping techniques based on Laplace's equation. Although the GAA MOSFET is a 3D structure, the DG MOSFET results can be successfully applied to the central, longitudinal cross-sections of the GAA structure as well, by performing an appropriate device scaling to compensate for the difference in gate control between the two devices [1-2]. This mapping is described in terms of the characteristic longitudinal field penetration lengths from source and drain of the DG and GAA MOSFET geometries [8-9].

3. Self Consistency

Near and above threshold, the carrier contribution to the body potential cannot be neglected. In this case, Poisson's equation is divided into two superimposed parts, the first of which is the 2D capacitive coupling described by Laplace's equation, as discussed above. The second part accounts for the electrostatic effects associated with the charge carriers, which must be derived in a self-consistent manner in agreement with Poisson's equation [1].

4. Results

The small dimensions of the present devices indicate that the drain current will have the character of both drift-diffusion and ballistic/quasi-ballistic transport. Here, we discuss a drain current model based on the classical drift-diffusion formalism.

The modeled and simulated drain currents are shown in the I_d-V_{GS} characteristics of Fig. 1 and in the I_d-V_{DS} characteristics of Fig. 2. An excellent agreement is observed between the modeling and the simulation results within the full range of bias conditions from sub-threshold to strong inversion. The slight undulations in the modeled curves result from transitions between different modeling regimes.

In Fig. 3, examples of the strong-inversion potential distribution along the Si-SiO_2 interface of the DG MOSFET are presented for three different values of drain bias. The maximum difference between the modeled potentials and the numerical simulations lies within a few millivolts.

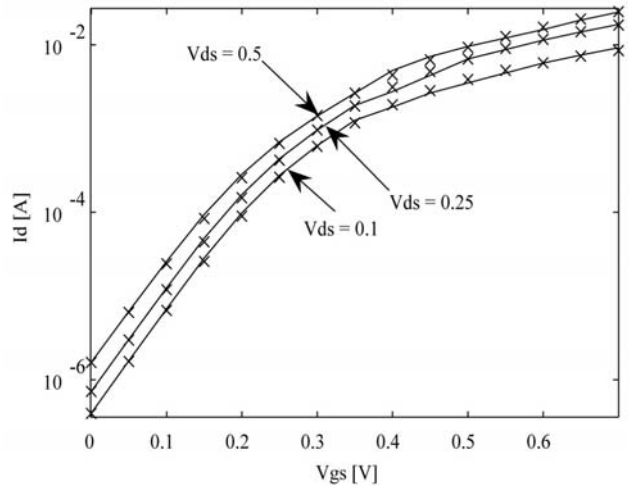

Fig. 1. Modeled transfer characteristics of the drain current of the DG MOSFET for three values of drain bias (solid curves). The symbols indicate numerical simulations performed with the Atlas device simulator.

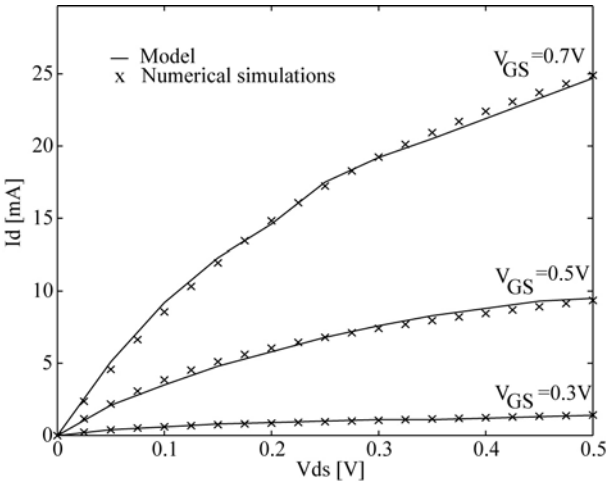

Fig. 2. Modeled strong-inversion I_d-V_{ds} characteristics of the DG MOSFET for three values of drain bias (solid curves). The symbols indicate numerical simulations performed with the Atlas device simulator.

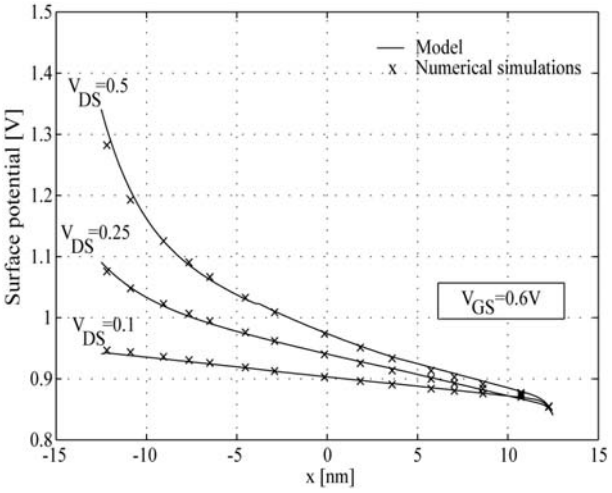

Fig. 3. Modeled near-threshold and strong inversion potential profiles (solid curves) of DG MOSFET along the Si-SiO_2 interface. The symbols indicate numerical simulations performed with the Atlas device simulator.

5. Spice-type modeling

The above modeling framework may serve as an excellent starting point for the development of more compact modeling expression suitable for use in circuit simulators. One possibility is to use a set of generic, semi-empirical expressions for the *I-V* characteristics with parameters that can be extracted to any desired accuracy from the framework.

6. Conclusions

We have developed a precise, compact 2D modeling framework for calculating the electrostatics as well as the drain currents in nanoscale, short-channel DG and GAA MOSFETs. The 2D modeling is based on conformal mapping techniques and a self-consistent analysis of the energy barrier topography, that include the effects of both the capacitive coupling between the contacts and the presence of inversion electrons. Short-channel effects, including DIBL, are inherently contained in this analysis, and no adjustable parameters are used. The modeling framework covers the full range of bias voltages from sub-threshold to strong inversion. Assuming a drift-diffusion transport mechanism, the drain current calculated from the present models and from numerical simulations show excellent agreement.

Acknowledgements

This work was supported by the European Commission under contract no. 506844 (SINANO) and the Norwegian Research Council under contract No. 159559/130 (SMIDA). We acknowledge the donation of TCAD tools from Silvaco and would like to thank Prof. Benjamin Iniguez from Universitat Rovira i Virgili, Spain for helpful discussions.

References

[1] H. Børli, S. Kolberg, and T. A. Fjeldly, , NSTI Nanotech 2007, pp.505-509, 2007.
[2] S. Kolberg, H. Børli, and T. A. Fjeldly, accepted, J. Math. and Comput. in Simulations.
[3] S. Kolberg and T. A. Fjeldly, J. Comput. Electronics, vol. 5, pp. 217–222, 2006.
[4] S. Kolberg and T. A. Fjeldly, Physica Scripta, vol. T126, pp. 57– 60, 2006.
[5] S. Kolberg, T. A. Fjeldly, and B. Iñiguez, Lecture Notes in Computer Science, vol. 3994, pp. 607 – 614, 2006.
[6] T. A. Fjeldly, S. Kolberg and B. Iñiguez, "Proc. NSTI Nanotech", vol. 3, Boston MA, pp. 668–673, 2006,.
[7] B. Iñiguez, T. A. Fjeldly, A. Lazaro, F. Danneville and M. J. Deen, IEEE Trans. Electron Devices, vol. 53, no. 9, pp. 2128-2142, 2006.
[8] K. Suzuki, Y. Tosaka, T. Tanaka, H. Horie and Y. Arimoto, IEEE Trans. Electron Devices, vol. 40, pp. 2326-2329, 1993.
[9] C. P. Auth and J. D. Plummer, IEEE Electron Dev. Letters, vol. 18, pp. 74-76, 1997.
[10] Y. Taur, X. Liang, W. Wang and H. Lu, IEEE Electron Dev. Lett., vol. 25, pp. 107-109, 2004.
[11] Iñiguez, B., Jiménez, D., Roig, J., Hamid, H.A., Marshal, L.F. and Pallarès, J.: IEEE Trans. Electron Devices, vol 52, pp. 1868-1873, 2005.

Sensing YSZ Nano-Material for Thermocatalytic Micromachined Gas Sensor with Improved Selectivity

R.G.Pavelko[1], A.A.Vasiliev[1], X.Vilanova[1], V.G.Sevastianov[2], V.Guarnieri[3], L.Lorenzelli[3], N.N.Samotaev[4]

[1]University Rovira i Virgili, Av. Paisos Catalans, 26, Tarragona, Spain
[2]Institute of General and Inorganic Chemistry, RAS, Leninskiy prosp., 31, Moscow, Russia
[3]Istituto Trentino di Cultura, ITC-irst, via Sommarive 18, 38050, Trento, Italy
[4]Moscow Engineering Physics Institute, 115409, Kashirskoe shaussee 31, Moscow, Russia

Abstract

A micromachined thermocatalytic sensor with improved catalyst support has been developed. The sensor is fabricated by deposition of Pd/Pt doped YSZ (120 m^2/g) on Si-micromachined substrate with Pt heater. Power consumption of the sensor is about 37 mW @ 450^0C per element (working and reference). Pt deposition technique assures the stability and bondability of Pt after thermal treatment. While the limit of the detection of alcohol and hexane was found to be about 0.05 vol. %, the device is completely insensitive to methane. These results enable the use of the sensors in the gas detectors applied in oil refineries, where low sensitivity of sensor to methane is important.

1. Introduction

Thermocatalytic (calorimetric) gas sensors are widely used for the detection of combustible gas concentrations close to low explosion level (LEL). The operation principle of these sensors is the detection of heat produced in an exothermal reaction of combustible gas oxidation. The main part of gas sensors of this type (for example, [1]) are fabricated by the deposition of catalyst (Pd/Pt doped alumina) on a spiral made of glass coated Pt wire (10 m in diameter). The catalyst is deposited as a suspension of alumina (with surface area of about 100 – 200 m^2/g), then the support is impregnated with Pt and Pd chloride drops and annealed at ~500^0C. The main disadvantage of this design and sensing material is the interaction of Al_2O_3 with glass and the formation of alumosilicates. For example after several month of operation of commercial available sensor (made by [1]) there is significant quantity of silicium in the bulk of catalyst support.

In this work, we used YSZ material as a carrier of Pd/Pt catalyst because at temperature below ~1500^0C it does not form solid solution with silicon oxide [2]. Silica impurity is concentrated on grain boundaries of this material. In addition, the catalysts based on carrier with mobile oxygen ions (like ceria-zirconia carrier) in contrast to Al_2O_3 give unambiguous sensor response.

2. Experimental.

As initial reagent we used yttria (8%) stabilized zirconia with surface area of 120 m^2/g produced by Sigma-Aldrich (Fig. 4). The material consists of big particles (200 – 300 nm), and therefore has large specific area corresponds to high internal porosity of particles. The material was impregnated consequently with water solution of $Pd(NH_3)_4(NO_3)_2$ and $Pt(NH_3)_4(NO_3)_2$ dried, and annealed at 600^0C. This material was deposited on microhotplate as ink in ethycellulose/terpineol, dried at 150^0C and annealed at 720^0C (15 min).

Microhotplate (Fig. 1) produced using silicon-based technology. Power consumption of the platinum heater at 450^0C was about 37 mW. The TCR is 2800 ppm/°C (20^0C).

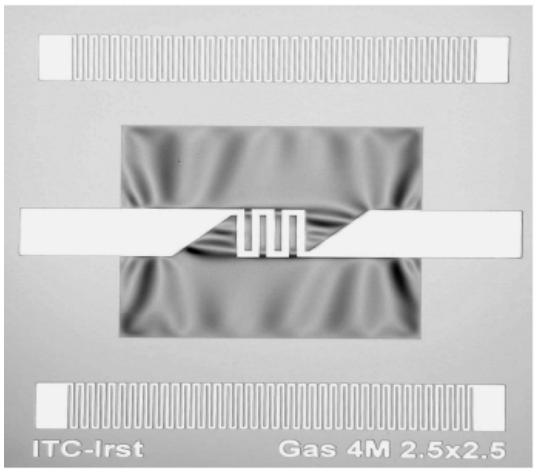

Fig. 1. Microhotplate (silicon technology) used for the deposition of thermocatalytic sensing layer. Chip size is of 2.2 x 2.7 mm^2, membrane size is of 1 x 1.5 mm^2, Pt heater size is of 300 x 300 μm^2. Side Pt resistors are designed for the measurement of ambient temperature.

3. Discussion.

The gas sensor response was measured using gas mixing installation with pre-mixed gas in bottles and computer controlled digital voltmeter. The response of the sensor was proportional to the change of current through the sensor heater at fixed heating voltage. This change is the result of additional heating due to thermal effect of the oxidation reaction.

The lack of contacting palladium clusters in YSZ sensing material leads to another sensitivity mechanism of the sensor compared to Pt/Pd doped alumina: the sensor is completely insensitive to methane. On the other hand, the sensitivity of the sensor to heavy hydrocarbons and oxygen containing organic compounds (alcohols, aldehydes) is high.

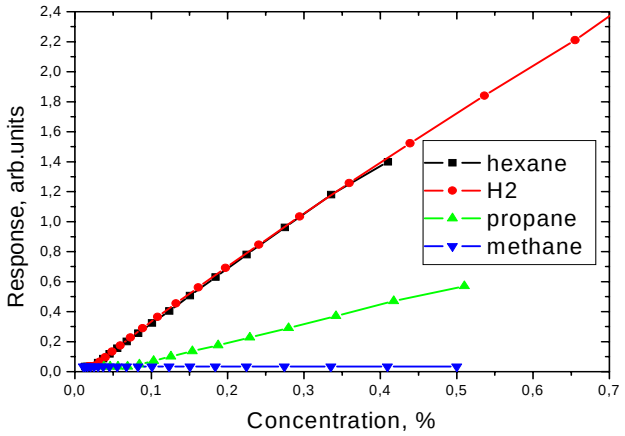

Fig. 2. Response of the Pd/Pt doped YSZ material as function of temperature. Concentration of all gases is equal to 1 vol. %.

Sensor response to different gases obtained with YSZ materials doped with platinum and palladium are presented in Fig. 2. The response in these figures is expressed as power produced in appropriate oxidation reaction. Pd/Pt doped YSZ sensing material gives only small negative response to CH_4 gas in whole temperature range due to higher heat conductivity of methane. On the other hand, the limit of the detection of hydrogen and hexane was found to be of about 0,01 vol. %. In contrast, the sensing element with Al_2O_3 based catalyst demonstrated comparable response to all combustible gases used in our experiments.

References:

[1] Technical information about thermocatalytic sensors: www.epris.ru

[2] F.M.B. Marques, V.V. Kharton, E.N. Naumovich, A.L. Shaula, A.V. Kovalevsky, A.A. Yaremchenko. Oxygen ion conductors for fuel cells and membranes: selected developments. Solid State Ionics, Vol. 177, Iss. 19-25, 2006, p. 1697-1703

An RFID Reader with gas sensing capability for monitoring fruit logistics

A. Vergara[1,*], E. Llobet[1], J.L. Ramírez[1], N. Cañellas[1], S. Zampolli[2], A. Scorzoni[3], S. Marco[4], L. Fonseca[5], T. Becker[6]

[1]University Rovira i Virgili, [2]CNR IMM-Bologna, [3]University of Perugia, [4]University of Barcelona, [5]CNM, [6]EADS

Avda. Països Catalans, 26, 43007 Tarragona, Spain, alexander.vergara@urv.cat

Abstract

We report the development of an RFID reader with onboard micro-machined metal oxide gas sensors aimed at monitoring in real time climacteric fruit during transport and vending. The developed platform integrates a commercial RF transceiver in the 13.56MHz band, ISO15693 compliant, micro-hotplate gas sensors, driving and readout electronics. By operating the sensors at an optimized temperature-modulation mode, the system has good potential to integrate a real time gas monitor for the application envisaged. The sensors are powered only during the measurement phase. 39 s are enough to get excellent performance, which helps in saving power.

1. Introduction

Nowadays food monitoring systems rely on expensive and bulky sensors suitable only for specific measurement tasks in laboratory environments. Therefore, there is a need for new devices capable of monitoring the quality and safety of food in real time, from the production site along the logistics chain into the hand of the consumer. This will enable producers, logistics groups and customers to trace their goods at any time, if needed. On the other hand, consumers will be protected against frauds as well as from the consummation of unsafe food.

In order to reduce the measurement time of the reader with on-board sensing capability, different approaches in signal processing and/or feature extraction have been investigated and developed. In this paper we explore the possibility to develop a real time RFID reader equipped with micro-machined metal-oxide semiconductor gas sensors by combining the characteristics given by an optimized thermal modulation together with pattern recognition and feature extraction methods. The signal processing methods implemented and the performance in the discrimination and semi-quantification of gases relevant to apple quality and safety during storage and transport are discussed in detail in the following sections.

2. Experimental

System architecture

A reader and a flexible tag micro-lab for monitoring climacteric fruit during transport and vending are under development in the framework of the FP6 Integrated Project "Good-Food". A prototype of the reader has the following characteristics: Based on TI MSP430 low power microcontroller, ISO15693 RFID communication, and Onboard gas sensors. Figure 1 shows the RFID reader and flexible tags and a picture of the RFID reader with 3 micro-sensor arrays. Fabrication of gas sensors is described below.

Figure1: The RFID reader with onboard gas sensing capability.

Micro-hotplate gas sensors

The reader can host up to 3 micro-sensor arrays, which implies up to 12 different micro-hotplate gas sensors. Every gas sensor array consisted of 1% Pt-doped and 1% Pd-doped tin and tungsten oxide (chips labelled A to D respectively). Basically, the structure of any sensor within the micro-array comprised a gas-sensitive layer, interdigited electrodes, insulating layers and a polysilicon heater, all stacked on a 0.2 μm thick Si_3N_4 membrane grown by LPCVD. The technological process needed to fabricate the substrates is summarized in [1]. The different sensing layers were deposited onto each micro-array by using a drop coating technique [2]. A paste was prepared dispersing the active material (SnO_2 or WO_3 nano-powders + 1% Pd or Pt) in glycerol. The paste was then drop-coated using a micro-injector (JBE1113 Dispenser, I&J FISNAR Inc., USA). The as-deposited films were annealed in situ at 480 ºC for 2 hours. The purpose of this process was to ensure a good adherence of the active material to the sensor substrates and to burn out the organic vehicle (i.e. glycerol) used in the paste.

Measurement set-up

The reader was placed in an air-tight test chamber. This

chamber was connected to a continuous flow system that allowed us to obtain, with high reproducibility, the different concentrations of gases (diluted in dry air) to be measured. Vapors of acetaldehyde (10, 50 and 100 ppm), ethylene (10, 50 and 100 ppm), ethanol (10, 25 and 50 ppm) and ammonia (25, 50 and 75 ppm) diluted in dry air were measured. Each measurement was replicated 5 times. Gas concentrations were obtained by computer-supervised mass-flow controllers. Measurements were performed while the operating temperature of the sensors was modulated using a multi-sinusoidal signal. The multi-sinusoidal signal resulted from the sum of 6 sinusoids of the same amplitude but different frequencies selected by an optimization process that involves using a multi-level pseudo-random maximum-length sequence [3]. The frequencies employed were 12.8 mHz, 25.6 mHz, 38.5 mHz, 92.9 mHz, 339.7 mHz and 682.7 mHz. Every measurement took approximately 312 s to complete (i.e., a complete cycle of the multi-sinusoidal signal). Before each measurement was performed, the sensors were not powered. Finally, measurements were repeated using a half, fourth and eighth part of the original signal (i.e.,156, 78, 39 s of measurement time (second, third and fourth data set respectively)).

3. Results and Discussions

Extensive tests to foresee the performance of the reader with onboard sensing capabilities have been run. Here we report on the study of its performance in the discrimination and semi-quantification of gases relevant to apple quality and safety during storage and transport. Therefore, 60 independent measurements per dataset of different concentrations of ethylene, acetaldehyde, ethanol and ammonia were conducted. The response signals were obtained and the absolute value of the FFT was computed. The values of the 6 harmonics corresponding to the modulating frequencies were extracted. These were the 6 features used to build identification and semi-quantification models. The dc component of the absolute value of the FFT was discarded because this is the mean value of the response signal, which is prone to be affected by drift.

Figure 2 shows the FFT spectra of the transient response of the Pd-doped SnO2 sensor in the presence of 50 ppm of ethylene. The peaks in the plots correspond to the temperature-modulating frequencies. Differences in the magnitudes of these peaks appear when the gas or gas concentration varies.

A fuzzy ARTMAP classifier was built and validated (using the leave-one-out approach) to discriminate among the different species (i.e. 4-category classification). Initially, the whole gas sensor response signal (i.e. 312 s of measurement time) was used to perform data analysis. See results in table 1.

A very high success rate in discrimination was reached, even using a single sensor (up to 100 %). When the information from sensors A and B was combined gases could be identified with a 100% success rate. Discrimination results when the whole response signals were used are summarized in Table 1.

Furthermore, by using a similar process than the one described above, fuzzy ARTMAP classifiers were built in order to obtain the discrimination success rate of the gases analyzed using the second, third and fourth data set respectively. A very high success rate in gas discrimination was obtained using a single sensors for the different data sets, while when sensors C and D were combined, correct discrimination peaked at 100 %.

Sensors→ Data set↓	A	B	C	D	C+D
312 s	71.66	95.00	96.66	100	100
156 s	71.66	93.33	96.66	98.33	100
78 s	70	95	98.33	95	100
39 s	68.33	96.33	95	86.66	100

Table1. Success rate in gas identification (%)

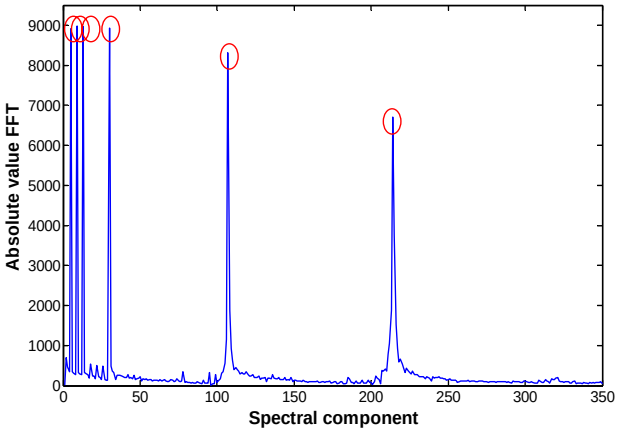

Figure2: FFT of the transient response of a temperature-modulated SnO_2 micro-hotplate sensor in the presence of 50 ppm ethylene.

In the second step a semi-quantitative analysis was envisaged. Once again different fuzzy ARTMAP classifiers were built and validated (using the leave-one-out approach) for the different data set (i.e., 312, 156, 78 and 39 s of measurement time) using a similar process than the one described for the qualitative analysis. Results reached are shown in table 2.

Sensors→ Data set↓	A	B	C	D	B+C
312 s	66.66	88.33	86.66	73.33	91.66
156 s	71.66	88.33	86.66	81.66	91.66
78 s	70	83.33	83.33	73.33	91.66
39 s	81.66	78.33	61.66	68.33	100

Table1. Success rate in gas semi-quantification (%)

References

[1] E. Llobet et al, Sens. Actuators B 83, 2002, 238-244.
[2] R. Ionescu et al., Sens. Actuators B, 113, 2006, 36-46.
[3] A. Vergara et al., Sens. Actuators B 123, 2007, 1002-1016.

Membranes in MEMS

R. Inglés[1*], J. L. Ramírez[1], J. Pallares[2]

[1]Dept. of Electronic, Electrical and Automatic Control Engineering, Universitat Rovira i Virgili Avd. Països Catalans, 26, 43007 Tarrragona. Phone: +34 977 558764, Fax: +34 977 559605, [*]E-mail: roser.ingles@urv.cat

[2]Department of Mechanical Engineering School of Chemical Engineering Universitat Rovira i Virgili Av. Països Catalans, 26, 43007 Tarragona

Abstract

In this paper we will review the state of the art in MEMS' membranes. We will study its thermal behaviour and power consumption. Finally we will present membranes simulations and propose further work.

1. Introduction

In this paper we will review the state of the art in membranes. Membranes are used in different devices but we will focus in two specific cases: the first one is membrane in MEMS used for hot plates in sensors. The second one is in preconcentrators.

The applications of micro hotplates, although, many and varied, share the same key design requirements: [1]

- ✓ fast response time
- ✓ low power consumption
- ✓ uniform plate temperature
- ✓ scalability

Preconcentrators are used to increase sensor sensitivity and/or selectivity[2]. They are used for detection of compounds that lay in air in trace concentrations. A vapor preconcentrator is designed in ref. [3] it is formed by a tube containing the adsorbent material and a resistive heater around the tube for thermal desorption. In [4] the use of a system that incorporates a preconcentrator, microfabricated from a fine microporous layer deposited on a membrane by means of sol-gel techniques, is reported to achieve efficient analyse collection and thermal desorption.

Temperature is one of the main factors which determine sensitivity, selectivity and response time of sensors. We will study this and power consumption in the next point of this paper. In the following point we will present our first simulations and finally we will propose further work.

2. Temperature and power consumption

Available micro heater resistor configurations: typically is used a square shaped membrane [5-8]. Simulation results, confirmed by thermographic analysis, have shown that optimum temperature uniformity is obtained with a double spiral shaped resistor. A minimum gradient of about 0.2 ºC/µm has been obtained. [5]

With all data of bibliography we have made a table where we have normalized data in order to compare structures. Table 1 shows data expressed in mW/ºCmm2. It was obtained from the ratio between the power consumption needed to reach a desired temperature at the surface of the membrane and the product of temperature and membrane area. The third dimension, membrane thickness, is not taken into as far as it has a second order effect. With this table we can obtain the graphic shown in figure 1. We can see that small membranes are less efficient that big membranes. In big membranes the most commonly value is 0.1 in mW/ºCmm2, so improve this value will be one of our objectives.

Author	*Year*	*mW / ºCmm2*	*Power (mW)*	*Temper. (ºC)*	*Dimensions (µm*µm)*	*Area (mm2)*
Swart[1]	***1994***	10,4167	8	120	80*80	0,0064
Solzbacher[9]	***2000***	8,75	35	400	100*100	0,01
Ducso[10]	***1997***	7,5	15	200	100*100	0,01
Bognar[11]	***2005***	4	20	500	100*100	0,01
Furjes[12]	***2006***	3,6291	18	496	100*100	0,01
Barretino[13]	***2004***	0,6667	1	6	500*500	0,25
Barretino[13]	***2004***	0,5714	1	7	500*500	0,25
Laconte[14]	***2002***	0,1220	20	400	640*640	0,4096
Astie[15]	***2000***	0,1805	65	450	1000*800	0,8
Baroncini[16]	***2004***	0,3	120	400	1000*1000	1
Briand[17] Cerda	***2000***	0,1833	55	300	1000*1000	1
Belmonte[18]	***2005***	0,1	50	500	1000*1000	1
Sberveglieri[8]	***1997***	0,1634	100	400	1700*900	1,53
Briand[17]	***2000***	0,1185	160	600	1500*1500	2,25
Briand[17]	***2000***	0,1111	75	300	1500*1500	2,25
Briand[17]	***2000***	0,1022	115	500	1500*1500	2,25
Rossi[19]	***1997***	0,08491	50	230	1600*1600	2,56
Plaza[20]	***2004***	0,1038	300	321	3000*3000	9

Table1. Comparative table

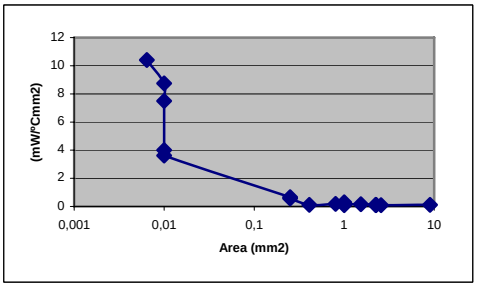

Fig 1 Power consumption to temperature and area unit ratio versus membrane area.

3. Simulations

We are running some simulations of our membrane electro-thermal behaviour. This is 1x3 mm2 membrane with an active area of 0.5x2.5 mm2. On top of this membrane there is a serpentine of platinum . At this point, we are characterizing the membrane without active material.

We simulate the thermal and electrical behavior in stationary mode. The membrane reaches a temperature of 200 ºC for a current of 20 mA through the platinum heater.

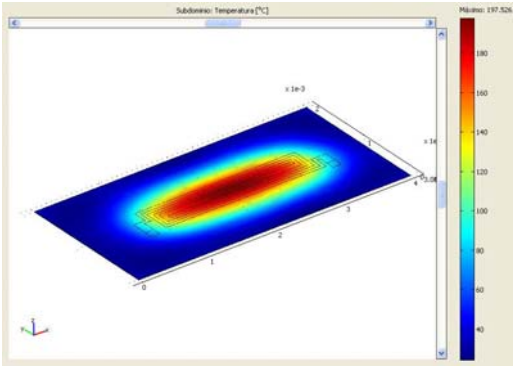

Fig 2 Temperature in membrane

At this point, the silicon bulk is not simulated in order to reduce simulation time. As far as membrane perimeter temperature is quite low, it seems that heat transfer to bulk is a second order effect that we can avoid in a first step approximation..

4. Conclusions and future work

Membranes have been much studied and the materials used, the shape and technology used determine the good work of the membrane. Big membranes are more efficient than small membranes. So a big membrane is better that two small ones.

Membranes used in preconcentrators are less studied than the ones used in sensors. In preconcentrators the peak of temperature is lower than in sensors (desorption values).

Our future work will be to simulate the behaviour in dynamic mode, so we will study the response for a voltage ramp. Then we will introduce the mechanical behaviour in order to avoid the breakdown of membrane reaching the biggest dimensions. And finally we will introduce the fluidic study.

References

1. Swart, N. and A. Nathan, *Design Optimization of Integrated Microhotplates.* SENSORS AND ACTUATORS A-PHYSICAL, 1994. **43**(1-3): p. 3-10.
2. Nakamoto, T., et al., *Odor-sensing system using preconcentrator with variable temperature.* SENSORS AND ACTUATORS B-CHEMICAL, 2000. **69**(1-2): p. 58-62.
3. Grate, J., N. Anheier, and D. Baldwin, *Progressive thermal desorption of vapor mixtures from a preconcentrator with a porous metal foam internal architecture and variable thermal ramp rates.* ANALYTICAL CHEMISTRY, 2005. **77**(6): p. 1867-1875.
4. Manginell, R.P., et al. *Microfabricated planar preconcentrator*. in *Solid State Sensor and Actuator Workshop*. 2000. Hilton Head, SC.
5. Dori, L., et al. *New material and heater geometry for high performance micromachined thermally insulated structures in gas sensor applications*. in *The Proceedings of Eurosensors XI*. 1997. Warsaw, Poland.
6. Cardinali, G., et al., *A smart sensor system for carbon monoxide detection.* ANALOG INTEGRATED CIRCUITS AND SIGNAL PROCESSING, 1997. **14**(3): p. 275-296.
7. Fung, S., et al., *Thermal analysis and design of a micro-hotplate for integrated gas-sensor applications.* SENSORS AND ACTUATORS A-PHYSICAL, 1996. **54**(1-3): p. 482-487.
8. Sberveglieri, G., W. Hellmich, and G. Muller, *Silicon hotplates for metal oxide gas sensor elements.* MICROSYSTEM TECHNOLOGIES, 1997. **3**(4): p. 183-190.
9. Solzbacher, F., et al., *A modular system of SiC-based microhotplates for the application in metal oxide gas sensors.* SENSORS AND ACTUATORS B-CHEMICAL, 2000. **64**(1-3): p. 95-101.
10. Ducso, C., et al., *Porous silicon bulk micromachining for thermally isolated membrane formation.* SENSORS AND ACTUATORS A-PHYSICAL, 1997. **60**(1-3): p. 235-239.
11. Bognar, G., et al., *Transient thermal characterisation of hot plates.* MICROSYSTEM TECHNOLOGIES-MICRO-AND NANOSYSTEMS-INFORMATION STORAGE AND PROCESSING SYSTEMS, 2005. **12**(1-2): p. 154-159.
12. Furjes, P., G. Bognar, and I. Barsony, *Powerful tools for thermal characterisation of MEMS.* SENSORS AND ACTUATORS B-CHEMICAL, 2006. **120**(1): p. 270-277.
13. Barrettino, D., et al., *Hotplate-based monolithic CMOS microsystems for gas detection and material characterization for operating temperatures up to 500(circle)C.* IEEE JOURNAL OF SOLID-STATE CIRCUITS, 2004. **39**(7): p. 1202-1207.
14. Laconte, J., et al. *Fully CMOS compatible low-power microheater*. in *Proceedings of the DTIP Conference*. 2002. Cannes.
15. Astie, S., et al., *Design of a low power SnO2 gas sensor integrated on silicon oxynitride membrane.* SENSORS AND ACTUATORS B-CHEMICAL, 2000. **67**(1-2): p. 84-88.
16. Baroncini, M., et al., *Thermal characterization of a microheater for micromachined gas sensors.* SENSORS AND ACTUATORS A-PHYSICAL, 2004. **115**(1): p. 8-14.
17. Briand, D., et al., *Design and fabrication of high-temperature micro-hotplates for drop-coated gas sensors.* SENSORS AND ACTUATORS B-CHEMICAL, 2000. **68**(1-3): p. 223-233.
18. Belmonte, J., et al., *High-temperature low-power performing micromachined suspended micro-hotplate for gas sensing applications.* SENSORS AND ACTUATORS B-CHEMICAL, 2006. **114**(2): p. 826-835.
19. Rossi, C., E. Scheid, and D. Esteve, *Theoretical and experimental study of silicon micromachined microheater with dielectric stacked membranes.* SENSORS AND ACTUATORS A-PHYSICAL, 1997. **63**(3): p. 183-189.
20. Plaza, J., et al., *A glass/silicon technology for low-power robust gas sensors.* IEEE SENSORS JOURNAL, 2004. **4**(2): p. 195-206.

Sensor Properties of WO_3 Thin Films RF Sputtered With Floating Regime

S. Vallejos[1], V. Khatko[1], J. Calderer[2], I. Gracia[3], C. Cané[3], E. Llobet[1], X. Correig[1]

[1]Departament d'Enginyeria Electronica, Universitat Rovira i Virgili, Campus Sescelades 43007 Tarragona, Spain
[2]Universitat Politecnica de Catalunya, Departament d'Enginyeria Electronica, Campus Nord 08034 Barcelona, Spain
[3]Centro Nacional de Microelectronica, Bellaterra 08193 Barcelona, Spain

Abstract

Tungsten trioxide sensing films were deposited by rf sputtering onto silicon micro-machined substrates. The sensing films were deposited using two sputtering technologies. First one included three interruptions of the deposition process. Second one comprised a deposition by using floating regime. It is shown that the sensor response to nitrogen dioxide is enhanced by the use of second technology.

1. Introduction

The high surface to volume ratio presented in the nano-grain metal oxides is a crucial factor in the gas sensor applications, since the sensitivity is directly related to this characteristic. One way to create metal oxide films with small grain size consists in using a special regime of thin film deposition by r.f. sputtering of pure metal target. This regime includes the thin film deposition with one or several interruptions of the deposition process [1]. We have observed in previous studies that the use of this regime allows decreasing the grain size in WO_3 thin films from 24 nm to 17 nm [2]. We have determined as well that the gas sensor responses of the WO_3 films deposited with interruptions to ozone and NO_2 were up to 4 times higher that those ones deposited using the basic regime [3, 4]. The other way is related with the use of a floating regime, which involves the thin film deposition with interruptions but at two different sputtering power densities. As a rule a low power deposition rate is set during the initial state of the thin film deposition and a high deposition rate is used during the final stage of the deposition. The aim of this work is to study the influence of the floating regime deposition on the morphological and sensing properties of the WO_3 thin films.

2. Experimental

Tungsten trioxide sensing films were deposited by reactive rf sputtering onto silicon micro-machined substrates (see Fig. 1). More detailed information about substrate fabrication is presented in [5].

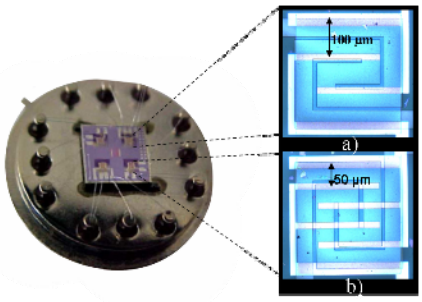

Fig. 1. On the left: view of the micro-array mounted on a standard TO-8 package. On the right: detailed views of the micro-machined sensor membranes. Interdigitated electrodes with spacing between fingers of 100 µm (a) and 50 µm (b).

The sensing films were deposited using two sputtering regimes. First one included three interruptions of the deposition process (S_i). The sputtering power was 100 W and the interruption time was 1.5 min. Second one comprised a deposition by using floating regime (S_f). The thin film was deposited with three interruptions in the first two interruptions the sputtering power was 100W and in last one the sputtering power was set to 280W. In fig. 2 it is shown a schematic illustration of the two types of active layers prepared. The active layer thickness was 0.2 µm approximately. After deposition the thin films were annealed at 400 ºC during 2 h. In order to investigate the WO_3 gas sensing properties to NO_2 (1 ppm, 2 ppm) the sensors were placed in a test chamber. Dry air was used as reference gas. The flow rate was 100 sccm. The sensor response was defined as R_{gas}/R_{air}.

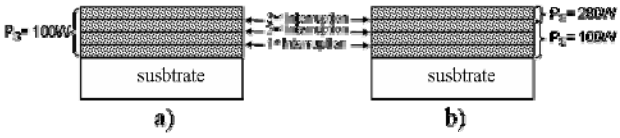

Fig. 2. Schematic illustration of the two deposition technologies used. Thin film deposited by interruption regime (a). Thin films deposited by floating regime (b). Ps: Sputtering power.

3. Results and discussions

3.1. Film morphology

The morphology of the thin film was analyzed by Atomic Force Microscopy in tapping mode. Fig. 3 shows the topography images of the WO_3 thin films deposited with interruptions and floating regime. No substantial difference in grain size (~11 nm) and roughness (~0.30 nm) was observed. This result was not expected because according to Ref. [6] grain size in WO_3 film should decrease when the sputtering power increase (i.e. films deposited by floating regime should have smaller grains). It is possible that the grain size is delimited by the diameter of the AFM tip (~10 nm). Therefore, if the grain size decreased in a range less than 10 nm the AFM tip used in this case could not show us the differences in samples.

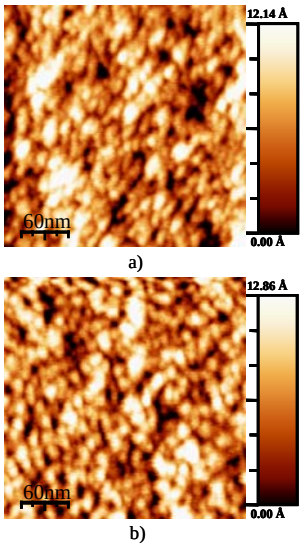

Fig. 3. AFM topography image of the thin films deposited with interruptions (a) and floating (b) regime. Scan area 300 x 300 nm.

3.2. Gas sensitivity studies

Fig. 4 shows the normalized responses (R_{gas}/R_{air}.) of the films deposited by interruptions and floating regime to 1 ppm and 2 ppm of NO_2. The sensor operating temperature was 350 ºC, in the previous work we found that higher sensitivities were obtained at this temperature [4]. The experimental data shows that WO_3 thin films deposited by floating regime present up to 1.5 better responses than those one deposited by interruption regime. The introduction of "extra" interfaces into the thin film body and the increase of sputtering power density during deposition of the superficial layer influence the response of WO_3 films to nitrogen dioxide.

On the other hand, it is observed that the response of the films deposited both with interruptions and floating regime is higher in the sensors with a 100 µm electrode gap. The influence of electrode geometry on the sensor response was discussed in [3].

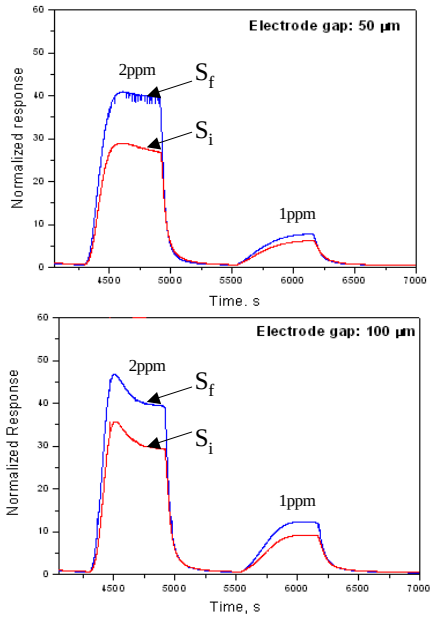

Fig. 3. Sensor response to 1 ppm and 2 ppm of NO_2. S_i : Active layers deposited with interruption. S_f : Active layers deposited by floating regime.

4. Conclusions

Tungsten trioxide sensing films were deposited by rf sputtering onto silicon micro-machined substrates. Two regimes of the sensing film deposition were used, first one with three interruptions and second one with floating regime. A clear enhancement of the sensor response to nitrogen dioxide was noticed for the WO3 films deposited with floating regime in comparison with the ones deposited with interruptions. The results of the study show the role of floating deposition regime in the WO_3 sensitivity to nitrogen dioxide.

References

[1] V. Khatko, J. Calderer, E. Llobet, X. Correig, Sens. Actuators B, Chem., 109 (2005) 128-134.

[2] V. Khatko, S. Vallejos, J. Calderer, E. Llobet, X. Vilanova, X. Correig, Sens. Actuators B, Chem., (2007) in press.

[3] S. Vallejos, V. Khatko, K. Aguir, K. Ngo, J. Calderer, I. Gràcia, C. Cané, E. Llobet, X. Correig, Sens. Actuators B, Chem., (2007) in press.

[4] S. Vallejos, V. Khatko, J. Calderer, I. Gràcia, C. Cané, E. Llobet, X. Correig, 32nd International Conference on Micro and Nano-Engineering MNE, (2006) Barcelona – Spain .

[5] M. Stankova, X. Vilanova, J. Calderer, E. Llobet, J. Brezmes, I. Gràcia, C. Cané, X. Correig, Sens. Actuators B, Chem., 113 (2006) 241-248.

[6] K. Wasa, S. Hayakawa, Hadbook of sputter deposition technology, Noyes publications, (1992).

A NEW ANALYTIC CHARGE AND CAPACITANCE MODEL FOR UNDOPED SYMMETRIC DOUBLE GATE MOSFETs

Oana Moldovan, Benjamin Iñiguez, David Jiménez* and Jaume Roig**

* Departament d'Enginyeria Electrònica, Escola Tècnica Superior d'Enginyeria, Universitat Autònoma de Barcelona, 08193-Bellaterra, Barcelona, Spain
** LAAS / CNRS, 7 avenue du Colonel Roche, 31077 Toulouse Cedex 4, France
e-mail: oana.moldovan@urv.cat

Abstract

Double-Gate (DG) fully depleted MOSFET architectures are promising candidates for ultra deep submicron VLSI technology since they allow a significant reduction of the short channel effects. Therefore, an accurate and CAD compatible DG MOSFET model is urgently needed. In the work by Sallese et al. [1], a unified charge control model for undoped symmetrical DG MOSFETs was developed, and from it a channel current model, was derived; this model was written in terms of the mobile charge sheet densities at the source and drain ends, but they had to be calculated iteratively. In this paper, we present analytical, explicit and continuous charge and capacitance models obtained from the unified charge control model derived by [1]. The drain current, charge and capacitances are written as analytical functions of explicit and continuous expressions of the mobile charge sheet density at the source and drain ends. Our model is valid from below to well above threshold, showing a smooth transition between the different regimes. A very important advantage of the new model is the absence of empirical parameters. We obtained very good agreement between the calculated capacitance characteristics and 2D numerical device simulations.

1. Model

An analytical expression of the total channel charge is obtained by integrating the mobile charge sheet density over the channel length (Q_{Tot}=-Q_G):

$$Q_{Tot} = -W^2 \frac{\mu}{I_{DS}} \int_{Q_s}^{Q_d} \left(\frac{Q^2}{2C_{ox}} + \frac{kT}{q} Q + \frac{kT}{q} \frac{Q^2}{Q+2Q_0} \right) dQ \qquad (1)$$

Following the Ward's channel charge partitioning scheme, we also obtain analytical expressions for the total drain (Q_D) and source (Q_S) charges, after integrating:

$$Q_D = -W \int_0^L \frac{x}{L} Q dx = -\frac{W^3 \mu^2}{L(I_{DS})^2} \int_{Q_s}^{Q_d} Q^2 \left(\left(\frac{Q^2 - Q_s^2}{4C_{ox}} \right) + \frac{kT}{q} \left(2(Q - Q_s) - 2Q_0 \log \left[\frac{Q+2Q_0}{Q_s+2Q_0} \right] \right) \right) \cdot \left(\frac{1}{2C_{ox}} + \frac{kT}{q} \left(\frac{1}{Q} + \frac{1}{Q+2Q_0} \right) \right) dQ \qquad (2)$$

$$Q_S = Q_{Tot} - Q_D \qquad (3)$$

Differentiating the total charges with respect to the applied bias, analytical expressions of all the capacitances are obtained in terms of the mobile charge sheet densities at the source and drain ends.

For the mobile charge sheet densities at the source and drain ends, we use explicit expressions of the same type as in [2] for Surrounding-Gate MOSFETs, since the charge control model considered here [1] has the same form as the one derived in [2].To validate our model, we have compared our modelled capacitance characteristics with 2D numerical simulations using DESSIS-ISE. We have also validated our drain current model. We have assumed L=1μm, W=1 μm, t_{ox}=2 nm, t_{Si}=20 nm and mobility equal to 300 cm^2/Vs.(Fig.1-6).

2. Conclusions

The modeled capacitance characteristics show excellent agreement with the 2D numerical simulations, in all operating regimes. Therefore, our model is very promising for circuit simulators.

References

[1]Jean-Michel Sallese, et.al. ".A design oriented charge-based current model for symmetric DG MOSFET and its correlation with the EKV formalism". *Solid-State Electronics*, vol.49, pp.485-489, December 2004

[2]Benjamin Iñiguez et.al., "Explicit Continuous Model for Long-Channel Undoped Surrounding Gate MOSFETs", *IEEE Transactions on Electron Devices*, vol.52, no.8, pp. 1868-1873, August 2005

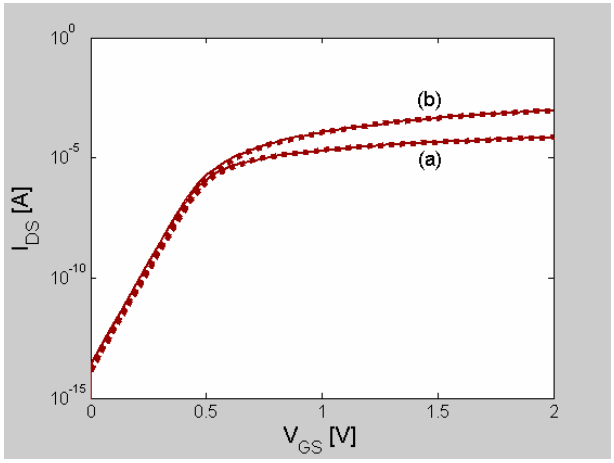

Fig. 1. Transfer characteristics, for V_{DS}=0.05V (a) and for V_{DS}=1V (b) in logarithmic scale. Solid line: DESSIS-ISE simulation; Symbol line: analytical model

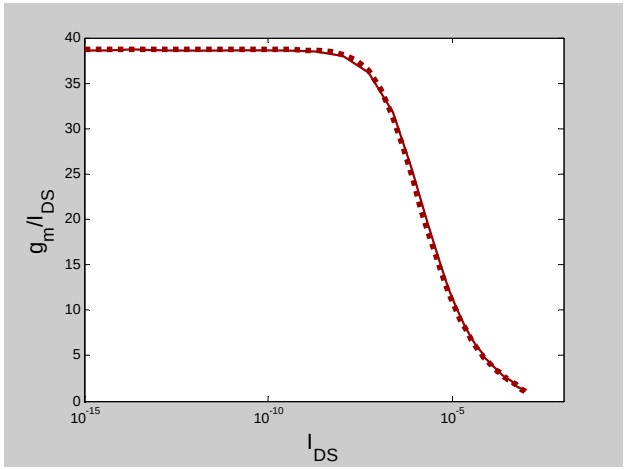

Fig. 2. g_m/I_{DS} versus I_{DS} for V_{DS}=1V. Solid line: DESSIS-ISE simulation; Symbol line: analytical model

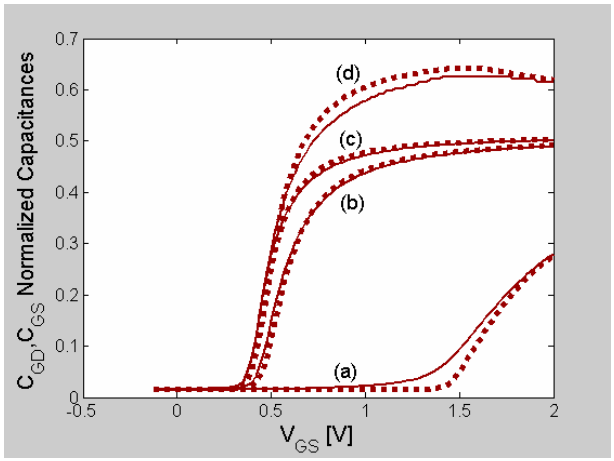

Fig. 3. Normalized gate to drain capacitance (a, b) and gate to source capacitance (c, d) with respect to the gate voltage, for V_{DS}=0.05V (b,c) and V_{DS}=1V (a,d). Solid line: DESSIS-ISE simulations; Symbol line: analytical model

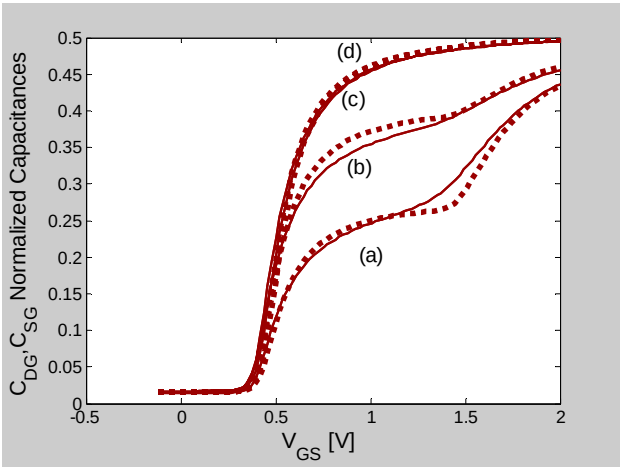

Fig. 4. Normalized drain to gate capacitance (a, c) and source to gate capacitance (b, d) with respect to the gate voltage, for V_{DS}=1V (a, b) and V_{DS}=0.05V (c, d). Solid line: DESSIS-ISE simulations; Symbol line: analytical model

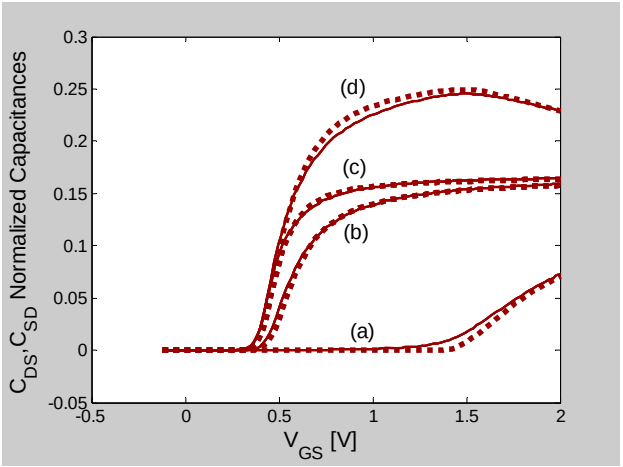

Fig. 5. Normalized source to drain capacitance (a, b) and drain to source capacitance (c, d) with respect to the gate voltage, for V_{DS}=1V (a, d) and V_{DS}=0.05V (b, c). Solid line: DESSIS-ISE simulations; Symbol line: analytical model

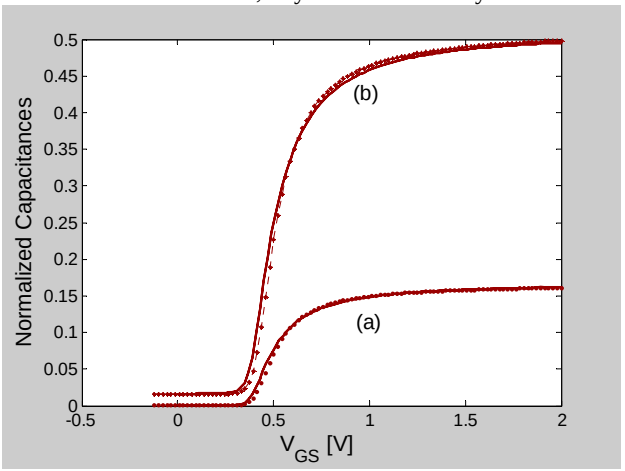

Fig. 6. Normalized drain-to-source capacitance and source -to-drain capacitance in (a), gate-to-drain capacitance, gate-to-source capacitance, drain-to-gate capacitance and source-to-gate capacitance in (b) for V_{DS} = 0 V (calculated as the limits of the capacitance expressions) Solid line: DESSIS-ISE simulations. Symbol line: analytical model.

Photonic bandgap analysis by transfer matrix method of liquid crystal infiltrated multilayers

Joaquín COS, Lluís F. MARSAL, Josep PALLARÈS y Josep FERRÉ-BORRULL

Nanoelectronic and Photonic Systems Group
D.E.E.E.A., Universitat Rovira i Virgili, Avda. Països Catalans 26, 43007 Tarragona, Spain
Contact: Lluís F. MARSAL (*lluis.marsal@urv.net*).

Abstract

In this work, we analyze the reflection characteristics of liquid crystal infiltrated multilayer by the transfer matrix method. This liquid crystal infiltration allow, in active way, the gap tuning (if we infiltrate one of the periodic structure) or the resonance tuning (if we infiltrate a defect of the multilayer). In order of characterize the liquid crystal's ordinary and extraordinary refractive indexes orientation we employ a transformation matrix defined by three angles.

Keywords: Optical multilayers; dielectric devices; photonic crystals; liquid crystal, matrix method.

1. Introduction

One-dimensional photonic crystal was known as optical multilayer since several decades. They play important roles as optical mirrors, interference edge filters, or antireflection coatings. Recent developments include the design of low-radiation-loss waveguide structures for optical interconnections on semiconductor wafers and the development of omnidirectional reflectors based on photonic bandgaps. Also, optical multilayer field has lately received a new and strong impulse due to its reinterpretation like one-dimensional photonic crystals.

On the other hand, due to the large optical anisotropic of liquid crystal, it's offer a very good opportunity in order to tune gaps and resonances.

In this work we analyzed numerically by Transfer Matrix Method the transmission properties of liquid crystal infiltrated multilayers.

2. Liquid crystal's optical axis orientation

Liquid crystal is a material characterized by two refraction indexes, ordinary and extraordinary. Optical axis orientation can be controlled by electric fields, temperature,... [1]. In this work we consider, in absence of external factors which could modify this orientation, X and Y axis for ordinary index and Z axis for extraordinary index.

In order to characterize the LC's optical axis orientation we must to define a transformation matrix which depend of the angles ϕ, θ and ψ, defined in the Fig. 1, and the dielectric constant tensor:

$$\tilde{\varepsilon} = A\begin{pmatrix} \varepsilon_o & 0 & 0 \\ 0 & \varepsilon_o & 0 \\ 0 & 0 & \varepsilon_e \end{pmatrix} A^{-1} = \begin{pmatrix} \varepsilon_{xx} & \varepsilon_{xy} & \varepsilon_{xz} \\ \varepsilon_{yx} & \varepsilon_{yy} & \varepsilon_{yz} \\ \varepsilon_{zx} & \varepsilon_{zy} & \varepsilon_{zz} \end{pmatrix} \quad (1)$$

where ε_o and ε_e are the ordinary and extraordinary dielectric constant and A is the coordinated rotation matrix and is defined by [2]:

$$A = \begin{pmatrix} cos\psi cos\phi - cos\theta sin\phi sin\psi & -sin\psi cos\phi - cos\theta sin\phi cos\psi & sin\theta sin\phi \\ cos\psi sin\phi + cos\theta cos\phi sin\psi & -sin\psi sin\phi + cos\theta cos\phi cos\psi & -sin\theta cos\phi \\ sin\theta sin\psi & sin\theta cos\psi & cos\theta \end{pmatrix} \quad (2)$$

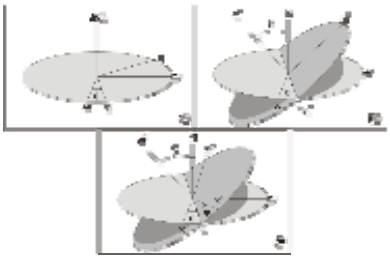

Fig.1. LC's optical axis orientation turns characterization. a) ϕ Angle. b) θ Angle. c) ψ Angle.

3. Transfer Matrix method

Anisotropic materials' transfer matrix method was generalized by Yeh [2]. This method is based in two kinds of matrixes, the dynamical matrix D and the propagation matrix P, which sizes are 4-by-4. In order to simplify equations, we are going to consider normal incidence (in Z axis) in this work.

With this commented normal incidence, the electric field of monochromatic waves assumes the following dependence $exp[i(\gamma z - \omega t)]$. To have a nontrivial plane-wave solution, we find the propagation constants γ of each layer from the determinant [3]:

$$\begin{vmatrix} \left(\frac{w}{c}\right)^2 \varepsilon_{xx} - \gamma^2 & \left(\frac{w}{c}\right)^2 \varepsilon_{xy} & \left(\frac{w}{c}\right)^2 \varepsilon_{xz} \\ \left(\frac{w}{c}\right)^2 \varepsilon_{yx} & \left(\frac{w}{c}\right)^2 \varepsilon_{yy} - \gamma^2 & \left(\frac{w}{c}\right)^2 \varepsilon_{yz} \\ \left(\frac{w}{c}\right)^2 \varepsilon_{zx} & \left(\frac{w}{c}\right)^2 \varepsilon_{zy} & \left(\frac{w}{c}\right)^2 \varepsilon_{zz} \end{vmatrix} = 0 \quad (3)$$

Eq. (3) gives us 4 roots γ which allow expressing the electric and magnetic fields in *j*-layer as lineal combination of 4 partial waves:

$$E^{(j)} = \sum_{\sigma=1}^{4} A_\sigma(j)\mathbf{p}_\sigma^{(j)} e^{i[\gamma_\sigma(j)(z-z_j)-\omega t]} \quad (4)$$

$$H^{(j)} = \sum_{\sigma=1}^{4} A_\sigma(j)\mathbf{q}_\sigma^{(j)} e^{i[\gamma_\sigma(j)(z-z_j)-\omega t]} \quad (5)$$

where **p** and **q** vectors are described as

$$\mathbf{p}_\sigma = N_\sigma \begin{pmatrix} \left(\frac{\omega}{c}\right)^2 \varepsilon_{zz}\left[\left(\frac{\omega}{c}\right)^2 \varepsilon_{yy} - \gamma_\sigma^2\right] - \left(\frac{\omega}{c}\right)^4 \varepsilon_{yz}^2 \\ \left(\frac{\omega}{c}\right)^4 \varepsilon_{yz}\varepsilon_{xz} - \left(\frac{\omega}{c}\right)^4 \varepsilon_{xy}\varepsilon_{zz} \\ \left(\frac{\omega}{c}\right)^4 \varepsilon_{xy}\varepsilon_{yz} - \left(\frac{\omega}{c}\right)^2 \varepsilon_{xz}\left[\left(\frac{\omega}{c}\right)^2 \varepsilon_{yy} - \gamma_\sigma^2\right] \end{pmatrix} \quad (6)$$

$$\mathbf{q}_\sigma^{(j)} = \frac{\gamma_\sigma}{\mu_0 \omega} e_z \times \mathbf{p}_\sigma^{(j)} \quad (7)$$

with N_σ defined as a normalization constant so that $\mathbf{p}_\sigma \cdot \mathbf{p}_\sigma = 1$.

From equations (6) and (7) we can define the dynamic matrix *D* in *j*-layer that has only dependence on polarization directions:

$$D(j) = \begin{pmatrix} e_x \cdot \mathbf{p}_1^{(j)} & e_x \cdot \mathbf{p}_2^{(j)} & e_x \cdot \mathbf{p}_3^{(j)} & e_x \cdot \mathbf{p}_4^{(j)} \\ e_y \cdot \mathbf{q}_1^{(j)} & e_y \cdot \mathbf{q}_2^{(j)} & e_y \cdot \mathbf{q}_3^{(j)} & e_y \cdot \mathbf{q}_4^{(j)} \\ e_y \cdot \mathbf{p}_1^{(j)} & e_y \cdot \mathbf{p}_2^{(j)} & e_y \cdot \mathbf{p}_3^{(j)} & e_y \cdot \mathbf{p}_4^{(j)} \\ e_x \cdot \mathbf{q}_1^{(j)} & e_x \cdot \mathbf{q}_2^{(j)} & e_x \cdot \mathbf{q}_3^{(j)} & e_x \cdot \mathbf{q}_4^{(j)} \end{pmatrix} \quad (8)$$

By other hand, the propagation matrix *P* in *j*-layer depends on propagation constants and the thickness of this layer:

$$P(j) = \begin{pmatrix} e^{-i\gamma_1^{(j)} d_j} & 0 & 0 & 0 \\ 0 & e^{-i\gamma_2^{(j)} d_j} & 0 & 0 \\ 0 & 0 & e^{-i\gamma_3^{(j)} d_j} & 0 \\ 0 & 0 & 0 & e^{-i\gamma_4^{(j)} d_j} \end{pmatrix} \quad (9)$$

With the definition of these two matrixes, we can define the *T* matrix which corresponds on the total transfer matrix of a structure composes of *N* periods of the two kinds of layers:

$$T = D^{-1}(air)D(1)P(1)\cdot(T_p)^{N-1}\cdot \cdot D^{-1}(1)D(2)P(2)\cdot D^{-1}(2)D(air)P(air) \quad (10)$$

where T_p corresponds with the transfer matrix of the two kinds of layers:

$$T_p = T_{1,2}T_{2,1} = D^{-1}(1)D(2)P(2)D^{-1}(2)D(1)P(1) \quad (11)$$

Due to the liquid crystal use, at first, there are coupling in the reflection/transmission, therefore is necessary to define four coefficient of this reflection/transmission, which are related with matrix of the equation (10) [2]:

$$R_{xx} = \left|\frac{T(2,1)T(3,3) - T(2,3)T(3,1)}{T(1,1)T(3,3) - T(1,3)T(3,1)}\right|^2 \quad (12a)$$

$$R_{xy} = \left|\frac{T(4,1)T(3,3) - T(4,3)T(3,1)}{T(1,1)T(3,3) - T(1,3)T(3,1)}\right|^2 \quad (12b)$$

$$R_{yx} = \left|\frac{T(1,1)T(2,3) - T(2,1)T(1,3)}{T(1,1)T(3,3) - T(1,3)T(3,1)}\right|^2 \quad (12c)$$

$$R_{yy} = \left|\frac{T(1,1)T(4,3) - T(4,1)T(1,3)}{T(1,1)T(3,3) - T(1,3)T(3,1)}\right|^2 \quad (12d)$$

$$T_{xx} = \left|\frac{T(3,3)}{T(1,1)T(3,3) - T(1,3)T(3,1)}\right|^2 \quad (13a)$$

$$T_{xy} = \left|\frac{-T(3,1)}{T(1,1)T(3,3) - T(1,3)T(3,1)}\right|^2 \quad (13b)$$

$$T_{yx} = \left|\frac{-T(1,3)}{T(1,1)T(3,3) - T(1,3)T(3,1)}\right|^2 \quad (13c)$$

$$T_{yy} = \left|\frac{T(1,1)}{T(1,1)T(3,3) - T(1,3)T(3,1)}\right|^2 \quad (13d)$$

3. Simulated results

From equations (10) and (12) we are going to simulate two kinds of structures. First, Bragg reflector composed by N cells formed by a first silicon layer ($n_{Si}=3.478$) and a second liquid crystal layer (type 5CB with $n_o=1.54$ y $n_e=1.72$), in which we vary the optical axis orientation. Finally, a Fabry-Perot composed by two reflectors (like the first structure) separated by a liquid crystal layer as cavity.

3.1. Bragg reflector

The multilayer analyzed in this section consists on the repetition 6 times of two materials H (high constant index) and L (low constant index). Where H corresponds on a silicon layer with thickness $d_H=2.3$ μm and L is a liquid crystal layer with thickness $d_L=1.7$ μm.

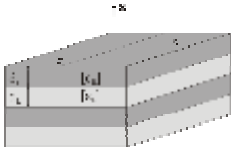

Fig.2. Schematic Photonic crystal structure.

In this last kind of layer, optical axis orientation's angles have fixed at $\theta=90^o$ and $\psi=0^o$, by other hand, angle ϕ rotates between 0^o to 90^o so that the ordinary and extraordinary indexes, that are in the X and Y axis respectively at $\phi=0^o$, are interchanging its positions up to $\phi=90^o$ where ordinary index is at Y axis and extraordinary index is at X axis.

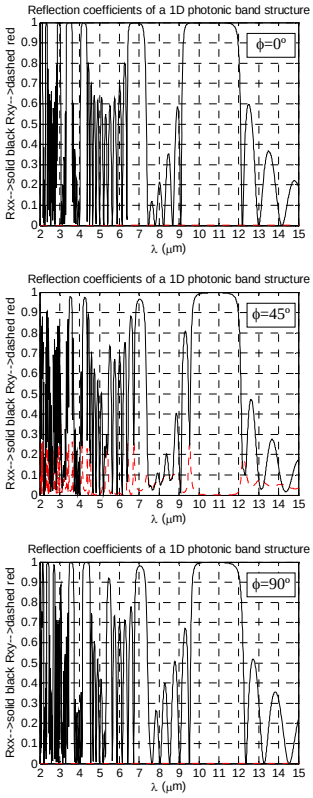

Fig.3. Reflection coefficients (X polarizations) of the 1D photonic crystal $(HL)^6$. H: Silicon (n_{si}=3.4, d_H=2.3μm). L: Liquid crystal E7 (n_o=1.54 n_e=1.72, d_L=1.7μm). Orientation θ=90º ψ=0º.ϕ=0º, 45º, and 90º.

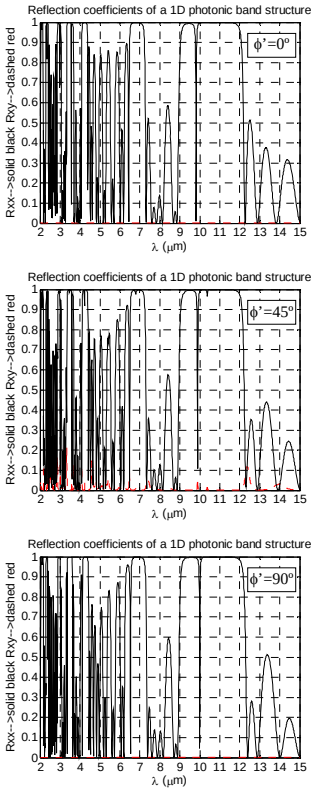

Fig.4. Reflection coefficients (X polarizations) of the 1D PC $(HL)^3$-L'-$(LH)^3$. H: Silicon (n_{si}=3.4, d_H=2.3μm). L: LC E7 (n_o=1.54 n_e=1.72, d_L=1.7μm) ϕ=0º θ=90º ψ=0º. L': LC E7 (d_L=2.55μm) θ'=90º ψ'=0º. ϕ'=0º, 45º, and 90º.

Figs. 3 show how for polarizations in X the gap has a red-shift as it increases the angle ϕ from *0º* to *90º*. By other hand, we can observe by means of the coupling coefficients (dashed lines) that for ϕ=*0º* and ϕ=*90º* there aren't coupling, whereas for the rest of the angles there are coupling because only for the first two situations ordinary and extraordinary indexes are purely oriented on X and Y axis.

3.2. Fabry-Perot structure

We study the tuning potential of structure with a resonance in the gap. This structure consists on Fabry-Perot composed by similar mirrors as the last section, but in this case we use 3 bi-layer periods in stead of 6. The cavity of the structure has a thickness of *d=2.55 μm*, filled by liquid crystal. LC's optical axis orientation on the mirror has fixed at ϕ=*0º*, θ=*90º* and ψ=*0º* while liquid crystal cavity has an optical axis orientation angles of θ'=*90º* and ψ'=*0º*, angle ϕ' rotate between *0º* to *90º* (in order to avoid confusions between mirrors and cavity LC's optical axis orientations we label the cavity set of angles with the superscript '). In the second mirror we truncate the layers order because of to keep symmetry with the other mirror.

Figs. 4 shows how we can tune the resonance since *9.81 μm* to *9.99 μm* for X polarization.

4. Conclusions

By means of a three angles' system we have characterized LC's optical axis orientation. With this characterization and the transfer matrix method we can obtain in a easily way the transmission and reflection properties and the coupling between the directions parallel to the multilayer polarizations of a uni-dimensional photonic crystal filled by liquid crystal.

In this work we have analyzed two structures. First, a photonic crystal mirror, which allows tuning its bandgap by means of i.e. voltage. Second, a Fabry-Perot filter composed by a LC cavity and two mirrors (similar to the first structure), with this structure we can tune the gap in a certain range.

As the results show, these structures can be used to design tunable and dynamical all-optical devices. Multilayer mirrors can be employed as tunable filters in a wide wavelength range. On the other hand, in the case of the analyzed Fabry-Perot, its capacity of tuning is very useful for the development of sensors, as well as controlled multiplexers devices by means of voltage.

Acknowledgements

This work was supported by the Spanish Ministry of Science under Grant number TEC2006-06531. J. Ferré Borrull acknowledges the Ramon y Cajal fellowship from the Spanish Ministry of Science and Technology.

References

[1] S. M. Weiss *et al.*, *"Electrical and thermal modulation of silicon photonic bandgap microcavities containing liquid crystals"*, Opt. Express, **13** (4) 1090-1097, 2005

[2] P. Yeh, *"Electromagnetic propagation in birefringent layered media"*, J. Opt. Soc. Am., **69** (5) 742-756, 1979.

[3] C. Vandenbem *et al.*, *"Tunable band structures in uniaxial multilayer stacks"*, J. Opt. Soc. Am. B, **23** (11) 2366-2376, 2006.

Analysis of tunable 2D silicon photonic crystals

Joaquín COS, Lluís F. MARSAL, Josep PALLARÈS y Josep FERRÉ-BORRULL

Nanoelectronic and Photonic Systems Group
D.E.E.E.A., Universitat Rovira i Virgili, Avda. Països Catalans 26, 43007 Tarragona, Spain
Contact: Lluís F. MARSAL (*lluis.marsal@urv.net*).

Abstract

A theoretical study of 2D photonic crystals composed of anisotropic materials is presented. We analyzed the TE and TM modes for a 2D silicon photonic crystal with liquid crystal scatters in the XY plane and a 2D liquid crystal photonic crystal with silicon scatters in the XY plane. First we analyzed different design parameters, as lattice, radius, etc, in order to perform a suitable band gap. Next, changes of the photonic band structures by varying liquid crystal's optical axis orientation in the XY plane are discussed. These structures can be used to design all-optical devices

Keywords: Liquid crystal, photonic crystal, photonic bandgap, plane-wave method.

1. Introduction

Photonic crystals (PCs) are synthetic materials in which the dielectric constant is periodically modulated. Since first proposed [4] [8] PCs have attracted much attention both experimentally and theoretically. Photonic crystals have inspired great interest among researchers due to their potential scientific and technological applications.

Furthermore, lately there are enough endeavors towards the direction of tuning the properties of photonic crystals in order to design switchable devices or dynamical devices. Various structures combining photonic crystals with nonlinear or liquid crystal (LC) materials have been proposed [2]. In the former case, a high-intensity control signal with frequency outside the bandgap changes the properties of the crystal [3].

On the other hand, the refractive index of liquid crystals can be varied either by changing the operating conditions or applying an external field [7].

In this work, we present a study and discussion of two 2D silicon photonic crystals infiltrated by liquid crystal. We base the analysis on plane-wave expansion method for TE and TM modes.

2. Theory

2.1. Numerical method

Firstly, we are going to present the Plane-Wave Method (PWM) and its application on PCs with LC infiltration. LC is a material that has an anisotropy uniaxial (it has an ordinary and extraordinary refraction index) at its nematic state. As we commented before, the orientation of its indexes can be controlled by voltage, temperature,… In this work we consider a variation of this LC's optical axis orientation in the XY plane (which it's the periodic plane of the PCs' rods). On this plane of variation there aren't coupling between TE and TM modes [1].

In order to characterize the LC's optical axis orientation we must to define a transformation matrix which depend of the Euler angles ϕ, θ and ψ, defined in the Fig.1, and the dielectric constant tensor:

$$\tilde{\varepsilon} = A\begin{pmatrix}\varepsilon_o & 0 & 0\\ 0 & \varepsilon_o & 0\\ 0 & 0 & \varepsilon_e\end{pmatrix}A^{-1} = \begin{pmatrix}\varepsilon_{xx} & \varepsilon_{xy} & \varepsilon_{xz}\\ \varepsilon_{yx} & \varepsilon_{yy} & \varepsilon_{yz}\\ \varepsilon_{zx} & \varepsilon_{zy} & \varepsilon_{zz}\end{pmatrix}, \qquad (1)$$

where ε_o and ε_e are the ordinary and extraordinary dielectric constant and A is the coordinated rotation matrix and is defined by [9]

$$A = \begin{pmatrix} cos\psi cos\phi - cos\theta sin\phi sin\psi & -sin\psi cos\phi - cos\theta sin\phi cos\psi & sin\theta sin\phi \\ cos\psi sin\phi + cos\theta cos\phi sin\psi & -sin\psi sin\phi + cos\theta cos\phi cos\psi & -sin\theta cos\phi \\ sin\theta sin\psi & sin\theta cos\psi & cos\theta \end{pmatrix}. \qquad (2)$$

In the absence of electric current and free charges, Maxwell equations for nonmagnetic media can be written as [6]

$$\nabla \times \mathbf{E}(\mathbf{r},t) = -\mu_0 \frac{\partial \mathbf{H}(\mathbf{r},t)}{\partial t}, \qquad (3a)$$

$$\nabla \times \mathbf{H}(\mathbf{r},t) = \varepsilon_0 \varepsilon(\mathbf{r}) \frac{\partial \mathbf{E}(\mathbf{r},t)}{\partial t}, \qquad (3b)$$

where μ_0 and ε_0 are the permeability and permittivity of the vacuum.

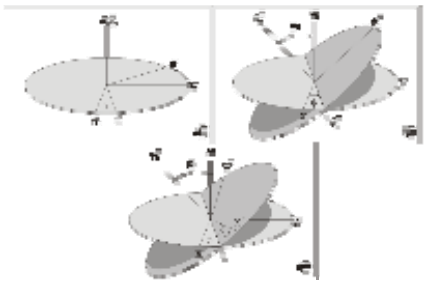

Fig.1. LC's optical axis orientation turns characterization. a) ϕ Angle. b) θ Angle. c) ψ Angle.

If we consider XY plane as the periodicity plane of the PCs we can obtain the next set of equations

$$\frac{\partial \mathbf{E}_z}{\partial y} = -\mu_0 \frac{\partial \mathbf{H}_x}{\partial t}, \quad (4a)$$

$$\frac{\partial \mathbf{E}_z}{\partial x} = -\mu_0 \frac{\partial \mathbf{H}_y}{\partial t}, \quad (4b)$$

$$\frac{\partial \mathbf{E}_y}{\partial x} - \frac{\partial \mathbf{E}_x}{\partial y} = -\mu_0 \frac{\partial \mathbf{H}_z}{\partial t}, \quad (4c)$$

$$\frac{\partial \mathbf{H}_z}{\partial y} = \varepsilon_0\varepsilon_{11}(\mathbf{r})\frac{\partial \mathbf{E}_x}{\partial t} + \varepsilon_0\varepsilon_{12}(\mathbf{r})\frac{\partial \mathbf{E}_y}{\partial t} + \varepsilon_0\varepsilon_{13}(\mathbf{r})\frac{\partial \mathbf{E}_z}{\partial t}, \quad (4d)$$

$$\frac{\partial \mathbf{H}_z}{\partial x} = -\varepsilon_0\varepsilon_{21}(\mathbf{r})\frac{\partial \mathbf{E}_x}{\partial t} - \varepsilon_0\varepsilon_{22}(\mathbf{r})\frac{\partial \mathbf{E}_y}{\partial t} - \varepsilon_0\varepsilon_{23}(\mathbf{r})\frac{\partial \mathbf{E}_z}{\partial t}, \quad (4e)$$

$$\frac{\partial \mathbf{H}_y}{\partial x} - \frac{\partial \mathbf{H}_x}{\partial y} = \varepsilon_0\varepsilon_{31}(\mathbf{r})\frac{\partial \mathbf{E}_x}{\partial t} + \varepsilon_0\varepsilon_{32}(\mathbf{r})\frac{\partial \mathbf{E}_y}{\partial t} + \varepsilon_0\varepsilon_{33}(\mathbf{r})\frac{\partial \mathbf{E}_z}{\partial t}, \quad (4f)$$

where the field notations are simplified as $\mathbf{A}_i(\mathbf{r},t)=\mathbf{A}_i$.

In order to classify TE and TM modes we consider a LC's optical axis orientation in the XY plane (as we can see in Fig.2), with this configuration the Euler's angles are $\phi=90^o-\alpha$, $\theta=90^o$ and $\psi=0^o$. The new dielectric constant tensor of the LC, ε_{LC}, which includes the LC's optical axis orientation, can be expressed as

$$\varepsilon_{LC} = \begin{pmatrix} \varepsilon_o sin^2\alpha + \varepsilon_e cos^2\alpha & (\varepsilon_o - \varepsilon_e)\cdot cos\alpha \cdot \sin\alpha & 0 \\ (\varepsilon_o - \varepsilon_e)\cdot cos\alpha \cdot \sin\alpha & \varepsilon_o cos^2\alpha + \varepsilon_e sin^2\alpha & 0 \\ 0 & 0 & \varepsilon_o \end{pmatrix}. \quad (5)$$

Without coupled modes we can eliminate $\mathbf{H}_x$ and $\mathbf{H}_y$ from Eqs. (4a), (4b), and (4f) and we can write the following eigenequation for the TE polarization:

$$-\varepsilon_{33}^{-1}(\mathbf{r})\left(\frac{\partial^2}{\partial x^2} - \frac{\partial^2}{\partial y^2}\right)\mathbf{E}_z(\mathbf{r}) = \omega^2\mu_0\varepsilon_0\mathbf{E}_z(\mathbf{r}). \quad (7)$$

On the other hand, eliminating $\mathbf{E}_x$ and $\mathbf{E}_y$ from (4c), (4d), and (4e) we obtain the following eigenequation for the TM polarization:

$$\nabla_{xy} \times \varepsilon_r^{-1}(\mathbf{r}) \times \nabla_{xy} \times \mathbf{H}_z(\mathbf{r})\hat{\mathbf{z}} = \hat{\omega}\mu_0\varepsilon_0\mathbf{H}_z(\mathbf{r})\hat{\mathbf{z}}, \quad (8)$$

where $\nabla_{xy} = \hat{\mathbf{x}}\cdot\partial/\partial x + \hat{\mathbf{y}}\cdot\partial/\partial y$ and $\varepsilon_r(\mathbf{r})$ is defined as

$$\varepsilon_r(\mathbf{r}) = \begin{pmatrix} \varepsilon_{11}(\mathbf{r}) & \varepsilon_{12}(\mathbf{r}) \\ \varepsilon_{21}(\mathbf{r}) & \varepsilon_{22}(\mathbf{r}) \end{pmatrix}. \quad (8)$$

In both equations (6) and (7) is assumed the solution $\mathbf{A}_z=\mathbf{A}_z(\mathbf{r})e^{-j\omega t}$ where ω is the angular frequency.

Applying plane-wave method on Eqs. (6) and (7) we can obtain a pair of eigenequations for TE and TM respectively [1]

$$\sum_{\mathbf{G}'}\varepsilon_{z\mathbf{GG}'}^{-1}\cdot(\mathbf{G}-\mathbf{G}')\cdot|\mathbf{k}+\mathbf{G}|\cdot|\mathbf{k}+\mathbf{G}'|F_{z,\mathbf{k}}(\mathbf{G}') = (\omega/c)^2 F_{z,\mathbf{k}}(\mathbf{G}), \quad (9a)$$

$$\sum_{\mathbf{G}'}(\mathbf{k}+\mathbf{G})\cdot\varepsilon_{r\mathbf{GG}'}^{-1}\cdot(\mathbf{G}-\mathbf{G}')\cdot(\mathbf{k}+\mathbf{G}')H_{z,\mathbf{k}}(\mathbf{G}') = (\omega/c)^2 H_{z,\mathbf{k}}(\mathbf{G}), \quad (9b)$$

where $\varepsilon_{z\mathbf{GG}'}^{-1}$ and $\varepsilon_{r\mathbf{GG}'}^{-1}$ are, respectively, the Fourier Transform of the inverse of $\varepsilon_{33}(\mathbf{r})$ and $\varepsilon_r(\mathbf{r})$ and c is the vacuum speed.

Fourier components of the inverse of the dielectric component can be defined for binary situations by

$$\varepsilon^{-1}(G) = \begin{cases} (f\cdot\varepsilon_c^{-1} + (1-f)\cdot\varepsilon_b^{-1}) & for\ G=0 \\ (\varepsilon_c^{-1} - \varepsilon_b^{-1})\cdot S(G) & for\ G\neq 0 \end{cases}, \quad (10)$$

where ε_b and ε_c are the dielectric constant for background and cylinders respectively and f is the filling factor. On the other hand, $S(G)$ relies only on the geometry of the cylinders and the lattice structures.

In this work we analyzed triangular lattice geometry with circulars rods. This geometry has larger photonic band gap (PBG) on TM modes than other geometries as square, honeycomb, kagome,… (Susa 2002). In Table 1., properties of triangular geometry are presented [5], a and R are lattice constant and radius of the rods respectively.

Base vector	$\mathbf{a}_1$	$a\,\hat{\mathbf{x}}$
	$\mathbf{a}_2$	$a(\frac{1}{2}\hat{\mathbf{x}} + \frac{\sqrt{3}}{2}\hat{\mathbf{y}})$
Reciprocal lattice base vector	$\mathbf{b}_1$	$(2\pi/a)\,(\hat{\mathbf{x}} - \frac{1}{\sqrt{3}}\hat{\mathbf{y}})$
	$\mathbf{b}_2$	$(2\pi/a)\,\frac{2}{\sqrt{3}}\hat{\mathbf{y}}$
Filling factor f		$\frac{2\pi}{\sqrt{3}}\,(R/a)^2$
$S(G)$		$2f\,\frac{J_1(GR)}{(GR)}$

Table 1. PCs triangular geometry properties.

2.2. Brillouin zone and geometry

Due to the liquid crystal anisotropy we must consider a larger Brillouin zone. In fact, the irreducible Brillouin zone depends on the LC's optical axis orientation [1]. For all the orientations we consider the same Brillouin zone in order to simplify the results comparisons. Fig. 2 shows considered irreducible Brillouin zones for triangular lattice.

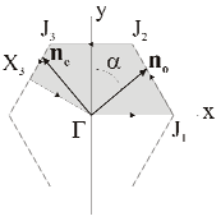

Fig.2. Irreducible Brillouin zone for Triangular lattice and LC's axis orientation (n_o, n_e).

3. Results and discussion

We perform the analysis of band structure of 2D PCs made of anisotropic material (E7 liquid crystal with $n_o=1.522$ $n_e=1.706$). The first structure is Silicon

(n_{Si}=*3.478*) PC with a triangular lattice of circular holes infiltrated by LC. The second structure is its inverse: LC photonic crystal with a triangular lattice of circular Silicon rods. We use 529 plane-waves in order to guarantee convergence of 8 first modes (with an error smaller than 1%).

3.1. Silicon PC with liquid crystal rods

In the previous theoretical analysis we have obtained an equation for TE modes that depend on $\varepsilon_{33}(\mathbf{r})$, therefore, TE modes do not depend on LC's optical axis orientation. TM modes depend on $\varepsilon_r(\mathbf{r})$ and need to be analyzed for different LC's optical axis orientation. Fig. 3 shows the variation of the PBG between 1st and 2nd modes versus radius of liquid crystal rods. For *R=0.401a* the normalized wide gap frequency is the largest.

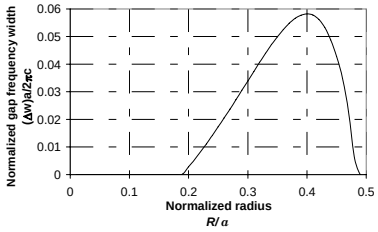

Fig.3. PGB between 1st and 2nd TM modes versus radius of LC rods in a triangular lattice (n_o=1.522, n_e=1.704, n_{Si}=3.478, α=0).

Next figures show an example of the photonic band structure of a 2D Silicon PC with LC infiltrated holes in a triangular lattice for all LC's optical axis orientations (TE modes, fig. 4) and α=*45º* (TM modes, fig. 5)

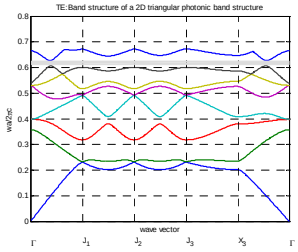

Fig.4. Photonic band structure (TE modes) of a 2D Silicon PC with LC infiltrated holes in a triangular lattice (R=0.401*a*, n_o=1.522, n_e=1.704 n_{Si}=3.478).

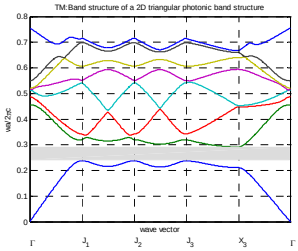

Fig.5. Photonic band structure (TM modes) of a 2D Silicon PC with LC infiltrated holes in a triangular lattice (R=0.401*a*, n_o=1.522, n_e=1.704 n_{Si}=3.478). α=45º

As we can see in fig. 5 there is a gap between modes 1st and 2nd. Depending on the LC's optical axis orientation this gap changes on position and width. This change allows tuning the bandgap in a certain range. First TM mode's maximum varies between *wa/2πc*=0.2379 (for α=0º) and *wa/2πc*=0.2380 (for α=30º), and second TM mode's minimum varies between *wa/2πc*=0.2900 (for α=30º) and *wa/2πc*=0.2961 (for α=0º). This tuning can be controlled by voltage, temperature or other operating conditions [7].

Fig. 6 shows an exhaustive analysis of complete band gap versus LC's optical axis orientation, it's important to stand out the 60º periodicity. Maximum gap (*wa/2πc*=0.0582) is for 60º and its multiples. By other hand, minima (*wa/2πc*=0.0520) are localized at 30º and at odd multiple degrees.

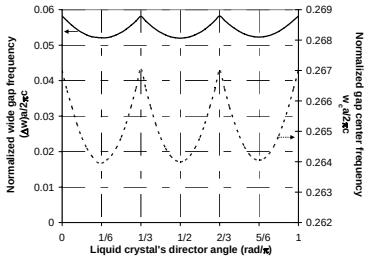

Fig. 6. Width (solid line) and center (dashed line) gap between 1st and 2nd TM modes analysis versus LC's optical axis orientation of Silicon PC with LC infiltrated holes in a triangular lattice (R=0.401*a*, n_o=1.522, n_e=1.704 n_{Si}=3.478).

3.2. Liquid crystal PC with Silicon rods

We analyze the inverse structure, a liquid crystal photonic crystal with a triangular lattice made of silicon circular rods. In this case, there is a gap between 4th and 5th TM modes for a certain range of radius. Fig. 7 shows the variation of normalized gap frequency width between 4th and 5th modes versus silicon rods radius. Here, for *R=0.218a* the PBG is the largest. The radius range with complete gap is smaller than for structure analyzed in section 3.1.

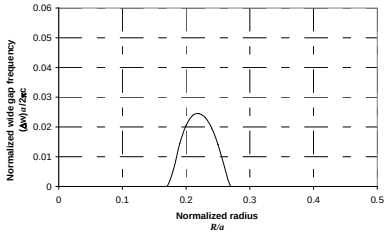

Fig.7. PGB between 4th and 5th TM modes versus radius of silicon rods in a triangular lattice (n_o=1.522, n_e=1.704, n_{Si}=3.478, α=0).

Fig. 8 presents dispersion curves for TE modes for all angles (as in section 3.1, TE modes do not depend on LC's optical axis orientation). In this case there is a gap between 1st and 2nd modes since *wa/2πc*=0.2493 (maximum of 1st mode dispersion curve) to *wa/2πc*=0.4480 (minimum of 2nd mode dispersion

curve). Fig. 9 shows dispersion curves for TM modes for LC's optical axis orientation $\alpha=45^{o}$.

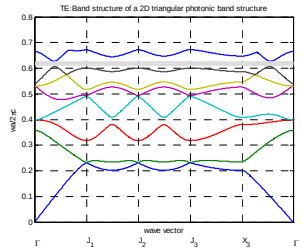

Fig.8. Photonic band structure (TE modes) of a 2D Liquid Crystal PC with silicon rods in a triangular lattice (R=0.218*a*, n_o=1.522, n_e=1.704 n_{Si}=3.478).

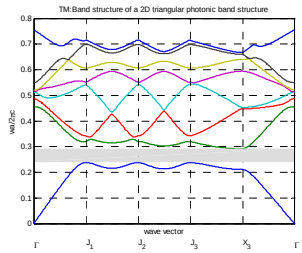

Fig.9. Photonic band structure (TM modes) of a 2D Liquid Crystal PC with silicon rods in a triangular lattice (R=0.218*a*, n_o=1.522, n_e=1.704 n_{Si}=3.478). α=45º

In this case, we can see how the gap is narrower than silicon PC with LC rods' case. Indeed, here is no gap for α=90º. Fig. 10 shows a most exhaustive analysis, the angle step is now 3.75º. As we can see, for a range of angle (82.5º – 97.5º) the gap disappears. This property can be used for the design of an optical switch, where varying LC axis angle (for example by means of voltage) we can modulate the complete band gap.

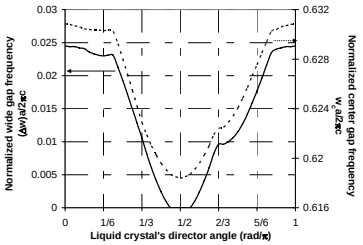

Fig. 10. Width (solid line) and center (dashed line) gap between 4th and 5th TM modes analysis versus LC's optical axis orientation of liquid crystal PC with silicon rods in a triangular lattice (R=0.218*a*, n_o=1.522, n_e=1.704 n_{Si}=3.478).

4. Conclusions

We have studied a structure based on silicon photonic crystal and liquid crystal that allows tuning a complete band gap. By means of the plane-wave expansion method we have analyzed the TE and TM modes. In particular, we have studied two structures, a silicon photonic crystal with liquid crystal infiltrated holes and a liquid crystal photonic crystal with silicon rods. For the first structure, the gap width has a 60º periodicity on the LC's optical axis orientation. Maximum gap is obtained for LC's optical axis orientation angles multiples of 60º and minimum for odd multiples of 30º. By means of a LC photonic crystal with silicon rods we have designed an optical switch, where for a range of LC's optical axis orientation (82.5º – 97.5º) the gap disappears. These structures can be used to design all-optical devices.

Acknowledgements

This work was supported by the Spanish Ministry of Science under Grant number TEC2006-06531. J. Ferré Borrull acknowledges the Ramon y Cajal fellowship from the Spanish Ministry of Science and Technology.

References

[1] G. Alagappan *et al., J. Opt. Soc. Am. A* **23** 2002, 2006.
[2] K. Busch and S. John, *Phys. Rev. Lett.* **83** 967, 1999.
[3] F. Cuesta-Soto, *et al., Opt. Express* **12** 161, 2004.
[4] S. John, *Phys. Rev. Lett.* **58** 2486, 1987.
[5] P. G. Luan and Z. Ye *Condensed Matter* **1** 0105428, 2001.
[6] K. Sakoda, *Optical Properties of Photonic Crystals*, Springer, 2001.
[7] S. M. Weiss, *et al., Opt. Express*, **13**, 1090, 2005.
[8] E. Yablonovitch, *Phys. Rev. Lett.* **58** 2059, 1987.
[9] P. Yeh, *J. Opt. Soc. Am.*, **69** 742, 1979.

Benzene Gas Sensors Response, Using Planar Gas Pre-Concentrator

F.Blanco[1*], P.Ivanov[2], M.Vinaixa[1], X. Vilanova[1], I.Gracia[2], C. Cané[2], X.Correig[1]

[1] DEEEA, Universitat Rovira i Virgili Avinguda dels Països Catalans, 26 Campus Sescelades, 43007 Tarragona (Spain)
[2] Gas Sensors Group, Centre Nacional de Microelectrònica, CNM-CSIC, Bellaterra, (Spain)

*Fernando Blanco, Departament d'Enginyeria Electrònica, Elèctrica i Automàtica,
Universitat Rovira i Virgili Avinguda dels Països Catalans, 26 Campus Sescelades, 43007 Tarragona (Spain)
Tel.: +34 977 558 764, Fax +34 977 559 605
e-mail: fernando.blancoc@urv.cat

Abstract

In this work, a low benzene concentration detector system is developed and characterized. It is based on increasing the concentration of the target gas by adsorbing it in specific carbon layer and desorbing it trough a temperature pulse. Two different type metal oxide sensors were used for measuring the benzene desorbed. Concentration factors of up to 344 were obtained allowing a significant improvement of the usual detection margins of a gas sensor.

1. Introduction

Benzene has become one of the most intensely regulated substances in the world, typical occupation exposure levels are currently at concentrations below of 3.25 mg/m^3 (1 ppm), and environmental exposure are typical below 50 µg/m^3 (15 ppb) [1]. For measuring low concentrations of this type of compound, gas chromatography, mass spectrometry and other techniques are used. These techniques are expensive, large and require significant expenditure maintenance and no permit measurements *in-situ*.
Some of these techniques employ gas pre-concentrators to increase the sensitivity and selectivity.

In this paper we propose the use of one gas pre-concentrator together with metal oxide gas sensors for detecting benzene. The pre-concentrator is based on experimental activated carbon (surface area 1300 m^2/g) obtained of Kraft Lignin [2], for creating a planar structure depositing approximately of 300 µg of material.

2. Previous Characterization

The technique of fabrication and characterization of the planar preconcentrador is previously reported in [3].
For this new material, exhaustive tests at different absorption times and fluxes were performed, using a fixed concentration of benzene in CO_2 of 150 ppb. These tests were performed using four different pre-concentrators in order to know their capacity to absorb benzene (Concentration Factor).

These results are show in the table 1.

Time Min.	CF. Flux 100 mL/min	CF. Flux 200 mL/min	CF. Flux 400 mL/min
5	44	105	70
15	128	188	153
30	226	323	344

Table 1. Average values of concentration factors, for the different times and fluxes used.

3. Experimental Set-Up

3.1. Measurement System

The Measurement system consists, in a set of 3 chambers for the different elements (see fig. 1). The Pre-Concentrator chamber, was mechanized in Teflon (Volume about 0,18 ml), that is interconnected to the commercial sensor chamber by a stainless steel tubing (l= 20 cm, ED= 6 mm, ID= 3 mm) that serve to cooling the carrier gas and decrease the impact of hot gas in the gas sensors responses [4].

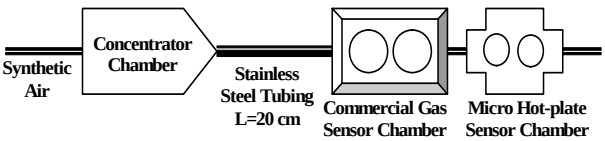

Fig 1. Gas Sensor measurement system.

The gas sensors chambers have different volumes; for the commercial sensors are 36 ml fabricated in acrylic glass and for the micro hot-plate (MHP) sensing array 0,50 ml fabricated in Teflon. These chambers are interconnected by a short length Teflon tubing.
Commercial TGS 822 gas sensor and noble metal-doped SnO_2 MHP gas sensor [5, 6] were selected to measure the benzene released from the preconcentrator.

3.2. Measurement Process

The measurement process is as follows: On one side, for the benzene absorption, a fixed flux of 200 ml/min is circulated through the concentrator chamber. The concentration employed of C_6H_6 was 150 ppb extracted from a calibrated bottle with CO_2 as gas carrier. On the other hand, in order to release the benzene from the pre-concentrator, the pre-concentrator and sensors chambers are inter-connected and 100 ml/min of synthetic air is circulated through them as carrier gas. Finally, the pre-concentrator is heated during 45 s at 250 ºC. To know the effect of temperature in the sensors, the pre-concentrator is heated in the same conditions of desorption without any absorbed substance.

4. Results

Figure 2 shows the response of a commercial sensor (TGS 822) at 3 different absorption times and the thermal effect in the sensor.

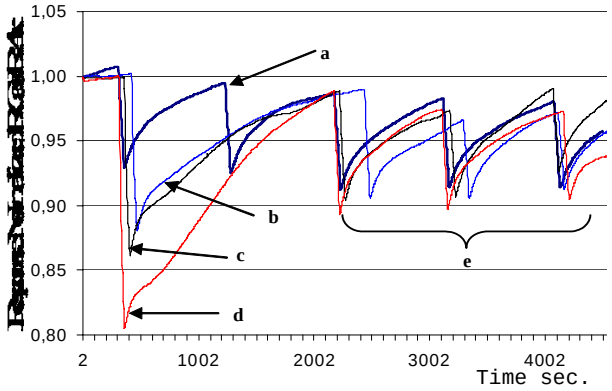

Fig.2. Normalized sensor response to: a) Heating Pre-Concentrator in Synthetic air, b) response after 5 min of absorption, c) response after 15 min of absorption, d) response after 30 min of absorption, e) thermal effect of desorption.

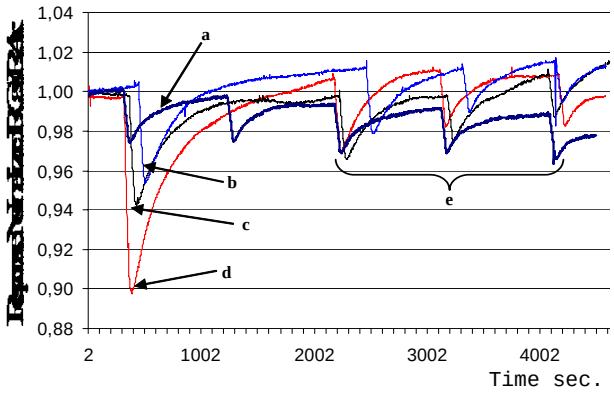

Fig. 3. Normalized sensor response to: a) Heating Pre-Concentrator in Synthetic air, b) response after 5 min of absorption, c) response after 15 min of absorption, d) response after 30 min of absorption, e) thermal effect of desorption.

The figure 3, show the micro hot-plate sensor (SnO_2+Pt) responses at 3 different absorption times.

In the above presented figures can be observed the difference between the peaks obtained as a result of the thermal response in synthetic air and in the case of benzene desorption. It could be clearly seen that the benzene compounds are released.

From these figures it can be seen that the recovery in commercial sensors is very slow compared to MHP sensor. In the later case the peak magnitudes are better defined.

Furthermore for both types of gas sensors, the 3 subsequent desorption show peaks labelled by *e* in figure 2 and 3, that the benzene is completely released. The shapes of the peaks are similar to the peaks in synthetic air.

5. Conclusions

The results obtained with the pre-concentrator_ show that is possible to increase the response of sensors for very low concentrations.
The principal limitation using this method is the thermal effect.

References

[1] Alexander C. Capleton, Leonard S. Levy "An Overview of occupational benzene exposures and occupational exposure limits in Europe and North America", Chemico-Biological Interactions 153-154 (2005) 43-53.

[2] V. Fierro et al, "Kraft lignin as a precursorfor microporous activated carbons prepared by impregnation with ortho-phosphoric acid: Synthesis and Textural characterization", Microporous and Mesoporous Materials 92 (2006) 243-250.

[3] F. Blanco et al, Miniaturized benzene preconcentrator for air quality monitoring, XX International Conference Eurosensors Proceeding (2006), Vol II, 326-327.

[4] Ljiubov Morris, Daren J Caruana and David E Williams, "Simple system for part-per-billion-level volatile organic compound analysis in groundwater and urban air", Meas.Sci. Technol. 13 (2002) 603-612.

[5] Figaro Gas Sensors, TGS 822 Data Sheet.

[6] P. Ivanov et al, "Influence of the doping material on the benzene detection", International Conference on Advanced Semiconductor Devices and Microsystems, 2006.

New TiO_2 and carbon nanotube hybrid microsensors for detecting traces of O_2 in beverage grade CO_2

E.H. Espinosa[1], L. Radouane[1], E. Sotter[1], R. Ionescu[1], C. Bittencourt[2], A. Felten[2], J.-J. Pireaux[2] and E.Llobet[1]

[1]Microsystems and Nanotechnologies for Chemical Analysis (MiNoS) University Rovira i Virgili, Tarragona, SPAIN
[2] Laboratoire Interdisciplinaire de Spectroscopie Electronique (LISE) University of Namur, BELGIUM

Abstract

We report on the development, fabrication and testing of an oxygen microsensor conceived for detecting traces of oxygen in beverage grade carbon dioxide. The microsensor is based on a titanium oxide and carbon nanotube hybrid gas sensitive layer obtained by a modified sol-gel process. The hybrid films show a high responsiveness towards traces of oxygen (~ 6) when operated at moderate temperatures (350ºC). This sensitivity compares very favourably to the one shown by similar microsensors based on titanium oxide with no carbon nanotubes.

1. Introduction

Considering the increasing social concern about quality and safety of foodstuffs, in the last years we have been working in the development of a multisensor system for monitoring the quality of carbon dioxide in the beverage industry [1]. The system employs metal oxide resistive gas sensors to successfully determine the presence of trace-level pollutants (methane, ethylene, sulfur dioxide and their mixtures) in a carbon dioxide stream [2]. Since oxygen is a pollutant species in beverage grade CO_2, there is a need for developing an oxygen sensor to be used within the multisensor system. Hybrid SnO_2 or WO_3 and carbon nanotube materials have been shown to possess high sensitivity to some air pollutant species at low operating temperatures [3]. In this context, this work reports for the first time on the development of an oxygen microsensor based on a TiO_2 and carbon nanotube hybrid film. The microsensor meets the requirements needed for assessing the quality of a CO_2 stream. To our knowledge, this is the first time metal oxide and carbon nanotube hybrids are introduced as sensitive material for detecting traces of oxygen. In addition, these hybrids are obtained via a new route: a modified sol-gel process. In the following sections, details on sensor fabrication and characterization are given.

2. Sensor fabrication

Two types of active materials were prepared using a sol-gel procedure. The first type consisted of either pure or niobium-doped titanium oxide and the second type consisted of pure or Nb-doped titanium oxide with carbon nanotubes. The standard sol-gel process was adapted for this purpose. During the hydrolysis phase of the usual sol-gel preparation of TiO_2, a small quantity of hydrogen plasma-functionalized multi-wall carbon nanotubes (MWCNT) was introduced. The same procedure was also followed for obtaining Nb-doped TiO_2/MWCNT hybrids. After the nucleation process, the obtained hybrid materials presented a proportion of ~ 1/500 wt% MWCNT/TiO_2. The materials were finally annealed at different temperatures ranging from 500 to 800ºC. The reason why nanotubes undergo a functionalisation in hydrogen r.f. plasma is twofold. On the one hand this treatment promotes the dispersion of nanotubes on the TiO_2 matrix and additionally, it cleans the nanotube surface and creates defects, which results in more reactive nanotubes [4-6]. Once annealed, the resulting powders were mixed with an organic vehicle based on glycerol and then drop-coated onto alumina based sensors substrates using a micro-injector. More details on the sensor chip can be found elsewhere [7]. Finally, an on-chip annealing using the polysilicon heating element within each membrane of the microsensor was performed to eliminate solvents. Figure 1 shows an image of a finished device.

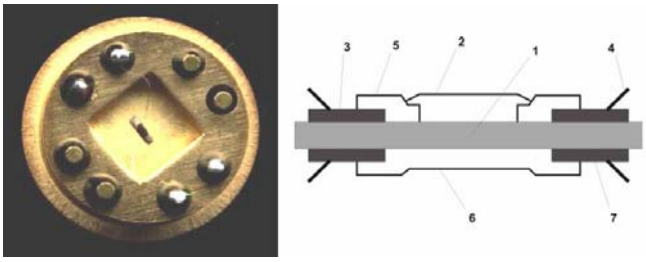

Fig. 1. Picture of sensor sustrate. 1. Alumina substrate, 2. sensing layer, 3. contact pads, 4. connecting wires, 5. disjunction layer, 6. heater, 7. contact pads

3. Sensor characterisation

In the first step, the morphology and crystalline phase of the different films obtained were studied.

The morphology of the films, recorded by ESEM analysis, indicated only the presence of titania grains at the surface of the films. However, images obtained from transversal sections of these films revealed the presence of nanotubes in the titania matrix (see Fig. 2).

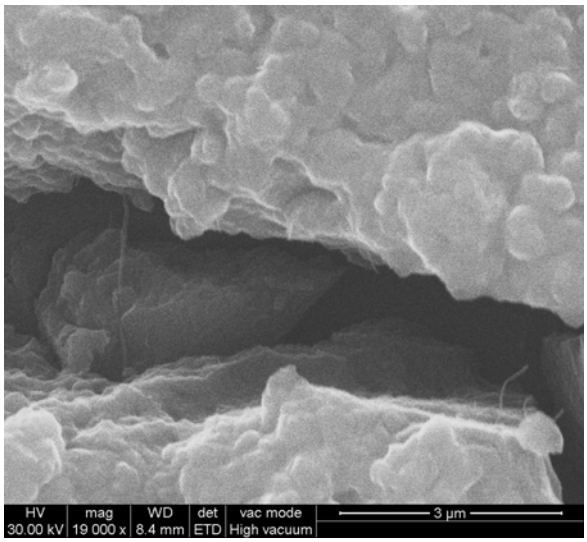

Fig. 2. ESEM image recorded for a TiO_2/MWCNT film sintered at 800ºC where some carbon nanotubes are visible.

XRD analyses were subsequently performed in order to determine the phase of TiO_2 in the hybrid films as a function of their annealing temperature. These results are shown in Fig. 3. The spectra recorded for TiO_2 films and MWCNT /TiO_2 hybrid films were similar. In conclusion, the presence of MWCNT did not modify the crystalline phase of TiO_2, but modified the microstructure of the films.

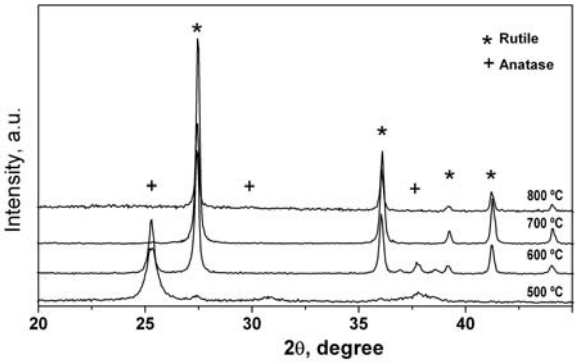

Fig. 3. XRD analysis of TiO_2/MWCNT hybrid materials sintered at different temperatures.

Figure 3 shows that anatase is the dominant crystalline phase in the materials sintered at the lowest temperature employed (i.e. 500ºC). A coexistence of rutile and anatase crystallites occurs for those materials annealed at 600ºC. Finally, rutile is the dominant phase for materials annealed at 700ºC or higher. Some authors have shown that anatase would be a more advantageous phase than rutile if one wants titanium oxide to behave as a surface-conductivity material (i.e. sensitive to oxygen at lower operating temperatures) [8-[9]].

In the second step, the gas sensing characteristics of the fabricated hybrid materials were investigated upon exposure to trace levels of O_2 in a CO_2 flow (concentration of 11 ppm). This was done by employing calibrated gas bottles and a computer-driven measurement rig and several mass-flow controllers. The best responsiveness to O_2 was obtained by TiO_2 / MWCNT samples operated at 350ºC (see Fig. 4). This responsiveness is approximately 20 times higher than the best responsiveness of pure TiO_2 films (operated at 500ºC) and approximately 6 times higher than the best of Nb-doped TiO_2 films (also operated at 500ºC). Furthermore, we also gained in lowering the optimal operating temperature for detecting oxygen. The response of Nb-doped TiO_2/MWCNT hybrid materials to O_2 (see Fig. 5) was lower, but more than doubled the response of Nb-doped TiO_2 films.

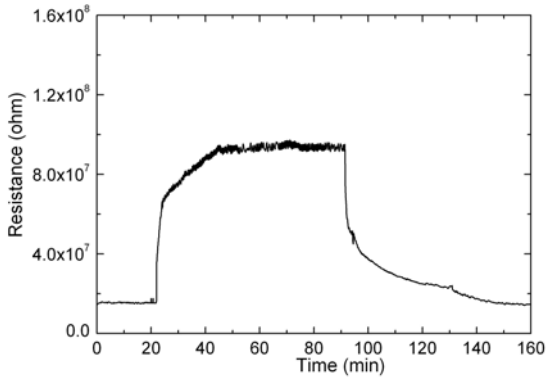

Fig. 4. Response to 11 ppm of O_2 in CO_2 flow obtained by TiO_2/MWCNT sensor sintered at 800 ºC operating at 350ºC.

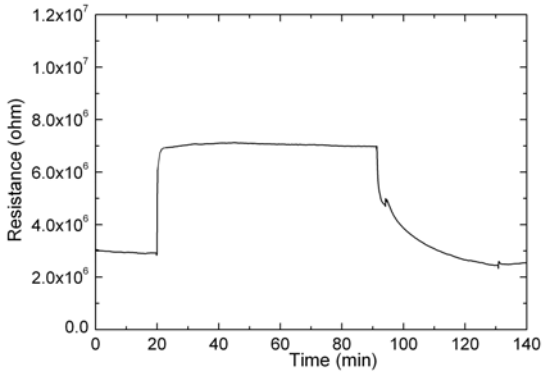

Fig. 5. Response to 11 ppm of O_2 in CO_2 flow obtained by Nb-doped TiO_2/MWCNT sensor sintered at 500 ºC operating at 350ºC.

The responsiveness towards oxygen was investigated for different operating temperatures. Table 1 shows a summary of the responsiveness study for the best sensors fabricated. Sensor responsiveness was defined by equation 1.

$$R = [R(O_2) - R(CO_2)]/R(CO_2) \quad (1)$$

where $R(O_2)$ is sensor resistance in the presence of 11 ppm O_2 and $R(CO_2)$ is sensor resistance in pure carbon dioxide.

Active Layer	OT(ºC)	R
TiO_2+CNT (500ºC)*	350	5.9
TiO_2+CNT (600ºC)	350	6.5
TiO_2+CNT (500ºC)	450	1.7
TiO_2+CNT (600ºC)	450	1.6
TiO_2 (600ºC)	500	0.3

Table 1. Summary of the responsiveness towards oxygen for the best sensors. (OT is operating temperature and R is responsiveness).
*Corresponds to the annealing temperature

These hybrid titanium oxide and MWCNT films were insensitive to methane and ethylene, so they show good potential as selective oxygen sensors. The presence of MWCNTs within the titanium oxide matrix alters the morphology (e.g. porosity) of the gas-sensitive layer and this surely has an important effect on sensor response.

4. Conclusions

A new material aimed at detecting oxygen at trace levels in a flow of CO_2 is introduced. An adapted sol-gel route that allows for controlling grain size and results in a good dispersion of nanotubes within the titania matrix has been developed. The fabricated microsensors show high sensitivity towards oxygen, reversible response in CO_2, good stability and fast response.

References

[1] X. Vilanova, X. Correig, E. Llobet, J. Brezmes, R. Calavia, X. Sanchez, “Carrier gas analyzer detecting reducing and oxidizing gases includes metal oxide based sensors with graphical representation of the measurements”, World Patent WO2004061449-A1, 2004.

[2] X. Vilanova, E. Llobet, J. Brezmes, R. Calavia, X. Sanchez, X. Correig, “A multisensor system for monitoring the quality of carbon dioxide in the beverage industry”, Transducers’03 Digest of Technical Papers, Vol. 2, 1347-50, 2003.

[3] E. Espinosa, R. Ionescu, B. Chambon, G. Bedis, E. Sotter, C. Bittencourt, A. Felten, J-J. Pireaux, X. Correig and E. Llobet, “Low temperature gas detection with hybrid metal oxides/MWCNTs”, Proceedings of Eurosensors XX, Gothenburg, 2006.

[4] R. Ionescu, E.H. Espinosa, E. Sotter, E. Llobet, X. Vilanova, X. Correig, A. Felten, C. Bittencourt, G. Van Lier, J.-C. Charlier and J.J. Pireaux, “Oxygen functionalisation of MWNT and their use as gas sensitive thick-film layers”, Sensors and Actuators B, Vol. 113, pp. 36-46, 2006.

[5] C. Bittencourt , A. Felten, E.H. Espinosa, R. Ionescu, E. Llobet, X. Correig y J-J.Pireaux, “WO_3 films modified with functionalised multi-wall carbon nanotubes: Morphological, compositional and gas responsiveness studies”, Sensors and Actuators B, Vol. 115, 33-41, 2006.

[6] C. Bittencourt, A. Felten, E.H. Espinosa, R. Ionescu, N. Moreau, P. Heszler, C.G. Granqvist, J.J. Pireaux, E. Llobet, “Evaporation of WO_3 on carbon nanotube films: a new hybrid film”, Smart Materials and Structures, Vol. 15, 1555-1560, 2006.

[7] J.H. Kim, J.S. Sung, Y.M. Son, A.A. Vasiliev, V.V. Malyshev, E.A. Koltypin, A.V. Eryshkin, D.Y. Godovski, A.V. Pisyakov and S.S. Yakimov, "Propane/Butane Semiconductor Gas Sensor with Low Power Consumption", Sensors and Actuators B, Vol. 44, 452–457, 1997.

[8] Y. Xu, X. Zhou and O. T. Sorensen, "Oxygen Sensors Based on Semiconducting Metal Oxides: an Overview", Sensors and Actuators B, Vol. 65, 2-4, 2000.

[9] K. Zakrzewska, "Gas Sensing Mechanism of TiO_2-Based Thin Films", Vacuum, Vol. 74, 335-338, 2004.

Ordered arrays of polymer microfibers by using macroporous silicon as template

R. Palacios, P. Formentín, T. Trifonov, J. Ferré-Borrull, J. Pallarés, A. Rodríguez, R. Alcubilla and L. F. Marsal

NePhoS (Nano-electronic and Photonic Systems), Departament d'Enginyeria Electrònica, University Rovira i Virgili, Av. Països Catalans 26, 43007 Tarragona, Spain
Departament d'Enginyeria Electrònica, Universitat Politècnica de Catalunya, Edifici C4, Campus Nord,c/ Jordi Girona 1-3, 08034 Barcelona, Spain
lluis.marsal@urv.cat

Abstract

The fabrication of one-dimensional nanostructures and microstructures inside the pores of porous template is intensively investigate. Herein we report the preparation of ordered macrofiber arrays from poly(methylmethac rylate) (PMMA) which is a hard and transparent acrylic polymer. We employed macroporous silicon with a pore diameter of 1.8-2 μm and various pore depth values as a template system.

1. Introduction

In recent years, the fabrication of nanostructures and microstructures based on porous templates has been intensively investigated [1,2]. The deposition of specific materials into porous templates allows tailoring structures as inverse replicas of the porous. The use of ordered porous arranged in a regular lattice allows fabrication of ordered fiber arrays.

Macroporous silicon is an attractive candidate for use as a template because the porosity and average pore size can be tuned by adjusting the electrochemical preparation conditions that allow the construction of photonic crystals, dielectric mirrors, microcavities, and other optical structures.

For many applications, porous silicon is limited by its chemical and mechanical stability but these issues can be eliminate using macroporous silicon as a template which provides the means for construction of complex optical structures from flexible materials that are compatible with biological systems or harsh environments [3].

In this context, we have used a simple technique for the fabrication of polymer microfibers with a monodispersive size distribution and uniform orientation using ordered macroporous silicon templates.

2. Experimental

Macroporous silicon was prepared by light-assisted electrochemical etching [4]. The starting material was n-type silicon with a resistivity of 2–6 Ωcm. The front side of the wafers was patterned with inverted pyramid shaped pits by oxidation, photolithography, and subsequent tetramethyl ammonium hydroxide (TMAH) etching. These inverted pyramids act as nucleation sites for the ordered pore growth. The wafers were incorporated in an electrochemical etching cell containing a 2.5 wt% aqueous solution of HF acid. The quality and size of the pores was controlled by a computerized feedback mechanism to maintain a constant current.

Samples with a pore depth between 22.1 and 7.48 μm and pore diameter value of 1.8-2 μm were fabricated. Furthermore, free-standing silicon templates was obtained when after pore growth, the back side of the wafer was etched until the holes opened. In this case macroporous silicon with 150 μm of pore depth and 3 μm of pore diameter was fabricated. As shown in Figure 1, the pores of the silicon templates were very uniform in size.

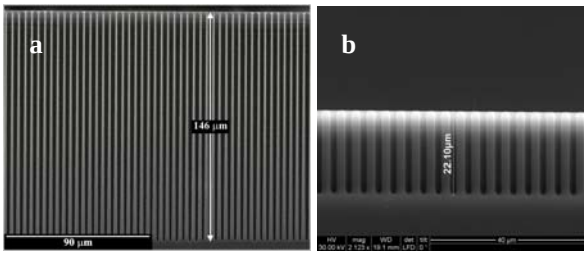

Fig.1. Scanning electron microscopy (SEM) images of cross section of (a) a membrane silicon template and (b) a macroporous silicon template.

Polymer microfibers using membrane macroporous silicon were prepared immersing the template in a

polymer solution of 27w% PMMA (poly(methylmethacrylate) purchase from Sigma-Aldrich) in toluene. The polymer solution was dropped to the template under vacuum when the silicon substrate was open only at one end. In this case, the concentration of the solution was lower (15w%) in order to improve the experimental results.

After immersion or addition of the solution, the samples were heated during 24h at 60ºC, followed of the immersion into 40w% KOH(aq) at 40ºC in order to remove the silicon template.

3. Results and discussion

Different types of macroporous silicon were used as template to obtain ordered arrays of polymer microfibers (see experimental part). Samples were examined by scanning electron microscopy (SEM) which allow us to confirm that the photonic structure of the porous silicon is retrained in the polymer casting.

Figure 2 shows the PMMA microfibers obtained from macroporous silicon template, which present about 150 μm. Microfibers of a length around 100-120 μm confirm that almost all the template was filled. These microfibers are not apparently solid.

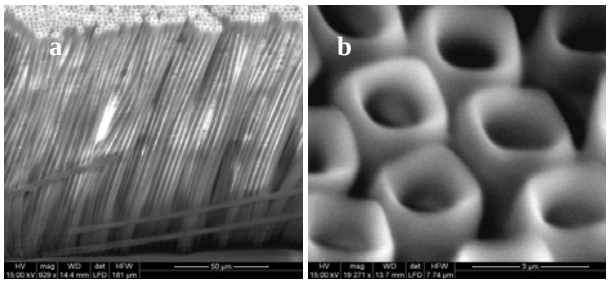

Fig.2. SEM images of PMMA microfibers after removed the macroporous silicon membrane. a) Cross-sectional view of some PMMA microfibers. b) Top view of the PMMA microfibers.

In order to control the microfibers length, macroporous silicon with different pore depth was used as template. These samples were prepared under vacuum but not all pore was filled. Using silicon templates with pore depth 22.1, 17.5 and 7.48 μm, microfibers of about 15, 12 and 4 μm respectively were obtained. These results are shown in Figures 3 and 4.

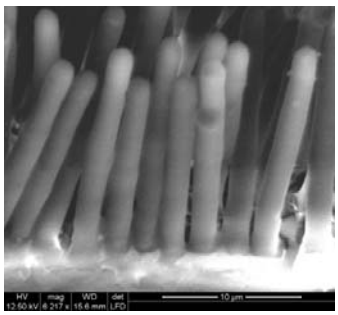

Fig.3. SEM images of PMMA microfibers after removed the template of 22.1 μm.

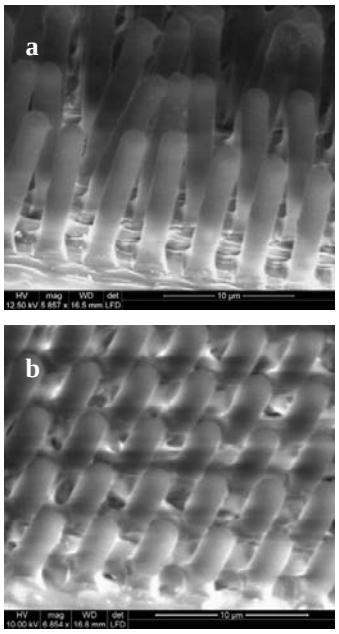

Fig.4. SEM images of PMMA microfibers after removed the template of (a) 17.5 μm and (b) 7.48 μm.

4. Conclusions

Ordered microfiber arrays were prepared using macroporous silicon as template. Two types of substrate were employed: macroporous silicon membrane and silicon substrate with only one end opened. The polymeric material selected was PMMA, which is a hard and transparent acrylic polymer.

Depending on the pore depth of the template, different microfibers with length between 4 and 15 μm were obtained. Notice that almost perfect ordered array was observed when length of the microfiber is less than 10 μm.

Acknowledgment

This work was supported by Spanish Ministry of Education and Science (MEC) under grant number TEC2006-06531. J Ferré-Borrull acknowledges the Ramón y Cajal fellowship from the Spanish Ministerio de Ciencia y Tecnología.

References

[1] X. Chen, M. Steinhart, C. Hess and U. Gösele, Advanced Materials, 18, 2153 (2006).

[2] M. Steinhart, J.H. Wendorff, A. Creiner, R.B. Wehrspohn, K. Nielsch, J. Schilling, J. Choi, U. Gösele, Science, 296, 20032 (1997).

[3] Y. Y. Li, F. Cunin, J. R. Link, T. Gao, R. E. Betts, S. H. Reiver, V. Chin, S. N. Bhatia, M. J. Sailor, Science, 299, 2045 (2003).

[4] T. Trifonov, L. F. Marsal, A. Rodríguez, J. Pallarès, R. Alcubilla, Physica Status Solidi (c), 2, 3104 (2005).

Enhancement of the sensitivity of gas sensors to toxic gases by using a novel hybrid material (Metal decorated MWNTs/Metal oxide)

R. Leghrib[1*], R. Ionescu[1], E.H. Espinosa[1], E. Sotter[1], A. Felten[2], C. Bittencourt[2], J.J. Pireaux[2], R. Erni[3], G. Vantendeloo[3] and E. Llobet[1]

[1] MINOS, Universitat Rovira i Virgili, ETSE-DEEEA, Av. Països Catalans 26, E-43007 Tarragona, Spain
Phone : 977 558 764 , Fax : + 34 977 559 605 , e-mail : radouane.leghrib@urv.cat
[2] LISE, Falcultés Universitaires Notre Dame de la Paix, 61 rue de Bruxelles, B-5000 Namur, Belgium
[3] EMAT, University of Antwerp, 171 Groenenborgerlaan, B-2020 Antwerp, Belgium

Abstract

Novel hybrid materials were fabricated by means of metal-decorated MWCNT dispersed on nanoparticular metal oxide. Active layers for gas sensing applications were obtained by adding a low amount of Au or Ag decorated MWCNT to two either SnO_2 or WO_3.
The hybrid materials have been analyzed by means of XPS, TEM and SEM. The sensing potential of the fabricated hybrid gas sensors has been tested upon exposure to different hazardous species, specifically NO_2, CO, C_6H_6 and NH_3, at low operating temperature.

Introduction

The carbon nanotubes (CNT) are receiving nowadays more and more attention from the gas sensors community[1-4]. Recently, hybrid films based on tin or tungsten oxide and carbon nanotubes have been introduced as new gas sensitive materials with improved sensitivity[1-3]. These works indicated that the detection at ambient temperature of toxic gases such as nitrogen dioxide, carbon monoxide and ammonia or ethanol vapors can be improved by dispersing an adequate quantity of carbon nanotubes into a metal oxide matrix.
In this paper, we study and discuss the performance in gas sensing of hybrid materials consisting of Au and Ag decorated multiwall carbon nanotubes dispersed in a metal oxide matrix.

Experimental

Sensing layers were prepared using commercially available SnO_2 and WO_3 nano-powders (Sigma-Aldrich). Hybrid materials were obtained by adding two different amounts of metal-decorated MWCNT to 70 mg of metal oxide (1/500 and 1/250 wt. %, respectively). An adequate mixture of the components was obtained by dissolving them in glycerol, and stirring the resulted solution in an ultrasonic bath at 75°C for 2 hours. The pastes obtained were dropped onto the electrode area of micro-hotplate transducers (fabricated at the Centre Nacional de Microelectrònica, Barcelona, Spain) using a micro-injector (JBE1113 Dispenser, I&J FISNAR Inc., USA).
The as deposited sensing films were firstly dried at 140 ºC during 2 h, using a slow temperature ramp of 2.5 ºC/min for reaching this temperature in order to avoid material's crashing. Finally, they were annealed in situ at 450 °C during 3 h in ambient atmosphere.

Results

Fig. 1 shows SEM images recorded on the different hybrid carbon nanotubes / metal oxide sensing films. The micrographs show the presence of the metal oxide grains, both when employing WO_3 and SnO_2. The presence of the carbon nanotubes was revealed only in the case of the WO_3/CNT hybrids, while they could not be actually detected into the SnO_2 matrix. This is due to the low proportion of the carbon nanotubes embedded in the metal oxide matrix (1/500 or 1/250 wt. %), and to the difference in density between WO_3 and SnO_2 (7.16 and 6.95 g/cm^3, respectively[3-5]). Taking into account furthermore the extremely low density of the CNT (0.7 g/cm), a very important difference between the number of SnO_2 grains and the number of carbon nanotubes added is predictable, which made very difficult to detect the presence of CNT by SEM analyses.

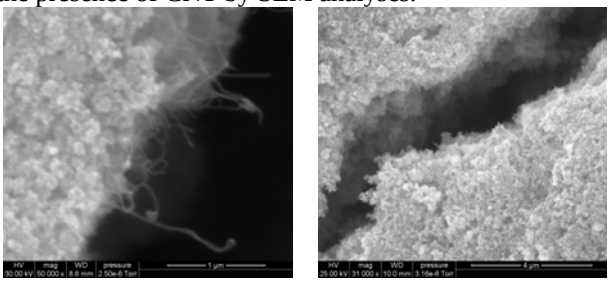

Fig.1: SEM images recorded on different hybrid films: (left) Ag-MWCNT/WO_3 (1/500 wt.%); (right) Ag-MWCNT/SnO_2 (1/250 wt.%).

Sensors based on SnO_2 and Au-decorated MWCNT were the most sensitive to NO_2, outperforming in a high degree the performance of either pure SnO_2 or pure Au-decorated MWCNT materials when operating both at

250ºC and 150ºC. Typical responses of metal-decorated MWCNT/ SnO_2 gas sensors to NO_2 are shown in Fig. 2. The quantity of nanotubes dispersed in the SnO_2 matrix was found to play a determinant role in the sensing mechanism of the hybrid materials to NO_2 detection. At 1/250 wt% ratio, the responsiveness of the hybrids made of metal-decorated MWCNT and SnO_2 was significantly superior in comparison with the 1/500 wt% ratio when the detection of NO_2 at 250ºC. When the operating temperature of sensors was lowered to 150ºC, the particular type of metal decorating the carbon nanotubes emphasized also an important role in NO_2 detection. Thus, at 150ºC a concentration ratio of 1/250 wt% of carbon nanotubes dispersed in the SnO_2 matrix was the most appropriate when Au was used as dopant, while 1/500 wt% of Ag-decorated MWCNT added to SnO_2 was the most suitable for this later case. On the other hand, similar values of responsiveness were found at 150ºC for both Au-MWCNT/SnO_2 and Ag-MWCNT/SnO_2 materials. Furthermore, it is worth mentioning that the hybrid films based on SnO_2 became already saturated after the injection of just only 500 ppb of NO_2 at the working temperature of 150ºC .

Regarding the responsiveness of the hybrid materials based on WO_3 to NO_2, when existing, it was at least one order of magnitude below the one obtained by the hybrids based on SnO_2. The quantity of nanotubes embedded in WO_3 was of important relevance. Thus, when the sensors were operated at 250ºC, only metal-decorated MWCNT dispersed in the WO_3 matrix in a concentration ratio of 1/500 wt% were able to detect NO_2, while at 150ºC the semiconducting behaviour of the metal-decorated MWCNT/WO_3 hybrids changed from n-type at a concentration ratio of 1/500 wt% (similar to WO_3 behaviour), to p-type at a concentration ratio of 1/250 wt% (similar to carbon nanotubes behaviour).

The second air pollutant tested was CO. The highest responsiveness was again achieved by the hybrid sensors based on Au-decorated MWCNT and SnO_2 in the concentration ratio of 1/250 wt%, operated at 250ºC . Although lower, some responsiveness was also obtained at 150ºC by the hybrid sensors containing SnO_2. When the metal oxide employed was WO_3, the only hybrid based on this material that responded to CO was Ag-MWCNT/WO_3 in the concentration ratio 1/500 wt% at the operating temperature of 250ºC. One surprising phenomena observed is, in spite of its very low responsiveness to CO, the particular behaviour of the Ag-MWCNT/WO_3 hybrid material (concentration ratio 1/250 wt%). When this sensor was operated at 250ºC, it behaved as an n-type semiconductor; operated at 150ºC it did not respond at all to CO; while at room temperature its behaviour was equivalent to an n-type semiconductor. This achievement clearly suggests that not only the amount of carbon nanotubes determines the semiconducting character of the new hybrid materials fabricated, but also that the operating temperature can play an important role in the sensing mechanism.

The sensors did not respond toNH_3 and C $_6H_6$.

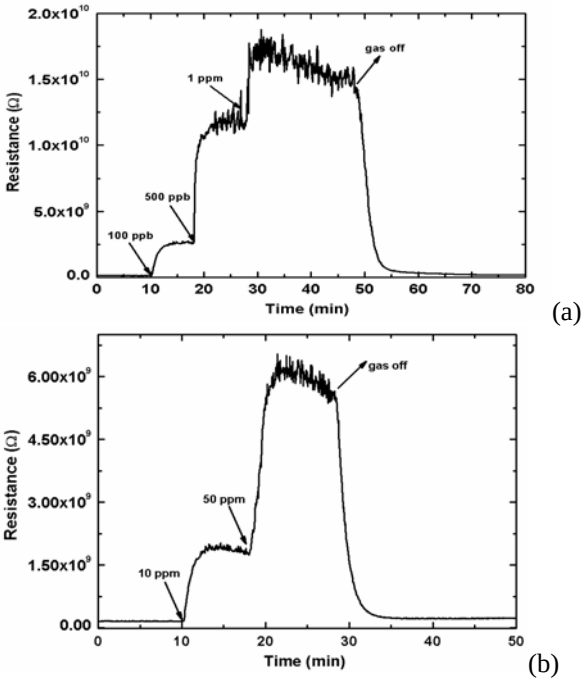

Fig.2: Response to different hazardous species obtained by gas sensors employing different hybrid materials: (a) NO_2 detection at 250ºC with Ag-MWCNT/SnO_2 (1/250 wt.%) sensor; (b) CO detection at 250ºC with Au-MWCNT/SnO_2 (1/250 wt.%).

Conclusions

The addition of a small quantity of metal decorated MWCNT to metal oxides can significantly improve the detection capability of metal oxide based sensors and lower the operating temperature.

In particular, micro-sensors based on Au-MWCNT/SnO_2 hybrid films in a concentration ratio of 1/250 wt% showed the highest sensitivity towards NO_2 and CO. The response mechanism is fully reversible, since the sensors can recover their baseline resistance after each exposure to pollutant gases.

Our results suggest that there is an optimum amount of carbon nanotubes to be added to each particular metal oxide in order to enhance responsiveness.

The modulation of the width of two depletion layers existing at the surface of metal oxide grains and at the interface of metal oxide grains and MWCNT, respectively is postulated as the mechanism that could explain the enhanced performance of hybrid metal oxide/MWCNT sensors in comparison with pure metal oxide or pure MWCNT sensors.

References

1. S. Chopra et al, APl, Phy, Lett, 83 (2003), 2280-2282.
2. C. Cantalini et al, Sensors and Actuators 95 (2003), 195-202.
3. J. Li et al ,Nano Lett, 3 (2003), pp. 929-933.
4. Y. Lu et al, Journal of Electroanalytical Chem, 593 (2006), 105-110.
5. http://www.mercorp.com.

Thermo-Electrical Characterization of a Silicon Micro-Hotplate Membrane of a Gas Pre-concentrator

H. Lahlou[1*], P. Ivanov[2], X. Vilanova[1], X. Correig[1]

[1] DEEEA, Universitat Rovira iVirgili , Spain
[2] Gas Sensors Group, Centre National de Microelectrònica, CNM-CSIC, Bellaterra, Spain
[*]Houda Lahlou, Departament d'Enginyeria Electrònica, Electrica i Automàtica, URV
Avinguda dels paisos Catalans, 26 Campus Sescelades, 43007 TARRAGONA (Spain)
Tel. +34 977 558 764, Fax +34 977 559 605 e-mail: houda.lahlou@urv.cat

Abstract

Environmental monitoring requires the measurement of gas pollutants present at trace concentrations. The key component in trace analysis is the pre-concentration step aimed to enhance the sensitivity and selectivity of metal-oxide gas sensors toward these gases. These concentrators are based on thermal programmed adsorption-desorption. So, they need a well designed membrane to carry and heat the adsorbing layer to the desired temperatures. Our new challenge is to fabricate a low power consumption silicon microsystem that can include the gas sensor and gas concentrator membranes over the same substrate. To achieve that goal, a micro-hotplate membrane for gas concentrator bigger than the conventional one used for gas sensor is primarily designed and thermo-electrically characterized. In this paper, we will evaluate its power consumption, thermal response and life time.

1. Introduction

Some volatile organic compounds like benzene, toluene and xylene have been identified as a human carcinogenic even at a concentration of some ppb [1].

Our group has already tested some microhotplate membranes based-metal oxide gas sensors (table 1) [2,3] designed and fabricated at CNM in Barcelona.

Membrane Dimensions	Power vs. temp.	Heating time (ms)	Cooling time (ms)
1000x1000x3.54 (μm^3)	8.11mW/ 200 ºC	12	4

Table1. Thermo-electrical characteristics of silicon Micro-hotplate membrane for gas sensors

These membranes were thermo-electrically characterized giving very good results. The new challenge of the group is to design a portable and low cost microsystem that can include the gas sensor and the concentrator over the same substrate. The idea is to design a silicon micro-hotplate membrane bigger than those for gas sensors to be used for the concentrator conventionally used. Through a thermo-electrical characterization of the structure, we will preview the power consumption, thermal response and life time needed for implementing the microsystem.

In this paper, the membrane will be adapted to gas concentrator. The gas concentrator must include an adsorbing layer over the membrane and a silicon micro-hotplate support containing a resistive heater to perform its thermal cycling.

The experiments performed are aimed to determine: The electrical parameters (voltage and current) needed for cycling thermally the membrane to 200 ºC, the thermal response time and the heating power consumption that needs the membranes to reach this temperature. Finally, the life time of the membrane under the application of continuous thermal cycling. The temperature range considered in this study is [To-200ºC], where To is the ambient temperature.

2. Design and fabrication

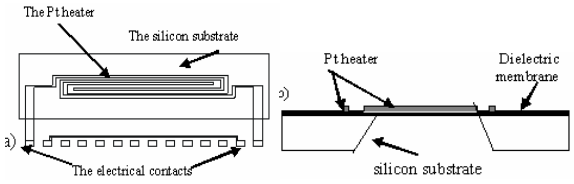

Fig 1. **a)** A view from the top of the membrane
b) A cross sectional view of the membrane

The membrane has a total size of 3000x1000 μm^2 (fig. 1.a and 1.b) and it's composed by:

-A mechanical support: Silicon substrate 300 µm thick anisotropically etched to reduce the heat losses.

-A dielectric block: Three layers of low thermal conductivity to ensure the thermal insulation of the structure (1.2 µm thick). They are fabricated as follows:

- Thermal oxidation at 1100 ºC in order to grow 100 Aº of a SiO_2 layer.
- An LPCVD deposition of 8000 Aº of SI_3N_4 layer.
- An LPCVD deposition of 3000Aº of SiO_2

-The heater: Platinum layer is deposited. It has a serpentine shape to ensure the uniformity of the temperature distribution under the adsorbing layer. The heater has a thickness of 2500 Aº and a length of 12350 µm. The heater separation is 50 µm and its width was estimated to be 50 and 80 µm in the middle and in the electrical contacts respectively. A layer of Ti is deposited prior to Pt to promote the heater adhesion to the substrate.

3. Thermo-electrical characterization

3.1. The temperature programming and evaluation of the heating power consumption

In this section, Three identical membranes are tested. An input voltage was applied by a Keithley power supply. It was controlled by a Labview program. A Matlab program was used to calculate the temperature reached by the membrane using eq (1) and to plot the graphs of temperature reached by the membrane 2 vs. time (fig. 2.a), voltage applied V, current I passing through the heater resistor and the heating power consumption P (fig. 2.b).

$$R_T = R_0*(1+\alpha*(T- To) \quad \text{eq (1)}$$

R_T is the Pt heater resistance at temperature T, R_0 is the resistance at an ambient temperature To, α=0.00392 Ω/Ω/ºC is the standard linear thermal coefficient of Pt.

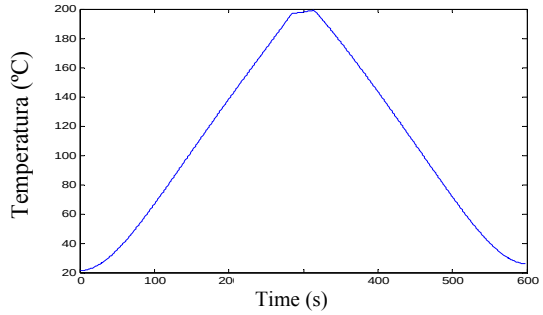

Fig 2. a) The temperature (ºC) of membrane 2 vs. time (s)

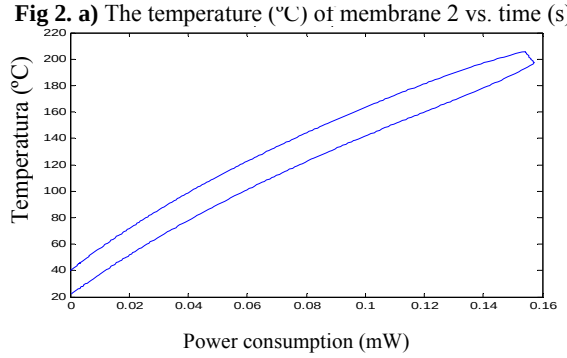

Fig 2. **b)** Temperature (ºC) of membrane 2 vs. power consumption (W)

The results obtained for the three membranes are summarized in table 2 bellow:

MHTP	To(ºC)	Ro(Ω)	T(ºC)	v(V)	I(A)	P(mW)
(1)	23.2	186,19	200,18	6	19.02	114.15
(2)	21.8	282,73	199,04	9.5	19.82	188.35
(3)	21.8	211,97	205,77	7.5	20.12	150.91

Table2. The electrical parameters adjusted in order to reach a temperature around 200 ºC

3.2. The thermal response time

The thermal response time of membrane 2 and 3 includes the time needed for heating the membrane from ambient temperature to 200 ºC and its cooling time.

The relation between the heater voltage U, current I and its temperature is described by the following eq. (1):

$$U= R_0*(1+\alpha*(T- To))*I \quad (1)$$

Where U is the heater voltage, I the current passing through the heater resistor.

The idea is to inject a sequence of current peaks (0.1 s period) limited by 4 and 20 mA by means of the Keithley source (20 µs of response time) then, collect and record the graph of the heater voltage versus time using an oscilloscope. So the membrane heating and cooling time will be respectively the same as the delay time for that the voltage reaches 90% of its maximal value and passes from this value to the minimal one. We have determined the time values (table 3) from the graphs obtained:

membrane	Heating time (ms)	Cooling time (ms)
(2)	9.44	14.5
(3)	10.88	12.4

Table3. Thermal response times of membranes 1 and 2.

3.3. The Membrane life time

- In order to count the number of cycles that can support membrane 1 without breaking down, a thermal cycling has been performed by applying a periodic square voltage signal. The number of cycles was calculated by means of a counter. The cycle period was at first adjusted to 70 s. It was reduced after to 34s and finally to 1s (table 4). Nowadays, the membrane is still surviving.

Cycle period (s)	The number of cycles applied
70	40328
34	8192
1	439 848….

Table4. Life time of membrane 1 during its thermal cycling

- A voltage of 6 V was applied to membrane 1. Then, it was increased by 1V step. By applying 16.5 V, the membrane reaches 480 ºC without breaking down. On the other hand, membrane 4 (Ro= 208 Ω at To= 22.3 ºC) broke down at 335 ºC by abruptly applying a voltage of 10 V.

4. Summary and conclusion

The concentrator membrane was able to reach rapidly (from 9.44 to 10.88 ms) the temperature of 200 ºC requiring only a power consumption ranging from 114 to 188 mW. It demonstrates its long life time under a thermal cycling process and its ability to be heated at up to 480 ºC without breaking down. This is due to the good thermal insulation of the membrane demonstrated by the experiments performed in the CNM.

Although this gas concentrator structure is bigger than the membrane previousely designed for gas sensor (see table 4), their thermal response are almost the same. This can be due to the new design of the heater (serpentine shape) for higher uniformity of the temperature distribution. These results encourage to implement the preconcentrator/ gas sensor microsystem.

References

[1] T. Sorahan et al, *Occup. Envir. Med.*, 62 (2005) 231.
[2] A. Vergara et al, *Eurosensors XVIII*, (2004) 13.
[3] C. Cané et al, *J. Micromech. Microeng* 7 (1997) 247.

Reflectance spectroscopy of photonic bands dispersion in macroporous silicon

Zdeněk Král* [1], Josep Ferré-Borrull[1], Lluis F. Marsal[1], Josep Pallarés[1], Trifon Trifonov[2], Angel Rodriguez[2], Ramon Alcubilla[2]

[1]Nephos, Universitat Rovira i Virgili, Campus Sescelades, Avda. Paisos Catalans 26, Tarragona 43007, Spain.

[2]MNT, Universitat Politécnica de Catalunya, Campus Nord, c/ Jordi Girona 1-3, 08034 Barcelona, Spain.
*Tel.: 977 55 86 53 - e-mail: zdenek.kral@urv.cat – http://www.urv.es

Abstract

We report an experimental study of two-dimensional (2D) macroporous silicon photonic crystals using an angular-dependent reflectance spectroscopy. We have investigated samples with different lattice structures and lattice constants. The macroporous silicon samples were measured along the different symmetry directions of the lattices so that the photonic bands can be mapped.

1. Introduction

The Photonic crystals are artificial materials with a spatial periodicity of their dielectric constant on a wavelength scale. This spatial periodicity implies the application of the Bloch-Floquet theorem to the Maxwell equations and thus, to the existence of photonic bands, which are analogous to the electron bands in crystalline solids.

Photonic crystals were first proposed by *Yablonovitch* [1] and *John* [2] as a way to suppress spontaneous emission and to localize light by disorder. They showed that by a proper design of the photonic crystal geometry and the material dielectric constant, the electromagnetic wave dispersion inside the structure can be tailored. To have control over the modeling of the structure, it became necessary to develop methods for the photonic crystal characterization.

Photonic crystals have first been characterized in the microwave regime by phase-sensitive transmission measurements [3] that yield the wave vector inside the crystal at a given frequency. Other technique, based on the in-plane transmission in two-dimensional (2D) waveguide photonic crystals has been used to map the photonic bands from Fabry-Pérot fringes within the sample [4]. Several authors have also measured the photonic bands dispersion in 2D photonic crystals by means of the angular-dependent reflectance spectroscopy, first proposed by Astratov at al. [5]. This method relies on the observation of resonant features in the reflectance spectra at different incidence angles. The resonant features occur when the in-plane component of the wave vector ($k_{//}$) of the incident light matches the wave vector of a propagating mode inside the photonic crystal. The in-plane wave vector $k_{//}$ is related to the angle of incidence on the photonic lattice θ and to the incident light frequency as $k_{//} = (\omega/c) \sin\theta$. By varying θ, and monitoring the wavelengths λ of the resonant features in the reflectivity spectra, the photonic bands dispersion can be extracted.

In this paper we report the optical characterization of different 2D macroporous silicon structures. The paper is organized as follows. In Sec. II we present the fabrication of macroporous silicon samples by photo-electrochemical etching process. In Sec. III we describe the setup for experimental measurements by angular-dependent reflectance technique. Finally, the results are summarized in section IV.

2. Samples fabrication

The macroporous silicon photonic crystals of different lattice types were prepared by a photo-electrochemical etching process. An n-type (100) silicon wafer with a resistivity of 2-6 Ωcm was first pre-structured by oxidation, photolithography and subsequent tetramethyl ammonium hydroxide (TMAH) etching to form the initial pits. Such a patterned structure consists of ordered pyramidal notches that act as nucleation centers for the following ordered pore growth. The pore growth mechanism is ruled by the reverse-biased space charge region at the silicon-electrolyte interface. In order to create a good ohmic contact at the silicon-electrolyte interface, a uniform n^+-layer was created on the wafer backside by ion implantation. The electrochemical etching was carried out in aqueous hydrofluoric acid (HF) with a concentration of 5wt. % at 15°C. During the anodization, the wafer was backside illuminated by a 100 W halogen lamp, coupled to an IR cut-off filter. More detailed information about the sample fabrication and sample structures used in this paper can be found elsewhere [6].

3. Experimental measurements

All the studied samples have lattice constants that range between 4 μm and 5 μm. Standard plane-wave expansion band calculations show that, for these lattice constants, the first photonic bands lie in the mid-infrared range. For this reason, the angular-dependent reflectivity was measured in the mid infra-red region (4000-400 cm-1) using a Fourier-transform Infra-Red

spectrometer (Bruker, model Vertex 70) equipped with a special reflectivity attachment. The light source was a broadband halogen-tungsten lamp. The angle of incidence θ was varied from 12º to 66º in steps of 2°, and the plane of incidence was perpendicular to the sample surface. The reflectivity spectra were recorded with a liquid-nitrogen-cooled MCT detector. The spectral resolution was set to 4 cm-1. A polished N-type silicon wafer was used as absolute reflectance reference. The measurements were performed for light incident along the ΓX and ΓM lattice orientations for the square lattice structure, and along the ΓM and ΓZ directions for the triangular and honeycomb lattices.

4. Results

Figures 1, 2, 3 and 4 show the photonic bands dispersion corresponding to the macroporous silicon structures shown in the insets. The figures represent 2D plots of the angular-dependent reflectivity versus the photon energy and the angle of incidence. The lattice type, the lattice dimension and the lattice orientation of the measurement are included in the insets respectively. Each 2D plot is overlapped with the theoretically calculated photonic bands. The dot-and-dashed lines and full lines corresponding to TM and TE light polarization respectively.

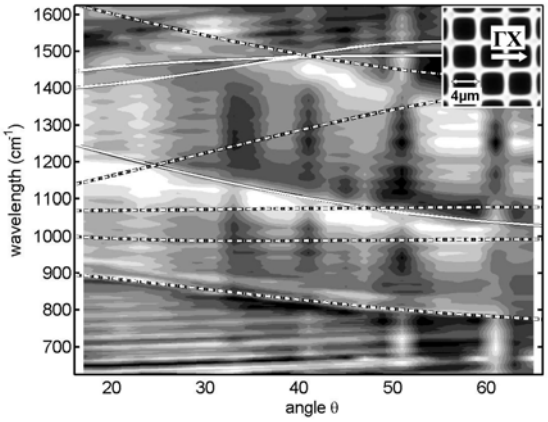

Fig.1. The photonic bands dispersion corresponding to the sample consisting of rounded square air holes formed in a square lattice.

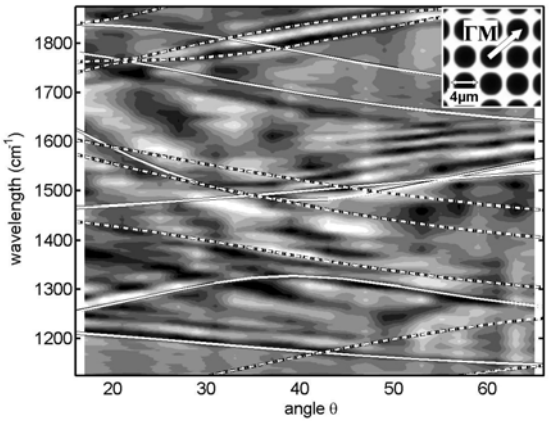

Fig.2. The photonic bands dispersion corresponding to the sample consisting of air holes formed in a square lattice.

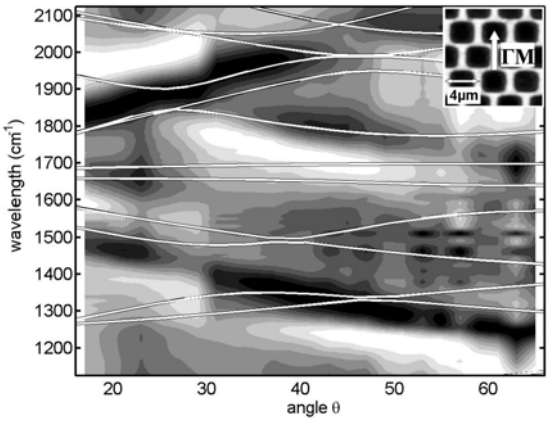

Fig.3. The photonic bands dispersion corresponding to the sample consisting of rounded square air holes formed in a triangular lattice.

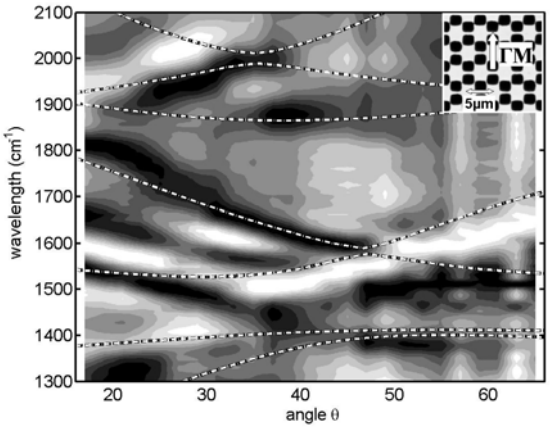

Fig.4. The photonic bands dispersion corresponding to the sample consisting of rounded square air holes formed in a honeycomb lattice.

5. Conclusions

We have applied the angular-dependent reflectivity technique to the characterization of macroporous silicon photonic crystals. We have distinguished several photonic bands in macroporous structures of different lattice types and lattice constants. The characteristics of the samples require that the measurement range is in the mid-IR, which implies the adaptation of the technique.

References

[1] E. Yablonovitch, Phys. Rev. Lett. **58** (1987), pp. 2059-2062.

[2] S. John, Phys. Rev. Lett. **58** (1987), pp. 2486-2489.

[3] E. Yablonovitch, T. J. Gmitter, Phys. Rev. Lett. **63** (1989), pp. 1950-1953.

[4] D. Labilloy, H. Benisty, C. Weisbuch, T. F. Krauss, R. M. DeLaRue, V. Bardinal, R. Houdre, U. Oesterle, D. Cassagne, C. Jouanin, Phys. Rev. Lett. **79** (1997), pp. 4147-4150.

[5] V. N. Astratov, M. S. Skolnick, S. Brand, T. F. Krauss, O. Z. Karimov, R. M. Stevenson, D. M. Whittaker, I. Culshaw, R. M. De la Rue, IEE P-Optoelectron. **145** (1998), pp. 398-402.

[6] T. Trifonov, L. F. Marsal, A. Rodriguez, J. Pallares, R. Alcubilla, Phys. Stat. Sol. **8** (2005), pp. 3104-3107.

Thinning barrier layer of self-ordered porous alumina templates for nanostructure synthesis

A. Santos, L. Vojkuvka, J. Ferré-Borrull, J. Pallarés and L. F. Marsal*

Rovira i Virgili University, ETSE-DEEEA,Av. Països Catalans 26, 43007 Tarragona - Spain

*Tel.: +34 977 55 96 25 - e-mail:lluis.marsal@urv.cat

Abstract

A method to reduce or eliminate the oxide barrier layer from the pore bottoms of self-ordered porous alumina was probed. The samples were characterized using several techniques such as environment scanning electron microscopy (ESEM) and atomic force microscopy (AFM). Afterwards, data were suitability treated and later analyses were done. Characteristics of home-made PAMs were accurately determined by means of fast Fourier transforms (FFT). In this way, we were able to establish the thinning rate of the oxide barrier layer, the arrangement of pores, the interpore distance and the pore length and diameter. In addition, our results were compared with previous works and new applications were proposed.

1. Introduction

Scientists have made a lot of efforts in order to improve the fabrication process of porous alumina membranes (PAMs) for a long time [1]. Since the two-step anodization process was used for the first time [2], many research groups have studied this process and new ways to produce PAMs have been come out [3]. With regards to the two-step process, we can to produce PAMs with desirable dimensions varying the work parameters (acid, applied voltage, temperature, anodizing time, etc.). Previous studies have established the relationship between PAMs properties and the work parameters [4, 5, 9]. This fact has allowed to us produce PAMs controlling relatively their morphology. Therefore, we can adapt home-made PAMs to later applications. One of these applications is to use PAMs as etching mask on certain substrates. The porous alumina structure consist of pores which have the upper part opened but its bottom is covered by a thin oxide barrier layer of several tens of nanometers. The thickness of this layer depends on the applied voltage throughout the anodization process (approximately 1.3 nm/V). If this barrier layer is eliminated, PAMs can be used as pattern to transfer certain nanostructures on other kind of substrates such as aluminum, silicon, titanium, etc. In this study we report a way to reduce or eliminate the oxide barrier layer of pore tips introducing a new stage when the 2nd anodization has finished. Meanwhile the PAM stand attached to aluminum substrate, the wet chemical pore widening is carried out following the standard procedure. Then, two current-limited anodization steps are applied and due to the anodization take place under non-equilibrium conditions the oxide barrier layer decreases its thickness progressively [6, 7].

2. Experimental part

The substrates (High purity aluminum (99.999%) foils from Goodfellow Cambridge Ltd.), which were later used to produce home-made PAMs by two-step anodization process, were firstly pre-treated. The foils were annealed in nitrogen (N_2) environment at 400ºC for 3 hours. Afterwards, they were electropolished in a mixture of EtOH and $HClO_4$ 4:1 (v:v). Once the samples were washed with distilled water and dried, a two-step anodization was performed on the aluminum surface using oxalic acid (0.3M). Both first and second step were carried out using a potenciostatic regime with different potentials depending on the used acid. When the first anodization was finished, a film of alumina with disordered pores was obtained. Then, this film was removed from the aluminum substrate by wet chemical etching in a mixture of phosphoric acid (0.4M) and chromic acid (0.2M) at 70ºC during the same time of first step (about 30 minutes). In this way, we produced a pre-pattern on aluminum surface. Subsequently, the second step consisted in repeating the conditions used in the first step but varying the etching time to obtain a thicker film (approximately 8μm/h). The PAM with ordered pores resulted from the second step. After the anodization process was finished, a standard chemical pore widening was applied immersing the samples in an aqueous solution of phosphoric acid (5%wt) for 10 minutes at room temperature. Later, the removing of the barrier layer was carried out using two current-limited anodization steps. The first one was carried out at 0.50mA/cm² and the second one at 0.25mA/cm², both for 3 minutes. As Fig. 1c shows, when the second step is finished, the voltage profile tends towards certain value asymptotically. At this moment, the oxide barrier layer has been completely removed from pore bottom tips. At last, to separate the PAM for later characterization, the aluminum substrate was dissolved immersing the samples in a solution of HCl and $CuCl_2$ at 25ºC for 10 minutes approximately.

The different stages of our process were controlled by computer-controlled analogic interface using the LabView 6.1 ™ software.

3. Results and discussions

The morphology of the PAMs was examined by ESEM and AFM. In Fig. 1a-b we can see ESEM images, in which ordered arrays of nanopores arranged hexagonally are noticeable on the sample bottom surface. Comparing Fig. 1a and Fig. 1b images, we can see clearly that the oxide barrier was removed as a whole. This fact spreads use of porous alumina for a large quantity of future applications. By means of this technique, we obtain a high-ordered mask to etch a lot of materials and, in this way, to transfer its arrangement to them. In addition, their diameter was 15 and 40 nm with interpore distance of 50 and 120 nm for sulfuric acid and oxalic acid, respectively.

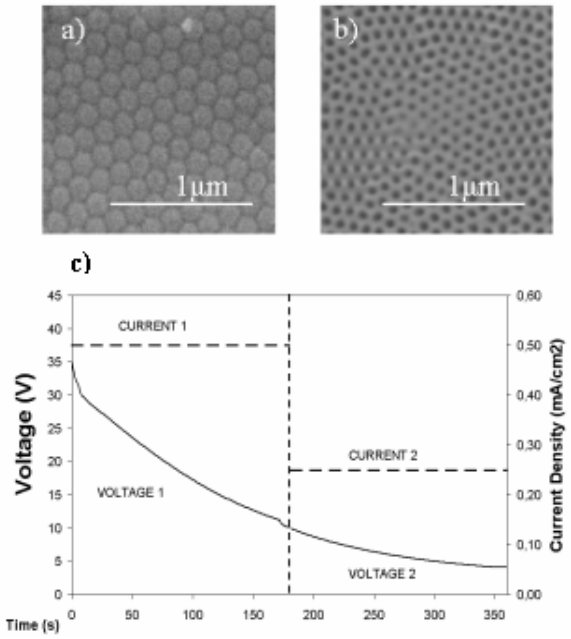

Fig. 1: ESEM images of ordered porous alumina membrane (PAM). a) Bottom image of PA in oxalic acid before the removing of the oxide barrier layer. b) Bottom image of PA in oxalic acid after the removing of the oxide barrier layer. c) Voltage and Current Density profiles used in the removing of the oxide barrier layer.

Fast Fourier transform (FFT) analysis was carried out for AFM high-resolution micrographs of PAMs produced by two-step anodization in oxalic acid. FFT of the AFM image representing the pore pattern over the sample surface provides the information about the geometrical periodicity in the reciprocal space. In theory, the ideal model for a pore array with a perfectly ordered triangular lattice has a FFT pattern consisting of a reciprocal hexagonal array. The Fig. 2a represents the AFM top surface image of PAM. In Fig. 2b we can see magnified zone, where the inset represents FFT. In order to perform the FFT analysis, the source image was first processed using specific software [8]. The FFT domain consists of various hexagons revealing the fact that the source image is highly ordered. Moreover, this figure illustrates six very bright spots arranged into the circle. This confirms quite perfect six-fold ordering of pores over the surface, while the ring shape predicts some periodicity imperfection in the ideal hexagon.

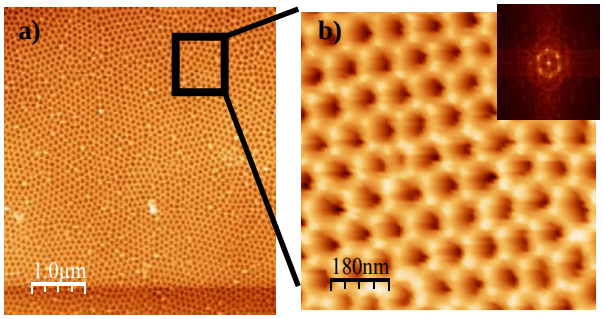

Fig. 2: a) High-resolution AFM top surface micrographs of PAM produced in oxalic acid and b) zoomed part where the inset represents Fast Fourier Transformation (FFT)

4. Conclusions

Ordered porous alumina membranes (PAMs) were fabricated by two-step anodization process. A method to remove the oxide barrier layer from their bottom tips was used. It could be a new way in order to use self-ordered porous alumina templates for nanostructures synthesis such as wires, tubes, dots, holes and pillars. Finally, ESEM and AFM were used in this study to characterize each sample, obtaining its morphology (diameter, interpore distance, thickness and arrangement) after analyse the data and images.

Acknowledgements

This work was supported by the Spanish Commission of Science and Technology (MEC) under grant number TEC2006-02038. J. Ferré acknowledges the Ramón y Cajal fellowship from the Spanish Ministerio de Ciencia y Tecnología.

References

[1] F. Keller, M. S. Hunter and D. L. Robinson, J. Electrochem. Soc., 100 (1953) 411

[2] H. Masuda, K. Fukuda, *Science*, 268 (1995) 1466

[3] K. Nielsch, R. B. Wehrspohn, J. Barthel, J. Kirschner, U. Gösele, S. F. Fischer, and H. Kronmüller, *Appl. Phys. Lett.*, 79 (2001) 1360-1362

[4] G . Che, B. B. Lakshmi, E. R. Fisher, C. R. Martin, *Nature*, 393 (1998) 346

[5] Y. Du, W. L. Cai, C. M. Mo, J. Chen, L D. Zhang and X. G. Zhu, *Appl. Phys. Lett.*, 74 (1999) 20

[6] P. P. Mardilovich, A. N. Govyadinov, N. I. Mukhurov, A. M. Rzhevskii and R. Paterson, *J. Mem. Science*, 98 (1995) 131-142

[7] J. H. Yuan, F. Y. He, D. C. Sun and X. H. Xia, *Chem. Mater.*, 16 (2004) 1841-1844

[8] I. Horcas, R. Fernández, J. M. Gómez, J. Colchero, J. Gómez-Herrero and A. M. Baro *Rev. Sci. Instrum.* 78, 013705 (2007)

[9] L. F. Marsal, L. Vojkuvka, J. Ferré-Borrull, T. Trifonov, and J. Pallarès phys. stat. sol. (c) 4, No. 6, 1918– 1922 (2007)

Fabrication and characterization of a porous silicon microcavity and study of the humidity influence

E. Xifré-Pérez, L.F. Marsal, J. Ferré -Borrull, and J. Pallarès

Departament d'Enginyeria Electrònica, Elèctrica i Automàtica, Universitat Rovira i Virgili, Avda. Països Catalans, 26, 43007 Tarragona.

Abstract

A porous silicon microcavity has been designed and fabricated. Its reflectivity spectrum is characterized by a transmission peak centered at λ=3 μm in between two spectral regions with high reflectivity values. The reflectivity spectrum of the microcavity has been simulated using the transfer matrix method, which results in good agreement with the measured one. The reflectivity spectrum of the microcavity has been also analyzed under different humidity conditions. We demonstrate that the transmission peak shifts to higher wavelengths and that the reflectivity decreases when the humidity increases. The reflectivity spectrum of the microcavity is recovered when the humidity returns to the initial laboratory conditions.

1. Introduction

Porous silicon is a dielectric material obtained by HF electrochemical etching of silicon. The refractive index of the porous silicon layers depends on the current density applied during the etching and its thickness depends on the time for which the current is applied. This material has excellent mechanical and thermal properties and is compatible with silicon-based microelectronics technology.

There are many different applications for porous silicon multilayers, such as waveguides [1], rugate filters [2] and omnidirectional mirrors [3]. Some of the most widely studied are the applications of microcavities, that have been used as light emitting devices [4], hydrocarbon sensors [5] or biosensors [6].

In this paper, we design and fabricate a microcavity structure with a transmission peak centered at approximately λ=3 μm. Its reflectivity spectrum is measured and analyzed and compared with the simulated reflectivity spectrum obtained during the design process. Finally, the influence of different humidity levels on the reflectivity spectrum of the microcavity is studied in order to determine its suitability for humidity sensors. Optical measurements may be more robust for some applications but only a few authors proposed the analysis of the optical properties of porous silicon microcavities for the detection of humidity changes [7].

2. Fabrication and characterization

The porous silicon microcavity was fabricated by the electrochemical etching of p^+-type silicon wafers with a resistivity of 0.01Ωcm in an ethanoic HF electrolyte with concentration of 15.4% (volumetric ratio). The SEM image of the fabricated microcavity can be observed in Fig. 1. It consists of a spacer layer inserted in between two symmetric Distributed Bragg Reflectors (DBR) with three periods. Each period consists of two layers with different refractive indices (n_1, n_2) and thicknesses (d_1, d_2).

The current densities used were J_1 = 100 mA/cm^2 and J_2 = 20 mA/cm^2 for the DBR and J_S = 70 mA/cm^2

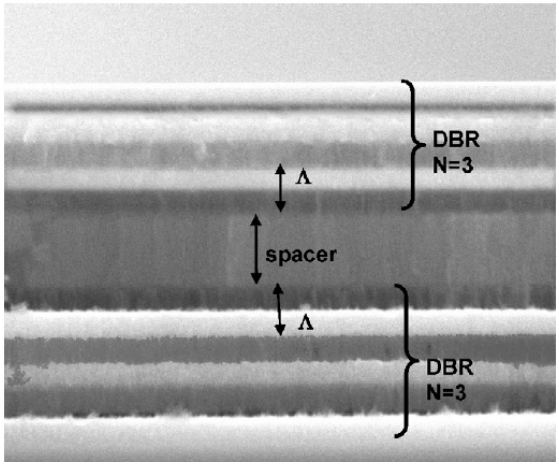

Fig. 1. SEM image of the fabricated porous silicon microcavity. The spacer layer is located in between two DBR. Each DBR is formed by the periodic repetition (N=3) of two layers with low refractive index (gray layer) and high refractive index (light gray layer).

for the spacer layer. They were applied during 10 s for J_1, 20 s for J_2 and 30 s for J_S, respectively, which lead to estimated layer thicknesses of d_1=0.55 μm, d_2=0.41 μm and d_S=1.50 μm.

The reflectivity spectrum of the microcavity was measured for incidence angle 20º using a FTIR spectrometer Bruker Vertex 70 (Fig. 2). The spectrum is characterized by a reflectivity resonance at 2.97 μm in between two high reflectivity bands. This measured spectrum has been compared with the one obtained with the simulation programs based on the transfer matrix method [8]. For the simulation, the refractive index was calculated for each current density using the method explained in [9], being the calculated refractive indices n_1=1.22, n_2=1.82 and n_S=1.30 for the studied wavelength range. The thicknesses used for the simulation were the ones estimated from the etching time. Fig. 2 also shows the simulated reflectivity spectrum assuming an incidence angle of 20º. We can observe that there is a good agreement between the simulated and the measured reflectivity spectra.

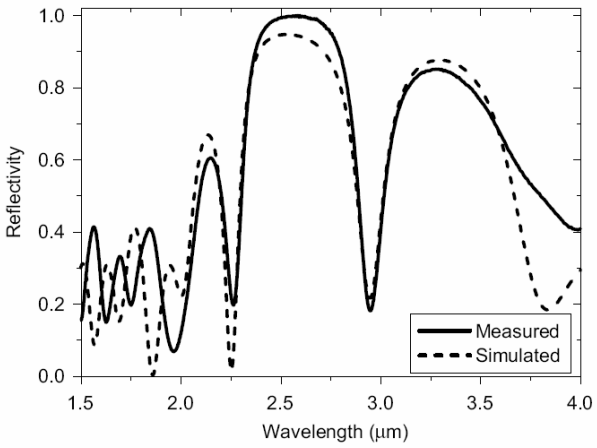

Fig. 2. Measured (solid line) and simulated (dashed line) reflectivity spectrum of the fabricated microcavity for incidence angle 20º.

3. Influence of the relative humidity on the reflectivity spectrum

We have measured the reflectivity spectrum of the fabricated microcavity under different humidity levels (Fig. 3). In this figure we can observe that the changes in the spectrum are small, in good agreement with other results presented in the literature [7]. The inset in Fig. 3 shows the zoom of the transmission peak and the fitting using a Gaussian function. We can observe that when humidity increases, the transmission peak shifts to higher wavelengths. The reflectivity of the peak also decreases.

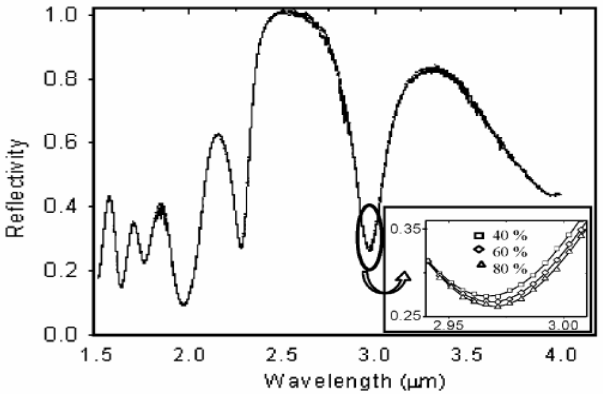

Fig. 3. Measured reflectivity spectrum for humidity levels of 40%, 50%, 60%, 70% and 80%. Inset: Zoom of the measured (symbol) reflectivity spectrum of the microcavity centered at the reflectivity resonance for humidity levels of 40%, 60% and 80%. The solid lines are the fitted values using a Gaussian function.

7. Conclusions

A porous silicon microcavity has been fabricated, characterized and simulated. The FTIR reflectivity spectrum of this device depends on the humidity level of the ambient medium. The reflectivity resonance shifts to higher wavelengths and the reflectivity decreases when the humidity increases.

Acknowledgements

This work was supported by the Spanish Commission of Science and Technology (CICYT) under Grant number TEC2006-06531. J. Ferré acknowledges the Ramon y Cajal fellowship from the Spanish Ministerio de Ciencia y Tecnología.

References

[1] A.M. Rossi, G. Amato, V. Camarchia, L. Boarino, S. Borini, "High-quality porous-silicon buried waveguides" Appl. Phys. Lett. **78**, 3003 (2001).

[2] E. Lorenzo, C.J. Oton, N.E. Capuj, M. Ghulinyan, D. Navarro-Urrios, Z. Gaburro, and L. Pavesi, "Fabrication and optimization of rugate filters based on porous silicon", phys. stat. sol. (c), **2**, 3227 (2005).

[3] E. Xifré-Pérez, L.F. Marsal, J. Pallarès, J. Ferré -Borrull, "Porous silicon mirrors with enlarged omnidirectional band gap", Appl. Phys. Lett. **97**, 064503 (2005).

[4] S. Chan, and P.M. Fauchet, "Tunable, narrow, and directional luminescence from porous silicon light emitting devices". Appl. Phys. Lett., **75**, 274 (1999).

[5] J. Dorvee, M.J. Sailor, "A low-power sensor for volatile organic compounds based on porous silicon photonic crystals", phys. stat. sol. (a) **202**, 1619 (2005).

[6] C. Pacholski, M. Sartor, M.J. Sailor, F. Cunin, G.M. Miskelly, "Biosensing using porous silicon double-layer interferometers: Reflective interferometric Fourier transform spectroscopy", J. Am. Chem. Soc. **127**, 11636 (2005).

[7] C.J. Oton, L. Pancheri, Z. Gaburro, L. Pavesi, C. Baratto, G. Faglia, G. Sberveglieri, phys. stat. sol. (a), **197**, 523 (2003).

[8] P. Yeh, "Optical Waves in Layered Media", Wiley, New York, 1988.

[9] E. Xifré-Pérez, J. Pallarès, J. Ferré-Borrull, T. Trifonov, L.F. Marsal, "Low refractive index porous silicon multilayer with a high reflection band", phys. stat. sol. (c),**4**, 2034 (2007).

Thin film porous alumina for sensor applications

R. Hrdy[1], J. Hubalek[1], X. Vilanova[2], L. F. Marsal[2] K. Klosova[1]

[1]Brno University of Technology, Department of Microelectronic, Údolní 53, 602 00 Brno, Czech Republic,
[2]Rovira i Virgili University, Electronic Department, Paisos Catalans 26, 43007 Tarragona, Spain
hrdyr@email.cz

Abstract

Various forms of anodized alumina (AA) has been studied for different application. [1,2] AA, which is fabricated from aluminum foils with thickness 250 μm, is one of them. The disadvantage of this template lies on its difficulty manipulation. Better way is to deposit aluminum thin film directly on the substrate and after that to anodize porous alumina. [3]. However, it requires deposition equipment and clean rooms. This technique has made possible fabrication of AA and subsequently nanowires on various metallic layers without necessity to solve problems allied to manipulation and dissolving of remainder aluminum. Therefore, this technique is more suitable for microsensors industry. The aim of present work is to create a new high sensitive electrochemical sensor using AA template which is created from aluminum thin film.

1. Introduction

The most interesting sphere is the applications of anodized alumina (AA) with various materials in sensors technology. Especially, the AA is used for increase areas of sensors active layers. The AA has been applied as template for deposition nanowires or nanotubes on substrate or as mask for etching tiny ordered motives. [4]

Nowadays we can see a tendency to fabricate still smaller sensors elements but it is required the same or higher sensitivity.[2,5] One of many solutions could be enlargement of detection area by force of nanopillars or nanotubes deposited on surface. The utilization of different AA templates makes possible to produce nanoparticles with various sizes. Unfortunately, there are still many outstanding challenges in production multi metallic systems with perfectly ordered nanoparticles surface.

2. Experiments

N-type of silicon substrate is used for deposition of thin sputtered aluminum film. The thickness of film was 2 μm and the purity 99,999%. The film was not homogenous and it was moulded by crystals bigger than 100 nm. Crystal's boundaries were very apparent and deep, Fig.1. They avoided the creation of ordered structure. [5]

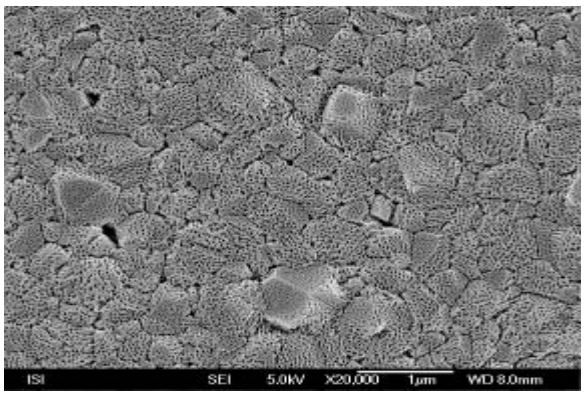

Fig.1 SEM image of the sputered porous alumina surface anodized in sulfuric acid at 25V at 10°C. Anodization time was 13 minutes.

In the second experiment, the alumina film was deposited by vapour deposition (VD) method. The surface was glossier than sputtered film. On the other hand, the problem with adhesion was appeared. The evaporated aluminum films were cracked or involved by anodization in many cases.

In both experiments, samples with alumina film were cleaned and degreased in acetone at first. After that, they were put on a cell, where the sample was the anode and a stainless steel was the cathode. Sulfuric acid at 10% was used as electrolyte. The temperature of electrolyte was ranging from 0°C to 24°C. The voltage was 25 V. The electrolyte was rigorously stirred. [2,3] Samples were anodized between 13 minutes and 15 minutes. During this time, current value decreased to value of 100 μA. After that, samples were etched in 5% phosphoric acid at 39°C in ordered to open the pores and dissolve the porous barriers. The etching time was between 2 and 3 minutes. After 3 minute of etching, the ceramic structure started breaking down. The pore diameter and inter-pore distance varied in a range of 15 – 30 nm and 20 – 50 nm respectively, see Fig. 2.

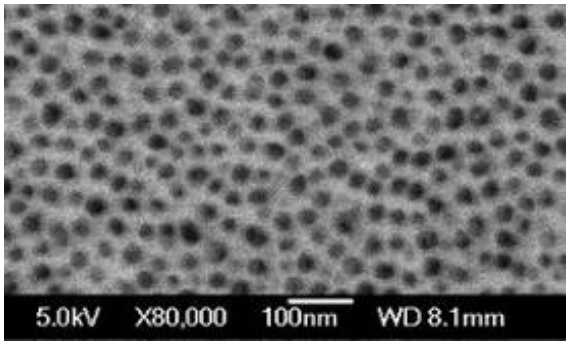

Fig.2 SEM image of the evaporated surface of the porous alumina anodized in sulfuric acid at 25V at 0°C. The sample was etched in 5% phosphoric acid. Anodization time was 15 minutes and etching time was 2 minutes.

Next step was preparation of AA on inter metallic layer. At first, 250 nm of nitride was fabricated on silicon wafer as non-conducting layer. On that, a photo-sensitive template was obtained with using a lithographic technique. The structure of designed template is shown in Fig. 3. The Lift-Off technique was used in order to create thin gold film with comb-like structure. The thickness of the gold layer was 300 nm. The template was dissolved in xylene ultrasonic bath. After that, the aluminum thin film was evaporated on the structure and the same conditions of anodization described above were applied.

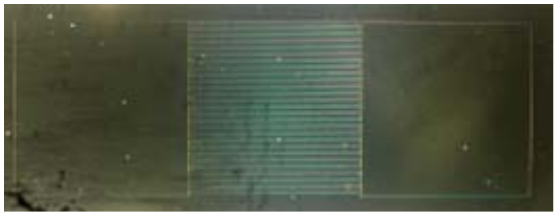

Fig.3. New type of micro sensor It has length 9 mm.

3. Result and discussion

Fig. 1 and 2 show that the alumina structures are not enough self-organized. The pores have been created ramdomly and they have different sizes. Nanocrystals of aluminum are the main cause of this issue. The size of nanocrystals grows is time dependent. Nanocrystals of aluminum are evident in Fig. 1, where many defects can be found between nanocrystals. Using VD technique this problem was solved, see Fig. 2. The aluminum layer, which was deposited by sputtering, was turbid. On the other hand the layer, deposited by VD, had brilliant polished surface. Because the VD run in many steps and the alumina film has a thickness of 200 nm, nanocrystals do not grow up as much as nanocrystals in sputtered film. Therefore the alumina thin film deposited by VD has more quality.

Another task is finding conditions for creating ordered porous structure. In comparison, it is much difficult to apply anodization by Two-step method because it often terminates in dissolving or breaking up the aluminum films by anodization at second step. This problem is much dependent on adhesion of alumina layer. Anodization in one step was success managed and conditions were determined but then an initiation of second step is done, it is necessary to dissolve the first anodized layer of AA. This part of fabrications is in progress at higher temperature in a range of 40°C to 60°C and the anodization is done at the same temperature or lower than room temperature. This thermal difference causes very high mechanical stress between AA and bottom layer. The problem could be solve with a slow increasing/decreasing of the temperature.

4. Conclusions

The new technique for fabrication of nanoporous alumina on gold comb like electrod was found. This porous structure is suitable for deposition of metal nanoparticles. The self-organized process of porous alumina is dependent on high purity, homogeneity of aluminum film and adhesion between aluminum and gold intermetalic layers. The conditions of the anodization process using aluminum thin films deposited by evaporation and sputtering were found. The optimal parameters for anodization processes have been determined for the first step of anodization process.

5. Acknowledgment

This research has been supported by Grant Agency of the Academy of Sciencies of the Czech Republic under the contract GAAV 1QS201710508 Impedimetric chemical microsensors with nanostructured electrode surface, by the Czech Ministry of Education within the framework of Research Plan MSM 0021630503 MIKROSYN New Trends in Microelectronic Systems and Nanotechnologies and like a collaboration under the contract GD102/03/H105 Modern Method of Analysis, Design and Application of Electronically Circuit.

References

[1] N.M. Yakovleva, A.N. Yakovlev, and E.A. Chupakhina, Structure of Al_2O_3 Films Prepared by Two-Step Anodization. Inorganic Materials, Vol. 34, No. 7, 1998, pp. 711-713.

[2] H.Madsuda, K. Yada, A Osaka, Selforderes of Cell cnofiguration of Anodic Porous Alumina with Large-Size Pores on Phosphoric Acid Solution, J.Apply.Phys,Vol 37,No11A,,1998,pp L1340

[3] O. Jessensky, F. Müller, and U. Gösele, Self-organized Formation of Hexagonal Pore Structure in Anodic Alumina. J. Electrochem. Soc. Vol. 145, No.11 (1998) 3735-3740.

[4] H.Madsuda, K.Fukuda, Ordered Metal Nanohole Arrays made by a two step replication of honey comb structures of anodic alumina. Science Vol.268,1995,pp,1566 8

[5] R. Hrdý, J. Hubálek, Selfordered pore structure of anodized alumina thin film on Si substrate, Technical digest of EDS 05, Brno, Czech Rep. 2005 ISBN 80-214-2990-9

Hard Anodization vs. Standard Two Step Anodization: Morphology Comparison

L. Vojkuvka*, A. Santos, J. Ferré-Borrull, J. Pallarés and L. F. Marsal

NePhoS (Nano-electronic and Photonic Systems), Departament d'Enginyeria Electrònica, Elèctrica i Automàtica, University Rovira i Virgili, Av. Països Catalans 26, 43007 Tarragona, Spain
**E-mail: lukas.vojkuvka@urv.cat*

Abstract

We report on the fabrication of self-ordered porous alumina with long interpore distance. The samples were prepared in an oxalic acid solution using a novel hard anodization process. In contrast to the common two step anodization process, this technique only consists of a single step, where a specific voltage profile is applied. The as-produced samples were examined and analyzed in detail by scanning electron microscopy. The results show that the porous structure produced by hard anodization have larger interpore distance of 310 nm as compared with the conventional two step anodization, where this distance can vary between 90 nm and 120 nm. Moreover, the porous layer growth rate is about 10 times faster.

1. Introduction

In the last decades the scientists have been focused on nanostructured porous materials because of their unique geometrical properties. Such nanoporous materials are very suitable as a template for synthesis of functional nanostructures [1, 2] or they can be also used for fabrication of various nanodevices, e.g. solar cells [3] or photonic crystals [4]. Among others, the ordered porous alumina (OPA) plays an important role in nanotechnology because of its easily tuneable morphological properties, relatively low-cost production and wide range of applications.

The porous alumina has been investigated over the last 50 years, but the breakthrough became in 1995, when Masuda and Fukuda have produced for the first time the self-ordered porous alumina membrane using the so-called two step anodization process [5]. Thereafter, the scientific interest in the OPA has significantly increased. In summary, the OPA nanostructures with nanopores hexagonally arranged into close-packed domains must be fabricated under specific conditions known as ¨self-ordering regimes¨ [5]. This means that the OPA morphology such as the pore diameter and the interpore distance strongly depend on the anodizing parameters and especially on the acid solution and anodizing voltage [6]. If the anodizing parameters are set outside of the optimum range, it leads to the extreme decrease of the ordering degree for the resultant structure. Recently, Lee et al. have discovered a novel approach to fabricate OPA with large interpore distance between 220 – 300 nm [7]. In principle, this fabrication process combines the so-called hard anodization (that was widely used in industry since 1960s) and the specific conditions from standard two step anodization. This important finding has significantly contributed to the expansion of applications based on the ordered porous alumina.

From the application viewpoint it is necessary to determine the quantitative and qualitative properties of ordered porous alumina with large lattice constant produced by the hard anodization technique. Therefore, this paper is focused on the study of ordering degree and pore uniformity of OPA structures using high-resolution images from scanning electron microscopy (SEM).

2. Experimental

The samples were prepared from high purity (99.999%) aluminium (Al) foils (Godfellow Cambridge Ltd.) with 0.25 mm thickness. The preliminary aluminium treatments were firstly annealing in an inert ambient at 400 ºC for 2 hours and then the foils were electropolished in ethanol and perchloric acid solution (4:1) to obtain smooth-surfaced samples for anodizing. The standard two step anodization procedure was described in detail elsewhere [8]. The hard anodization was performed in 0.3 M oxalic acid solution cooled to 1 ºC. The system was connected to a potenciostatic control that has the following profile: first, the standard anodization (SA) is set to 40 V for 5 min. (Fig. 1, region 1), then the voltage increases quickly from 40 V to 140 V at a rate of 0.8 V/s (Fig. 1, region 2), and finally the high voltage is maintained constant at 140 V for 1 hour to perform the so-called hard anodization (Fig. 1, region 3). The remaining aluminium substrate was immersed in mixture of 0.1 M copper dichloride and 20%wt. hydrochloric acid ($CuCl_2$ + HCl) until the freestanding OPA membrane was achieved. In order to open the pore bottoms, the OPA membrane was etched in 5% wt. phosphoric acid for 20 minutes.

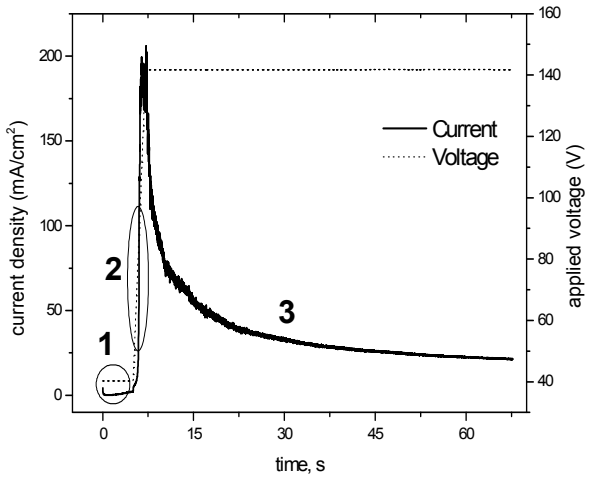

Fig.1. The current density vs. time dependence (solid line) under specific voltage control (dashed line)

3. Results

The as-produced OPA membranes were examined by scanning electron microscopy (SEM – FEI Quanta 600). The SEM images of different OPA membranes are compared in Fig. 2: a) the bottom surface of a sample produced in 0.3 M oxalic acid and 140V, where the inset shows the part covered by a barrier oxide layer before pore openning, and b) the top surface image of OPA anodized in standard two step process using 0.3 M oxalic acid and 40V. In comparison, the porous structure from HA (Fig. 2a) has the larger distance between pores around 300 nm and also a bigger domain size between 2 - 3 μm compared to SA samples (Fig. 2b). Similarly as in the SA samples, we can observe that each pore is hexagonally enclosed by six neighboring pores. This confirms very high ordering degree of HA porous structure. According to cross-section SEM analysis, the thickness of 88 μm was measured after one hour of hard anodizing process and the pore growth rate is 10 times faster than in the case of standard anodizing.

4. Conclusions

Ordered porous alumina membranes were successfully produced using a novel fabrication process called hard anodization. This process has several advantages compared with the conventional two step anodization: i) the self-ordered porous alumina produced in hard anodization is feasible only in a single fabrication step, ii) the HA process is more effective because the oxide growth rate is almost 10 times higher (80 μm/h) than in the case of standard anodization and iii) we can achieve a newly discovered large lattice constant of 300 nm for the resultant porous alumina structure. The interpore distance, the high pore ordering and the particular optical properties of such porous alumina, make these structures a very promising candidates for realising photonic bandgap materials for visible wavelength.

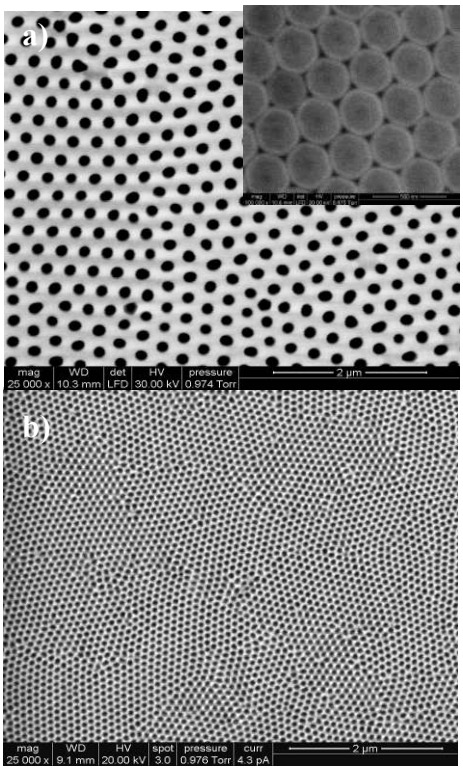

Fig.2. The surface images of porous alumina produced in: a) hard anodization at 140 V for 1 hour (inset shows the bottom part before pore opening) and b) standard two step anodization at 40V.

Acknowledgement

This work was supported by the Spanish Ministry of Education and Science (MEC) under grant number TEC2006-06531. J. Ferré acknowledges the Ramon y Cajal fellowship from the Spanish Ministerio de Ciencia y Tecnología.

References

[1] W. Lee, R. Scholz, K. Nielsch and U. Gösele, Angew. Chem. Int. Edn, 44 (2005) 6050–6054.
[2] G. Che, B. B. Lakshmi, E. R. Fisher and C. R. Martin, Nature, 393 (1998) 346.
[3] R. Karmhag, T. Tesfamichael, E. Wackelgard, G. A. Niklasson and M. Nygren, SolarEnergy, 68 (2000) 329.
[4] H. Masuda, M. Ohya, H. Asoh, M. Nakao, M. Nohtomi, T. Tamamura, Jpn. J. Appl. Phys., 38 (1999) L1403.
[5] H. Masuda and K. Fukuda, Science, 268 (1995) 1466.
[6] A. P. Li, F. Muller, A. Birner, K. Nielsch and U. Gösele, J. Appl. Phys., 84 (1998) 6023–6026.
[7] W. Lee, R. Ji, U. Gösele and K. Nielsch, Nature Materials, 5 (2006) 741-746.
[8] L. F. Marsal, L. Vojkuvka, J. Ferre-Borrull, T. Trifonov and J. Pallares, Phys. Stat. Sol. (c), 4 (2007) 1918 – 1922.

Autonomous Current-Programmed One-Cycle Controller with Feedforward Applications

Guillermo Ruiz Magaz

email:guillermo.ruiz@urv.net. Dept. Electronic, Electric and Automatical Engineering

Universitat Rovira i Virgili, Av. Dels Països Catalans,26 Campus de Sescelades, 43007 Tarragona, Spain,

Abstract

An introduction to the dynamic of the converter Boost, which is going to serve us of departure for our future study. Thus same the suggestion to continue this work with the implementation to level of simulation and assembly for converters Boost that work in "interleaving". Also the different software of simulation with the one is presented that normally is used to working itself. Autonomous current programmed one-cycle controller with feed-forward (ACPOCCF) for the elementary dc-dc converters is proposed[1]. With this method the current perturbations are rejected in one cycle at variable switching frequency.

1. Introduction

The boost converter see figure 1, is a topology very utilized in applications in which we should obtain a high voltage since a source of low voltage, as is the case of solar boards.

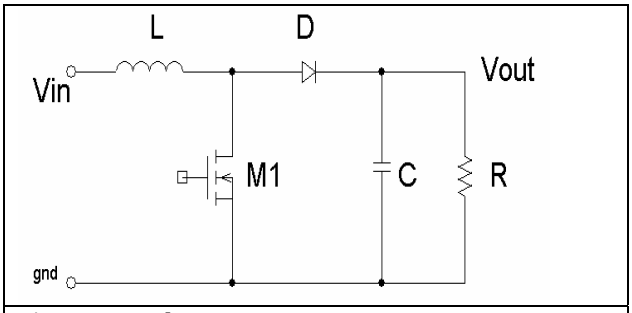

Fig. 1 Boost schema

These two faces are the change of topology according to the state on or off just as can be seen in the figure 2 [2].

One of the problems that has this boost topology, is its instability, owed this that is a system of second order and disruptions in the entrance or the exit can cause oscillations done not desire that carry the converter boost to the instability. At the same time the converter boost, presents two faces at the moment of to be produced the commutation. These two faces are the change of topology according to the state on or off just as can be seen in the figure 2.

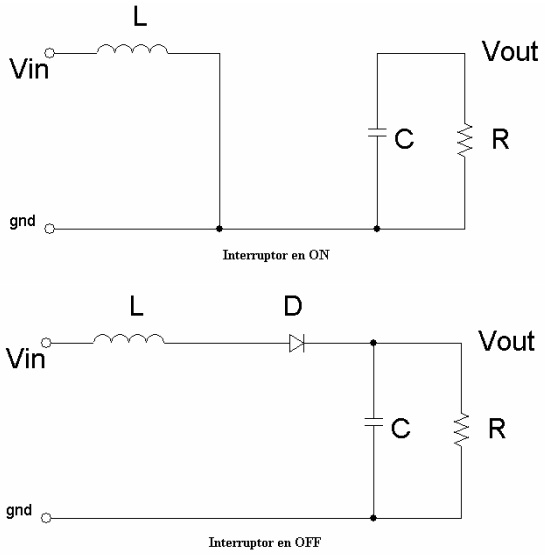

Fig. 2 Two Boost states due to switch position

2. Simulation Tools

We can introduce the electronic design of the so much circuit of the control as of the plant and to do simulations to see the forms of wave sign in concrete. The accuracy that this type of simulators gives us is going to be very close to the real , while the model that find chosen of the components they approach it but possible to the real. With this type of software we can do studies AC, DC, parametric, Monte Carlo. And with it to tune up our control in the figure 3 we can see the answer of the V1 in an oscillator of square wave in two simulators, Orcad-Pspice and Psim . We see that the Psim is not capable of simulating correctly the circuit, on the other hand the Orcad-Psim is correct

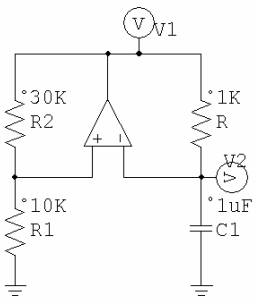

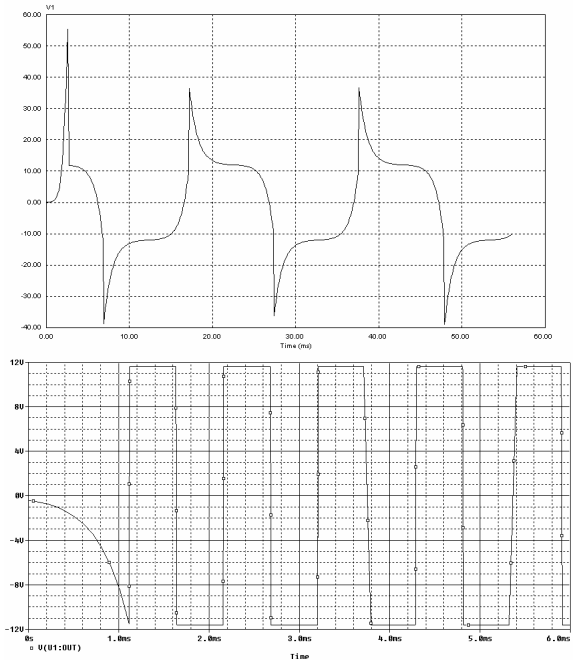

Fig. 3 Ocillator schema, Psim and Orcad-Pspice simulations

3. Controller Description

The controller [3] consists of a level-activated S–R flip-flop, a resetable integrator, a couple of comparators and some logic gates to ensure a reset-priority activation of the flip-flop, whose Q output activates the driver of the converter's switch. In the case of PCC (Fig.4), the reset of the flip-flop takes place when the inductor current (i_L) reaches a maximum level (I_{REF}) which can be constant or given by an outer compensating loop (i.e., a voltage PI network) [4]. Simultaneously, the converter's switch is turned off and the integrator is also reset starting to integrate the controller's input A from zero initial condition. Similarly, the turn-on of the switch occurs when the integrator's output equals the B input of the controller

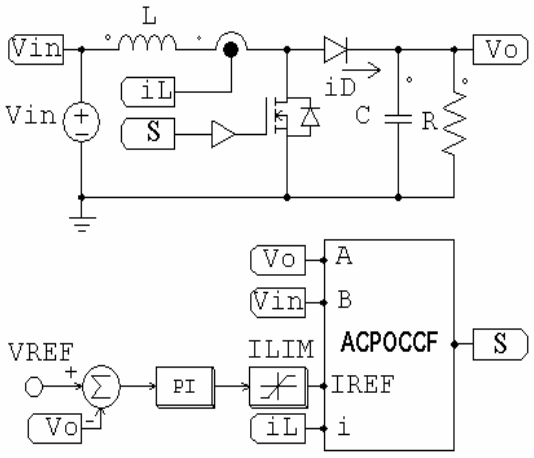

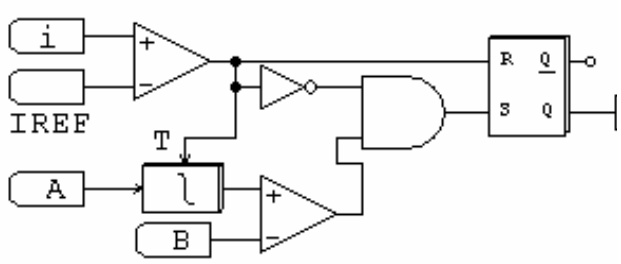

Fig. 4 ACPOCCF Strategy controller

4. Comparison PWM vs. ACPOCCF

To verify the performances of the regulator depicted in Fig.5 several PSIM simulations have been carried out. The results of the simulations are compared with those obtained from an equivalent PWM current-mode controlled boost converter operating at the same nominal switching frequency (50 kHz).

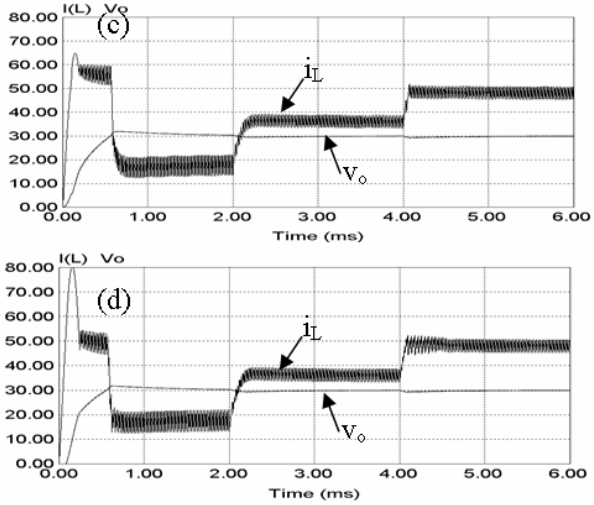

Fig 5 System response to different steps (input voltage and load applied at different instants: (c) ACPOCCF, (d) Equivalent PWM controlled system.

5. Conclusions

In this paper, a new current mode control one cycle control method is described

Simulation results show that the method has some advantages over the traditional PWM control with compensating ramp. Experimental results are in progress and they will be published in a further study

REFERENCES

[1] C. C. Fang, "Sampled Data Modeling and Analysis of One Cycle Control and Charge Control" IEEE: 1964, pp. III-9,12.

[2] R.W. Erickson, "Fundamentals of power electronics", Chapman and hall, New York, 1997 pp. 45-70

[3] R. Giral et al.. Autonomous Current-Programmed One-Cycle Controller. Saaaei: 2004.

[4] R. Sheehan, A New Way to Model Current-Mode Control, Power Electronics Technology, May 2007, pp.14-20.